

Millimetre-Wave Antennas and Systems for the Future 5G

Guest Editors: Masood Ur-Rehman, Qammer H. Abbasi, Atiqur Rahman, Imdad Khan, Hassan T. Chattha, and Mohammad Abdul Matin





Millimetre-Wave Antennas and Systems for the Future 5G

**Millimetre-Wave Antennas and Systems
for the Future 5G**

Guest Editors: Masood Ur-Rehman, Qammer H. Abbasi,
Atiqur Rahman, Imdad Khan, Hassan T. Chattha,
and Mohammad Abdul Matin



Copyright © 2017 Hindawi Publishing Corporation. All rights reserved.

This is a special issue published in "International Journal of Antennas and Propagation." All articles are open access articles distributed under the Creative Commons Attribution License, which permits unrestricted use, distribution, and reproduction in any medium, provided the original work is properly cited.

Editorial Board

Ana Alejos, Spain
Mohammad Ali, USA
Jaume Anguera, Spain
Rodolfo Araneo, Italy
Alexei Ashikhmin, USA
Herve Aubert, France
Paolo Baccarelli, Italy
Xiulong Bao, Ireland
Toni Björninen, Finland
Stefania Bonafoni, Italy
Djuradj S. Budimir, UK
Paolo Burghignoli, Italy
Shah Nawaz Burokur, France
Giuseppe Castaldi, Italy
Luca Catarinucci, Italy
Felipe Catedra, Spain
Marta Cavagnaro, Italy
Deb Chatterjee, USA
Shih Yuan Chen, Taiwan
Yu Jian Cheng, China
Renato Cicchetti, Italy
Riccardo Colella, Italy
Lorenzo Crocco, Italy
Claudio Curcio, Italy
Francesco D'Agostino, Italy
M. Elena de Cos Gómez, Spain
Tayeb A. Denidni, Canada
Giuseppe Di Massa, Italy
Michele D'Urso, Italy
Hala A. Elsadek, Egypt

Francisco Falcone, Spain
Miguel Ferrando Bataller, Spain
Flaminio Ferrara, Italy
Vincenzo Galdi, Italy
Claudio Gennarelli, Italy
Farid Ghanem, Algeria
Sotirios K. Goudos, Greece
Rocco Guerriero, Italy
Kerim Guney, Turkey
Song Guo, Japan
Mohamed Himdi, France
Tamer S. Ibrahim, USA
Mohammad T. Islam, Malaysia
M. Ramlee Kamarudin, Malaysia
Slawomir Koziel, Iceland
Luis Landesa, Spain
Ding-Bing Lin, Taiwan
Angelo Liseno, Italy
Pierfrancesco Lombardo, Italy
Giampiero Lovat, Italy
Lorenzo Luini, Italy
Atsushi Mase, Japan
Diego Masotti, Italy
C. F. Mecklenbräuker, Austria
Massimo Migliozi, Italy
A. Toaha Mobashsher, Australia
Ananda S. Mohan, Australia
J.-M. Molina-Garcia-Pardo, Spain
Giorgio Montisci, Italy
Marco Mussetta, Italy

N. Nasimuddin, Singapore
Miguel Navarro-Cia, UK
Mourad Nedil, Canada
Symeon Nikolaou, Cyprus
Giacomo Oliveri, Italy
Pablo Otero, Spain
A. D. Panagopoulos, Greece
Ikmo Park, Republic of Korea
Josep Parrón, Spain
Matteo Pastorino, Italy
M. Pieraccini, Italy
Xianming Qing, Singapore
Ahmad Safaai-Jazi, USA
S. Safavi-Naeini, Canada
M. Salazar-Palma, Spain
Stefano Selleri, Italy
Prabhakar Singh, India
Raffaele Solimene, Italy
Gino Sorbello, Italy
Seong-Youp Suh, USA
Sheng Sun, Hong Kong
Larbi Talbi, Canada
Luciano Tarricone, Italy
Parveen Wahid, USA
Wen-Qin Wang, China
Shiwen Yang, China
Yuan Yao, China
Jingjing Zhang, Denmark

Contents

Millimetre-Wave Antennas and Systems for the Future 5G

Masood Ur-Rehman, Qammer Hussain Abbasi, Atiqur Rahman, Imdad Khan, Hassan Tariq Chattha, and Mohammad Abdul Matin

Volume 2017, Article ID 6135601, 2 pages

Multiband Split-Ring Resonator Based Planar Inverted-F Antenna for 5G Applications

Muhammad Kamran Ishfaq, Tharek Abd Rahman, Hassan Tariq Chattha, and Masood Ur Rehman

Volume 2017, Article ID 5148083, 7 pages

Millimeter-Wave Microstrip Antenna Array Design and an Adaptive Algorithm for Future 5G Wireless Communication Systems

Cheng-Nan Hu, Dau-Chyrh Chang, Chung-Hang Yu, Tsai-Wen Hsaio, and Der-Phone Lin

Volume 2016, Article ID 7202143, 10 pages

Enhanced Next Generation Millimeter-Wave Multicarrier System with Generalized Frequency Division Multiplexing

Hidekazu Shimodaira, Joongheon Kim, and Ali S. Sadri

Volume 2016, Article ID 9269567, 11 pages

Pilot Contamination Mitigation via a Novel Time-Shift Pilot Scheme in Large-Scale Multicell Multiuser MIMO Systems

Zhangkai Luo, Huali Wang, and Wanghan Lv

Volume 2016, Article ID 7628692, 9 pages

Connectivity Analysis of Millimeter-Wave Device-to-Device Networks with Blockage

Haejoon Jung and In-Ho Lee

Volume 2016, Article ID 7939671, 9 pages

Joint User Scheduling and MU-MIMO Hybrid Beamforming Algorithm for mmWave FDMA Massive MIMO System

Jing Jiang and Deting Kong

Volume 2016, Article ID 4341068, 10 pages

A Novel Simulator of Nonstationary Random MIMO Channels in Rayleigh Fading Scenarios

Qiuming Zhu, Xinglin Liu, Xuefeng Yin, Xiaomin Chen, and Cuiwei Xue

Volume 2016, Article ID 3492591, 9 pages

Editorial

Millimetre-Wave Antennas and Systems for the Future 5G

**Masood Ur-Rehman,¹ Qammer Hussain Abbasi,² Atiqur Rahman,³
Imdad Khan,⁴ Hassan Tariq Chattha,⁴ and Mohammad Abdul Matin⁵**

¹Centre for Wireless Research, University of Bedfordshire, Luton LU1 3JU, UK

²Texas A & M University at Qatar, Doha, Qatar

³Department of Electrical & Computer Engineering, North South University, Dhaka, Bangladesh

⁴Department of Electrical Engineering, Faculty of Engineering, Islamic University in Madinah, Al-Madinah, Saudi Arabia

⁵Department of Electrical and Electronic Engineering, Institute Teknologi Brunei, Gadong, Brunei Darussalam

Correspondence should be addressed to Masood Ur-Rehman; masood.urrehman@beds.ac.uk

Received 4 April 2017; Accepted 5 April 2017; Published 10 April 2017

Copyright © 2017 Masood Ur-Rehman et al. This is an open access article distributed under the Creative Commons Attribution License, which permits unrestricted use, distribution, and reproduction in any medium, provided the original work is properly cited.

1. Introduction

5G is the next technological marvel enabling ubiquitous portable systems for the realization of Internet of Things (IoT). Millimeter-wave frequency range is a prestandardization favorite for the portable 5G applications. High performing millimeter-wave devices require efficient low-profile antennas to ensure reliable and interference-free communications. Requirements for increased power, larger bandwidth, higher gain, and insensitivity to the human user presence further complicate the antenna and propagation aspects. Enhanced techniques for multiplexing, interference mitigation, scheduling, and radio resource allocation work alongside the antenna design to realize efficient millimeter-wave systems delivering seamless and optimal performance. Being a newly developed area, simulation techniques also need to be revisited to ensure high level of accuracy of millimeter-wave antennas and systems. It solicits novel ideas and innovative solutions for the antenna design and system development.

This special issue is intended to reflect current research trends and novel approaches to address the issues of antenna design and propagation for 5G enabled millimeter-wave applications. Particular emphasis has been put in the antenna design and measurement methods, MIMO antenna systems, and beamforming techniques; solutions for advanced millimeter-wave operational scenarios including device-to-device communications, multiplexing, spectrum cognition,

and interference mitigation have also received particular emphasis.

2. Contributions

The special issue consists of 7 contributions covering a variety of antenna design and MIMO techniques.

In “Multiband Split-Ring Resonator Based Planar Inverted-F Antenna for 5G Applications” by M. K. Ishfaq et al., the authors present design and realization of a novel multiband antenna for 5G applications. The antenna is composed of a PIFA, an inverted-L parasitic element, a rectangular shaped parasitic element, and a split-ring resonator etched on the top plate of the PIFA. The antenna covers three frequency bands at 6 GHz (5–7 GHz), 10 GHz (9–10.8 GHz), and 15 GHz (14–15 GHz), each with more than 1 GHz impedance bandwidth. It exhibits peak gains of 3.4 dBi, 4.9 dBi, and 5.85 dBi, respectively, at the three bands.

In “Millimeter-Wave Microstrip Antenna Array Design and an Adaptive Algorithm for Future 5G Wireless Communication Systems” by C.-N. Hu et al., the authors present a high gain millimeter-wave Low-Temperature Cofired Ceramic microstrip antenna array having a compact, simple, and low-profile structure. Significant level of interference mitigation is achieved by incorporating minimum mean square error adaptive algorithm with the proposed antenna. The simulated antenna performance is validated through

measurements and demonstrates a return loss of ≥ 15 and a peak gain of ≥ 6.5 dBi at 37.5–39 GHz frequency band.

In “Enhanced Next Generation Millimeter-Wave Multi-carrier System with Generalized Frequency Division Multiplexing” by H. Shimodaira et al., the authors discuss a new Generalized Frequency Division Multiplexing frame to comply it with IEEE 802.11ad standard and extend the intercarrier interference reduction technique to be used for the wireless systems using this standard. The proposed method exhibits good Peak-to-Average Power Ratio and throughput performance simultaneously while reducing the computational costs by 83%. This method is applicable to other mmWave standards in IEEE 802.11ay and 5G mmWave cellular networks as well.

In “Pilot Contamination Mitigation via a Novel Time-Shift Pilot Scheme in Large-Scale Multicell Multiuser MIMO Systems” by Z. Luo et al., the authors propose a novel time-shift pilot scheme with asymptotic channel orthogonality to mitigate the pilot contamination in Large-Scale Multicell Multiuser MIMO systems. The proposed method considers the users within a cell to transmit the same pilot sequence in a time-shift manner enabling channel state information to be estimated without contamination. For different cells, pilot sequences are considered to be mutually orthogonal. Analysis of channel coefficient estimation, uplink data detection, and downlink data transmission steps shows that the proposed method alleviates the pilot contamination problem and improves the performance of the system significantly compared with the popular orthogonal pilots.

In “Connectivity Analysis of Millimeter-Wave Device-to-Device Networks with Blockage” by H. Jung and I.-H. Lee, the authors analyse the impact of blockage of the LoS on the direct and indirect device-to-device (D2D) communications in millimeter-wave cellular networks. The connectivity performance in terms of the probability to achieve a fully connected network and average number of reliably connected devices is evaluated. It is observed that both connectivity performance metrics decrease with an increase in network size and the blockage. The authors recommend use of a hybrid of direct and indirect communication to improve the two parameters by 35% based on simulation results.

In “Joint User Scheduling and MU-MIMO Hybrid Beamforming Algorithm for mmWave FDMA Massive MIMO System” by J. Jiang and D. Kong, the authors propose a joint user scheduling and multiuser hybrid beamforming algorithm for downlink massive MIMO Orthogonal Frequency Division Multiple Access (OFDMA) system. The users with identical optimal beams form an OFDMA user group and multiplex the entire frequency resource. The base station then allocates the frequency resources to each member of the group. Each of the user groups is regarded as a virtual user enabling support of arbitrary MU-MIMO user selection and beamforming algorithms. In the proposed technique, the analog beamforming vectors employ the best beam of each selected MU-MIMO user and the digital beamforming algorithm is solved by weight MMSE to acquire the maximum gain and mitigate interuser interference.

In “A Novel Simulator of Nonstationary Random MIMO Channels in Rayleigh Fading Scenarios” by Q. Zhu et al.,

the authors propose a new model for simulations of non-stationary MIMO Rayleigh fading channels in time-variant scattering environments. The simulator is based on the sum-of-sinusoids method to achieve low complexity and implementation simplicity. In order to reproduce realistic time varying statistics for dynamic channels, an efficient method to update frequency parameters is also proposed. Comparative analysis with theoretical models indicates that the proposed method generates channel statistics with good level of accuracy.

These papers provide a good overview of current research and development activities going on in the selected areas of millimeter-wave systems. The editors hope that this special issue will benefit the scientific community and contribute to the knowledge base.

Acknowledgments

The editors would like to take this opportunity to applaud the contribution of the authors to this special issue. Efforts of the reviewers to enhance the quality of the manuscripts are also much appreciated.

*Masood Ur-Rehman
Qammer Hussain Abbasi
Atiqur Rahman
Imdad Khan
Hassan Tariq Chattha
Mohammad Abdul Matin*

Research Article

Multiband Split-Ring Resonator Based Planar Inverted-F Antenna for 5G Applications

Muhammad Kamran Ishfaq,^{1,2} Tharek Abd Rahman,¹
Hassan Tariq Chattha,³ and Masood Ur Rehman⁴

¹Wireless Communication Centre, Universiti Teknologi Malaysia, Johor, Malaysia

²Department of Electrical Engineering, Government College University, Faisalabad, Pakistan

³Department of Electrical Engineering, Faculty of Engineering, Islamic University in Madinah, Al-Madinah, Saudi Arabia

⁴Department of Computer Science and Technology, University of Bedfordshire, Luton, UK

Correspondence should be addressed to Muhammad Kamran Ishfaq; kamranzarrar@gmail.com

Received 9 September 2016; Revised 1 January 2017; Accepted 2 March 2017; Published 21 March 2017

Academic Editor: Renato Cicchetti

Copyright © 2017 Muhammad Kamran Ishfaq et al. This is an open access article distributed under the Creative Commons Attribution License, which permits unrestricted use, distribution, and reproduction in any medium, provided the original work is properly cited.

5G, the fifth generation of wireless communications, is focusing on multiple frequency bands, such as 6 GHz, 10 GHz, 15 GHz, 28 GHz, and 38 GHz, to achieve high data rates up to 10 Gbps or more. The industry demands multiband antennas to cover these distant frequency bands, which is a task much more challenging. In this paper, we have designed a novel multiband split-ring resonator (SRR) based planar inverted-F antenna (PIFA) for 5G applications. It is composed of a PIFA, an inverted-L parasitic element, a rectangular shaped parasitic element, and a split-ring resonator (SRR) etched on the top plate of the PIFA. The basic PIFA structure resonates at 6 GHz. An addition of a rectangular shaped parasitic element produces a resonance at 15 GHz. The introduction of a split-ring resonator produces a band notch at 8 GHz, and a resonance at 10 GHz, while the insertion of an inverted-L shaped parasitic element further enhances the impedance bandwidth in the 10 GHz band. The frequency bands covered, each with more than 1 GHz impedance bandwidth, are 6 GHz (5–7 GHz), 10 GHz (9–10.8 GHz), and 15 GHz (14–15 GHz), expected for inclusion in next-generation wireless communications, that is, 5G. The design is simulated using Ansys Electromagnetic Suite 17 simulation software package. The simulated and the measured results are compared and analyzed which are generally in good agreement.

1. Introduction

5th-generation wireless systems, abbreviated as 5G, are the proposed next wireless communication standards beyond the current 4G/IMT-advanced standards. 5G will increase the user capacity up to many billion and the data rate up to 10 Gbps. It will support a real-time wireless control, the device-to-device communication, allowing a reduction of power consumption by a factor of 1000 [1–4]. This next generation of wireless communications is focusing on multiple bands in the frequency range from 6 GHz to 100 GHz [2, 5]. For 5G, the antennas for handheld devices will need to operate within multiple frequency bands, while being low-profile and compact. Hence, there is a need for compact multiband antenna design approach to cover these several frequency bands. Planar inverted-F antenna (PIFA) has been

a popular candidate in portable wireless systems due to its appealing features, such as low-profile, ease of fabrication, and robustness [6, 7], and it does not require any matching network when connected with the 50 Ω coaxial input [8]. A wide range of multiband PIFA designs for wireless applications is found in the literature [9–14]. Over the last decade, the multiband antennas used in cellular devices cover frequency bands which are comparatively closer to each other, that is, 900 MHz, 1.8 GHz, 2.45 GHz, and so forth. The design of a multiband antenna for covering the far away frequency bands such as 6 GHz, 10 GHz, 15 GHz, 28 GHz, and 38 GHz expected for 5G [5] is a task much more challenging. Therefore, in this paper, we have designed a multiband split-ring resonator (SRR) based modified PIFA with the additions of a rectangular shaped and an inverted-L shaped

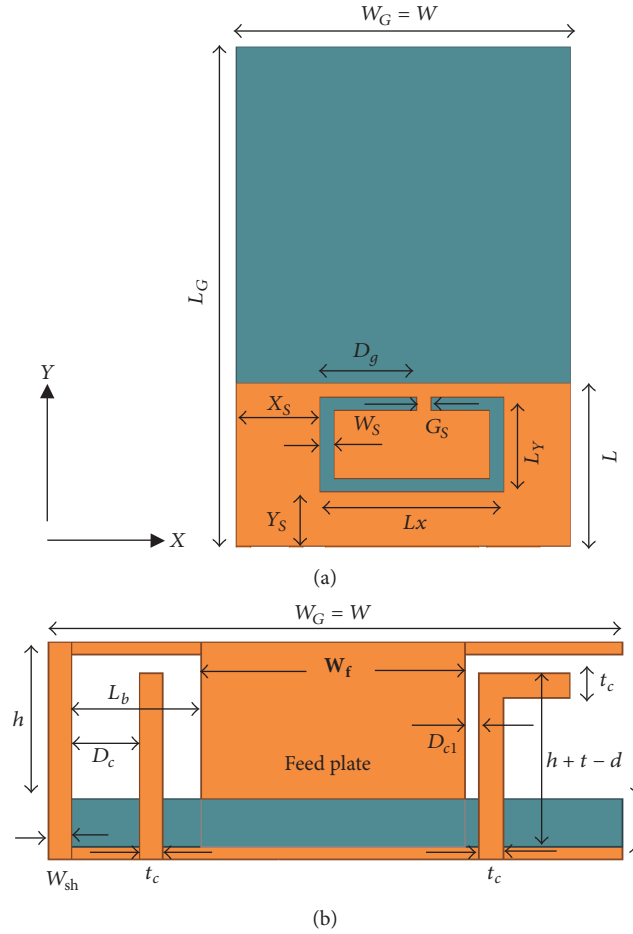


FIGURE 1: Geometry of an SRR based PIFA. (a) Top view; (b) side view.

parasitic element. It covers 6 GHz, 10 GHz, and 15 GHz, distant frequency bands, simultaneously, expected for 5G.

2. Antenna Configuration

The assembly of the designed PIFA is shown in Figure 1. It is composed of a radiating top plate of width W and length L and the ground plane of width W_G and length L_G . The height of the top plate above the substrate is h , filled with air. The sizes of the feeding and the shorting plates are $W_f \times h$ and $W_{sh} \times (h + t)$, respectively, where W_f is the width of the feeding plate, W_{sh} is the width of the shorting plate, and t is the thickness of the substrate. The separation between the feeding plate and the shorting plate is L_b . The substrate used is FR4, with a relative permittivity of 4.4 and a thickness $t = 1$ mm. An inverted-L shaped parasitic element is introduced at a separation of D_{c1} from the feeding plate, whereas a rectangular shaped parasitic element is inserted at a distance, D_c , from the shorting plate. The heights and the widths of both the inverted-L and rectangular shaped parasitic elements are identical and equal to $(h - d) + t$ and t_c , respectively, where d is the vertical gap between the top plate and the parasitic elements.

The top plate incorporates a split-ring resonator (SRR) introduced at a distance, X_S , from the horizontal edge and at a

distance, Y_S , from the vertical edge of the radiating top plate. W_S is the width of the SRR and L_X and L_Y are the lengths of the SRR along the horizontal and vertical sides of the top plate, respectively. The gap slot of the SRR is present at a distance, D_g , from the vertical side of the SRR. The fabricated prototype of the SRR based PIFA, for the measurement purpose, is shown in Figure 2. The antenna is excited by a semirigid cable in such a way that the braided outer conductor is shorted to the ground and the inner conductor is soldered to the feeding plate of the SRR based PIFA, as shown in Figure 2 [15]. An SMA connector is connected to the other end of the semirigid cable. This feeding mechanism reduces the coupling between the antenna and the SMA connector.

3. Design Approach and Parametric Study

For this multiband split-ring resonator based PIFA, a step by step design approach is adopted to attain the desired goals. Initially, a simple wideband PIFA is designed for 6 GHz frequency band. The wide bandwidth is achieved by adjusting the widths of the feeding and the shorting plates [16]. Further, an inverted-L shaped parasitic element is introduced towards the right side of the feeding plate so to shift the resonance at about 8 GHz. Next, a rectangular shaped parasitic element is inserted towards the right side of the shorting plate. The

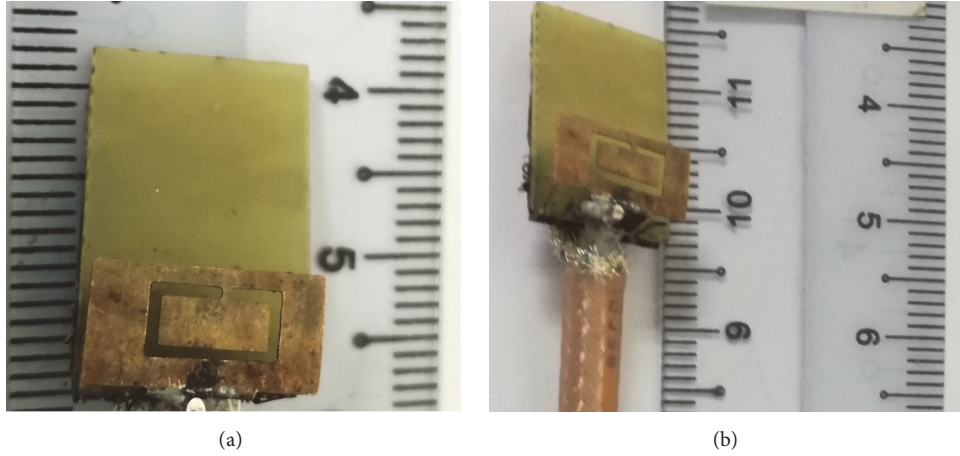


FIGURE 2: Fabricated SRR based PIFA for measurements. (a) Top view; (b) 3D view.

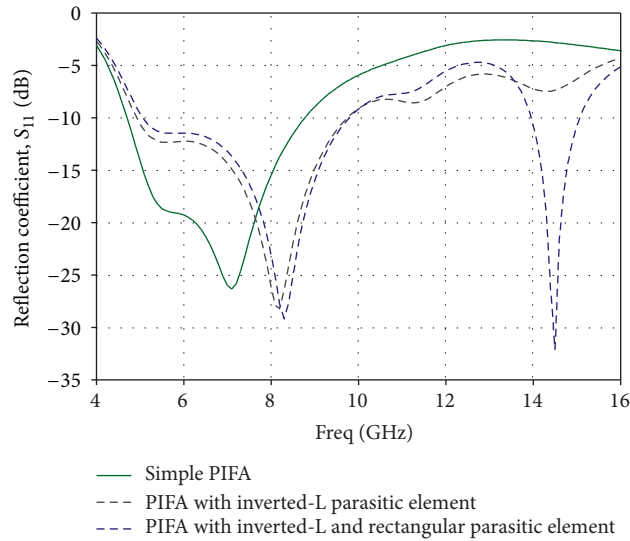


FIGURE 3: Magnitude of the simulated reflection coefficient of the PIFA with and without the inverted-L and rectangular shaped parasitic strips.

insertion of this parasitic element produces an additional resonance at around 15 GHz band. The optimized parameters up to this point of our step by step design approach are as follows: $W_G = 12$ mm, $L_G = 18.4$ mm, $W_{sh} = 0.5$ mm, $W = 12$ mm, $L = 6$ mm, $h = 3$ mm, $W_f = 5.5$ mm, $L_b = 2.7$ mm, $D_c = 0.3$ mm, $C_L = 1.4$ mm, $d = 0.4$ mm and $t_c = 0.5$ mm, and $D_{c1} = 1.4$ mm. Figure 3 shows the results for the above-mentioned design. To produce the required resonance at 10 GHz band, the study was started, initially, with the insertion of a slot at the top plate, which further led us to the design of a multiband PIFA with a split-ring resonator etched on its top plate. This design not only produces a required resonance at 10 GHz but also offers a band rejection at 8 GHz band.

To study the response of the split-ring resonator, an extensive parametric study is conducted in order to achieve the aforementioned design. The horizontal length of the SRR, L_X , is varied from 4.5 mm to 7.5 mm and all other parameters are held constant at $L_Y = 3.5$ mm, $W_S = 0.5$ mm, $X_S = 3$ mm,

$Y_S = 2$ mm, $G_S = 0.5$ mm, and $D_g = 3.5$ mm. Figure 4 shows that by varying L_X , the notched frequency band is varied. An increment in L_X decreases the notched frequency. On further investigations, a length $L_X = 6.6$ mm is chosen to obtain the required stop and pass frequency bands at around 8 and 10 GHz, respectively.

Similarly, D_g , the distance of the gap slot of the SRR from the vertical side of the SRR, is varied from 1.5 mm to 5.5 mm, while all other parameters are held constant at $L_X = 6.6$ mm, $L_Y = 3.5$ mm, $W_S = 0.5$ mm, $X_S = 3$ mm, $Y_S = 2$ mm, and $G_S = 0.5$ mm. It is observed that the notch band does not vary significantly with the variations in D_g ; however, the variations in the level of reflection coefficient S_{11} are important in pass-band near 10 GHz as shown in Figure 5. An increment in D_g slightly increases the second resonant frequency; however, after the value of $D_g = 3.5$ mm, a further increase in its value deteriorates S_{11} at that particular frequency. Therefore, the optimized value chosen for D_g is 3.5 mm.

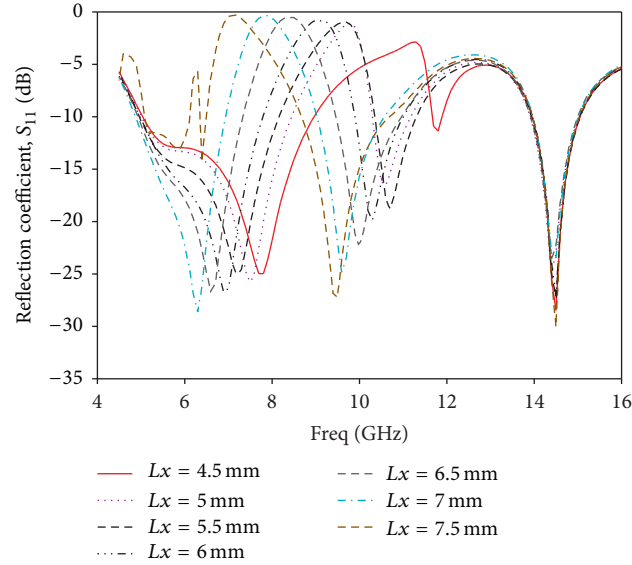


FIGURE 4: Magnitude of the simulated reflection coefficient of the PIFA versus frequency for different values of the geometrical parameter L_x .

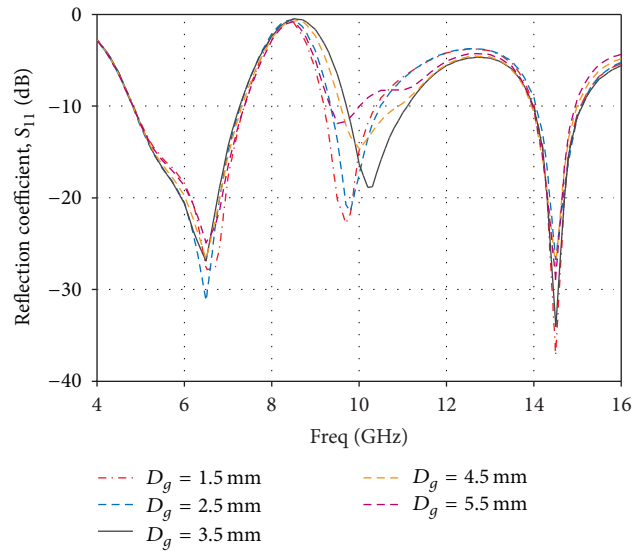


FIGURE 5: Magnitude of the simulated reflection coefficient of the PIFA versus frequency for different values of the geometrical parameter D_g .

Similarly, by increasing W_S the notch band and the second resonant frequency move towards a higher value as shown in Figure 6. This behaviour is due to the reason that an increase in the value of W_S decreases the current path length inside SRR and hence increases the rejection and passband frequency. Therefore, the final optimized design values for the SRR, chosen after extensive parametric study, are as follows: $L_X = 6.6$ mm, $L_Y = 3.5$ mm, $W_S = 0.5$ mm, $X_S = 3$ mm, $Y_S = 2$ mm, $G_S = 0.5$ mm, and $D_g = 3.5$ mm.

As discussed in [17], the surface current distribution is helpful towards explaining the phenomenon occurring due to the SRR. Therefore, the surface current distributions on the top plate of the SRR based PIFA excited at 8 GHz and 10 GHz

are shown in Figure 7. Figure 7(a) shows a strong surface currents distribution excited at 8 GHz causing an antiresonance at this frequency resulting in a band notch. Figure 7(b) shows a weaker surface current distribution excited at 10 GHz that results in a resonance at about 10 GHz.

We have observed that the insertion of a split-ring resonator with an inner perimeter of about 18 mm introduces a band rejection at a frequency around 8 GHz and further yields a resonance at 10 GHz. A highly sharp antiresonance occurs when the perimeter of the loop is about $\lambda/2$ [18]. Impedance results in Figure 8 show that an antiresonance occurs at around 8 GHz band. This is the reason towards the band notching at 8 GHz where the SRR perimeter is about

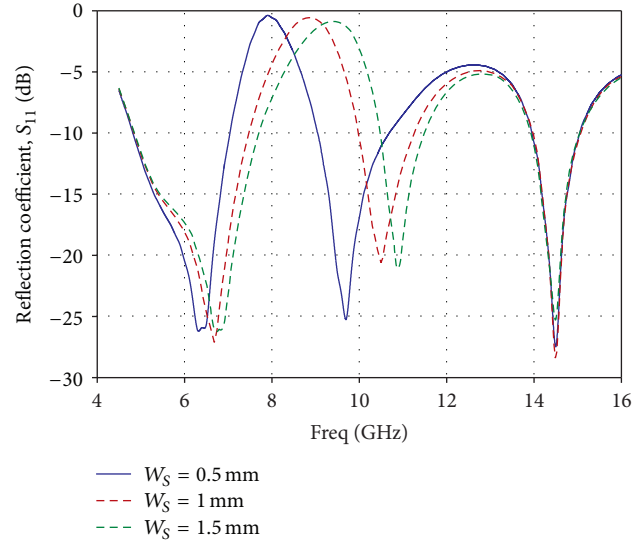


FIGURE 6: Magnitude of the simulated reflection coefficient of the PIFA versus frequency for different values of the geometrical parameter W_S .

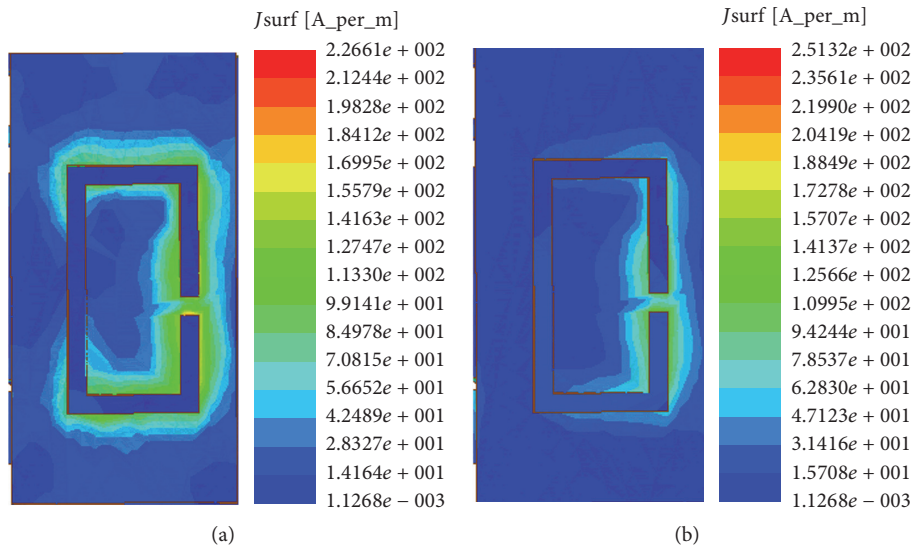


FIGURE 7: Surface current distribution on the top plate at (a) 8 GHz and (b) 10 GHz.

$\lambda/2$. And it starts resonating at around 10 GHz where its perimeter $> 0.6\lambda$. It is observed that the inverted-L and the SRR together provide a resonance at 10 GHz band.

4. Results and Discussion

The split-ring resonator based PIFA design has been simulated and optimized using Ansys Electromagnetics Suite 17.0 simulator package. The final optimized design parameters are as follows: $W_G = 12$ mm, $L_G = 18.4$ mm, $W_{sh} = 0.5$ mm, $W = 12$ mm, $L = 6$ mm, $h = 3$ mm, $W_f = 5.5$ mm, $L_b = 2.7$ mm, $L_X = 6.6$ mm, $L_Y = 3.5$ mm, $W_S = 0.5$ mm, $X_S = 3$ mm, $Y_S = 2$ mm, $G_S = 0.5$ mm, $D_g = 3.5$ mm, $D_c = 0.3$ mm, $C_L = 1.4$ mm, $d = 0.4$ mm and $t_c = 0.5$ mm, and $D_{c1} = 1.4$ mm. Figure 9 shows the simulated and the measured results for reflection

coefficient S_{11} . The S_{11} results show that the antenna covers simultaneously the 6 GHz band (4.8 GHz to 7 GHz), the 10 GHz band (9.5 to 10.8 GHz), and the 15 GHz band (14-15 GHz). The simulated and the measured results show generally a very good agreement. Figure 10 shows the simulated and the measured radiation patterns of this antenna at $\phi = 0^\circ$ and $\phi = 90^\circ$. The radiation patterns of this antenna are measured in an anechoic chamber. The maximum gains of this antenna at the frequencies 6 GHz, 10 GHz, and 15 GHz are 3.4 dBi, 4.9 dBi, and 5.85 dBi, respectively.

5. Conclusion

A novel multiband SRR based modified PIFA design has been proposed. The antenna operated at the frequency

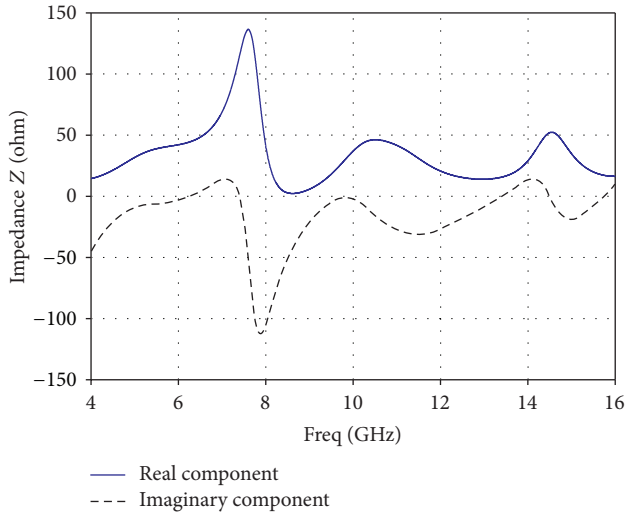


FIGURE 8: Impedance Z (Ω) versus frequency (GHz).

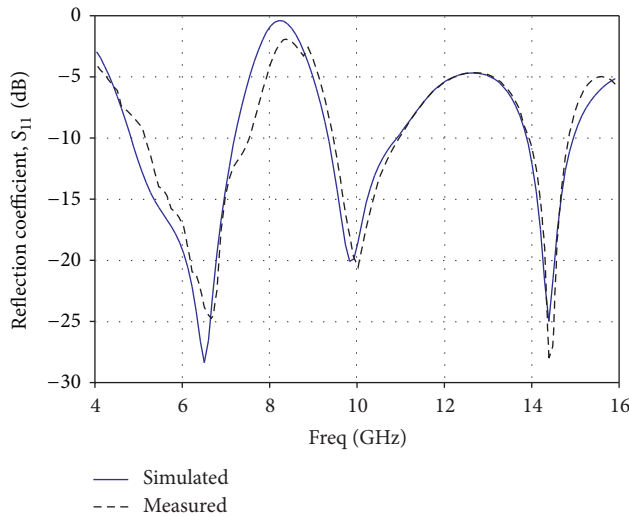


FIGURE 9: Magnitude of the simulated and measured reflection coefficient S_{11} (dB) versus frequency (GHz) for SRR based PIFA.

bands located at 6 GHz, 10 GHz, and 15 GHz, expected to be included in the upcoming 5G wireless communication standards. It was observed that an SRR with a width of 0.5 mm, etched on the top plate of the PIFA, having a perimeter, $\lambda/2$, provided a band rejection around 8 GHz. It also provided a resonance around 10 GHz band, where the SRR perimeter was greater than or equal to about 0.6λ . The SRR based PIFA with the parasitic elements radiated at 6 GHz, 10 GHz, and 15 GHz bands in such a way that the basic PIFA structure radiated at 6 GHz, whereas the inclusion of an SRR etched on the top plate, and inverted-L parasitic element together caused a radiation at 10 GHz band. Further, an insertion of a rectangular parasitic element caused the antenna to radiate at 15 GHz band. When the perimeter of the SRR became equal to $\lambda/2$ at 8 GHz, the antenna radiated poorly causing a sharp gain drop. This happened because an antiresonance occurred at this particular frequency. For the resonant frequency bands

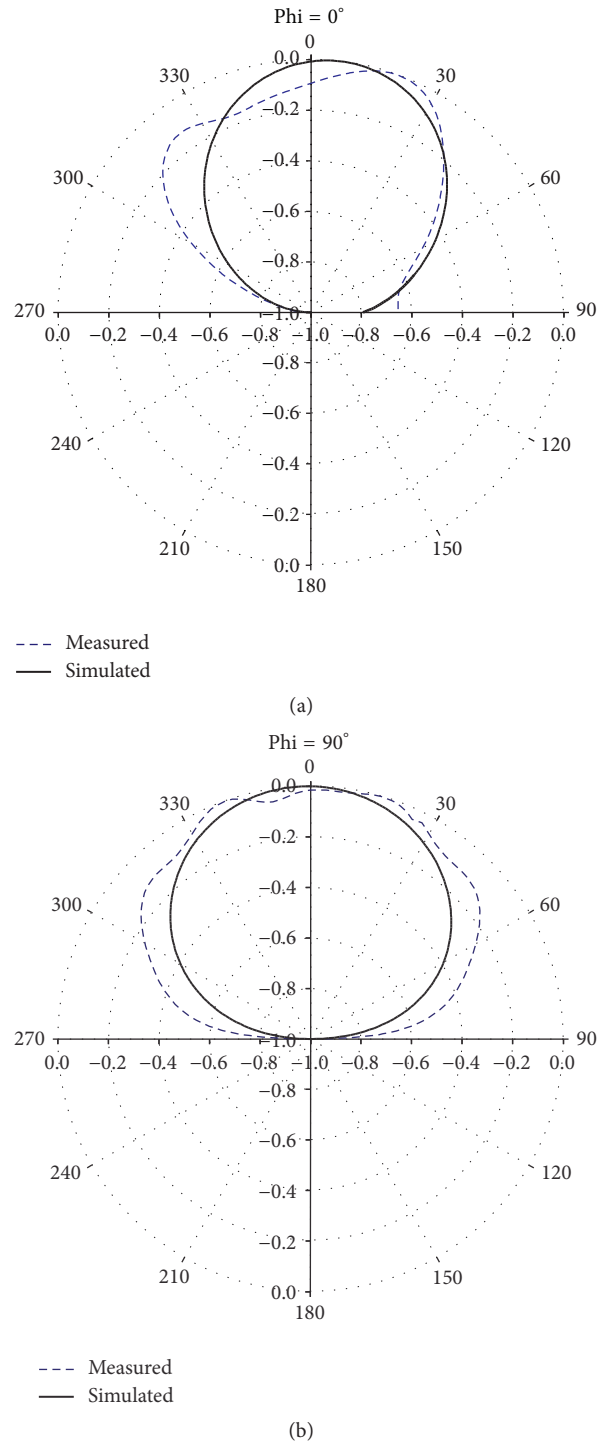


FIGURE 10: Simulated and measured 2D radiation patterns of SRR based PIFA for 6 GHz at (a) $\phi = 0^\circ$ and (b) $\phi = 90^\circ$.

of 6, 10, and 15 GHz, the peak gains were 3.4 dBi, 4.9 dBi, and 5.85 dBi, respectively.

Conflicts of Interest

The authors declare that there are no conflicts of interest regarding the publication of this paper.

References

- [1] J. G. Andrews, S. Buzzi, W. Choi et al., "What Will 5 G Be?" *IEEE Journal on Selected Areas in Communications*, vol. 32, no. 6, pp. 1065–1082, 2014.
- [2] Q. Wang, B. Ai, K. Guan, D. W. Matolak, R. He, and X. Zhou, "Ray-based statistical propagation modeling for indoor corridor scenarios at 15 GHz," *International Journal of Antennas and Propagation*, vol. 2016, Article ID 2523913, 12 pages, 2016.
- [3] G. Fettweis and S. Alamouti, "5G: personal mobile internet beyond what cellular did to telephony," *IEEE Communications Magazine*, vol. 52, no. 2, pp. 140–145, 2014.
- [4] F. Khan, Z. Pi, and S. Rajagopal, "Millimeter-wave mobile broadband with large scale spatial processing for 5G mobile communication," in *Proceedings of the 50th Annual Allerton Conference on Communication, Control, and Computing (Allerton '12)*, pp. 1517–1523, IEEE, October 2012.
- [5] Ofcom, *Spectrum above 6 GHz for Future Mobile Communications*, Ofcom, London, UK, 2015.
- [6] H. T. Chattha, Y. Huang, M. K. Ishfaq, and S. J. Boyes, "A Comprehensive Parametric Study of planar inverted-F antenna," *Scientific Research Wireless Engineering and Technology*, vol. 3, no. 1, pp. 1–11, 2012.
- [7] H. T. Chattha, Y. Huang, M. K. Ishfaq, and S. J. Boyes, "Bandwidth enhancement techniques for planar inverted-F antenna," *IET Microwaves, Antennas & Propagation*, vol. 5, no. 15, pp. 1872–1879, 2011.
- [8] P. Li, J. Pan, D. Yang, and P. Nie, "A novel dual-shortening point PIFA (GSM850 to IMT-A) for mobile handsets," *International Journal of Antennas and Propagation*, vol. 2013, Article ID 436808, 7 pages, 2013.
- [9] N. Chattoraj, J. Qurratulain, S. Agarwal, and K. V. Singh, "Design of a novel dual: band planar inverted F-antenna for mobile radio applications," *Journal of Microwaves, Optoelectronics and Electromagnetic Applications*, vol. 13, no. 2, pp. 177–184, 2014.
- [10] J. Yang, X.-L. Li, and W.-L. Zhao, "Triple broadband compact planar inverted F antenna for WLAN and WiMAX," *Journal of China Universities of Posts and Telecommunications*, vol. 17, no. 1, pp. 32–36, 2010.
- [11] H. T. Chattha, M. K. Ishfaq, Y. Saleem, Y. Huang, and S. J. Boyes, "Band-notched ultrawide band planar inverted-F antenna," *International Journal of Antennas and Propagation*, vol. 2012, Article ID 513829, 6 pages, 2012.
- [12] K. R. Boyle and P. G. Steenekken, "A five-band reconfigurable PIFA for mobile phones," *IEEE Transactions on Antennas and Propagation*, vol. 55, no. 11, pp. 3300–3309, 2007.
- [13] H. T. Chattha, Y. Huang, Y. Lu, and X. Zhu, "An ultra-wideband planar inverted-F antenna," *Microwave and Optical Technology Letters*, vol. 52, no. 10, pp. 2285–2288, 2010.
- [14] M. S. Ahmad, C. Y. Kim, and J. G. Park, "Multishortening pins PIFA design for multiband communications," *International Journal of Antennas and Propagation*, vol. 2014, Article ID 403871, 10 pages, 2014.
- [15] H. Jian-rong, L. Jiu-sheng, and W. Di, "A small planar antenna for 4G mobile phone application," *International Journal of Antennas and Propagation*, vol. 2016, Article ID 4791831, 7 pages, 2016.
- [16] H. T. Chattha, Y. Huang, and Y. Lu, "PIFA bandwidth enhancement by changing the widths of feed and shorting plates," *IEEE Antennas and Wireless Propagation Letters*, vol. 8, pp. 637–640, 2009.
- [17] D. Caratelli, R. Cicchetti, G. Bit-Babik, and A. Faraone, "A perturbed E-shaped patch antenna for wideband WLAN applications," *IEEE Transactions on Antennas and Propagation*, vol. 54, no. 6, pp. 1871–1874, 2006.
- [18] C. A. Balanis, *Antenna Theory: Analysis and Design*, John Wiley & Sons, 3rd edition, 2005.

Research Article

Millimeter-Wave Microstrip Antenna Array Design and an Adaptive Algorithm for Future 5G Wireless Communication Systems

Cheng-Nan Hu,¹ Dau-Chyrh Chang,¹ Chung-Hang Yu,²
Tsai-Wen Hsaio,² and Der-Phone Lin²

¹Communication Engineering Department, OIT, New Taipei City 22061, Taiwan

²National Chung-Shan Institute of Science and Technology, P.O. Box 90008, Longtan, Taoyuan City, Taiwan

Correspondence should be addressed to Cheng-Nan Hu; fo011@mail.oit.edu.tw

Received 9 September 2016; Accepted 14 November 2016

Academic Editor: Atiqur Rahman

Copyright © 2016 Cheng-Nan Hu et al. This is an open access article distributed under the Creative Commons Attribution License, which permits unrestricted use, distribution, and reproduction in any medium, provided the original work is properly cited.

This paper presents a high gain millimeter-wave (mmW) low-temperature cofired ceramic (LTCC) microstrip antenna array with a compact, simple, and low-profile structure. Incorporating minimum mean square error (MMSE) adaptive algorithms with the proposed 64-element microstrip antenna array, the numerical investigation reveals substantial improvements in interference reduction. A prototype is presented with a simple design for mass production. As an experiment, HFSS was used to simulate an antenna with a width of 1 mm and a length of 1.23 mm, resonating at 38 GHz. Two identical mmW LTCC microstrip antenna arrays were built for measurement, and the center element was excited. The results demonstrated a return loss better than 15 dB and a peak gain higher than 6.5 dBi at frequencies of interest, which verified the feasibility of the design concept.

1. Introduction

The growing demands on data traffic are propelling the evolution of wireless standards. Soon after the first forzon release in December 2008, commercial development of the 3rd-Generation Partnership Project (3GPP) Long-Term Evolution (LTE) system began. To increase capacity, LTE-Advanced was launched in March 2011, rendering LTE formally compliant with the International Telecommunication Union's definition of the fourth generation of wireless technology, termed IMT-Advanced [1, 2]. However, new traffic types and data services are emerging, notably machine-to-machine communications to support applications such as smart grid, smart homes and cities, and e-health. With the development of new applications, as many as 50 billion devices may be connected by 2020 according to one estimate [3]. The growing annual traffic demands (conservative estimates range from 40% to 70% [4–6]) imply that cellular networks may need to deliver as much as 1000 times their current capacity within the next decade. The challenging task of meeting this demand

impels the development of future wireless networks, called beyond fourth-generation (4G) and fifth-generation (5G) cellular systems, offering peak throughputs of multigigabits per second (Gb/s) and cell edge rates in tens of megabits per second (Mb/s) [7].

In addition to offering greater performance than LTE-Advanced, future networks must be much more energy efficient than current networks for 5G technology to be sustainable in the long term. Millimeter-wave (mmW) beam-forming technology is a key enabling factor for the data capacity improvement that is essential for 5G networks to be commercially successful. This technology employs a massive multi-input multioutput (MIMO) system operating between 30 and 300 GHz, where the available bandwidths are much wider than current cellular networks [8–11]. The new spectrum released by the Federal Communications Commission features bandwidth up to 11 GHz, including 3.8 GHz of licensed spectrum from 27.5 to 28.35 GHz and 37 to 40 GHz and 7 GHz of unlicensed spectrum from 64 to 71 GHz. The available spectrum of the mmW band can achieve data rates

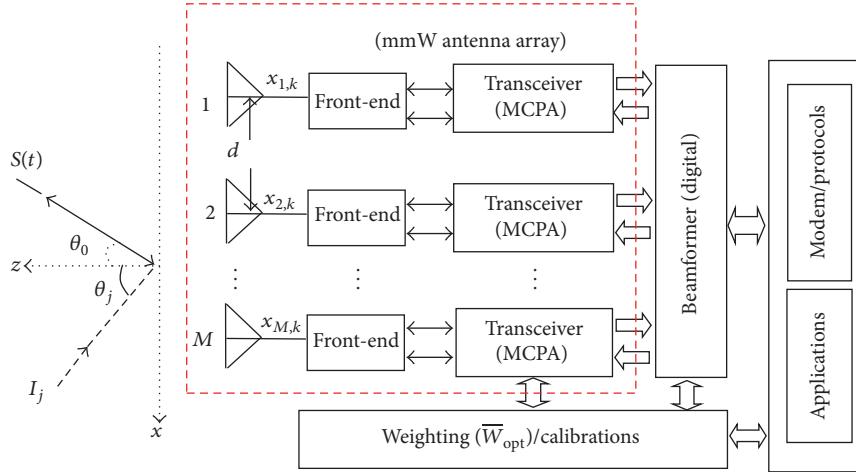


FIGURE 1: The functional block diagram of an adaptive antenna array for massive MIMO systems.

200 times greater than those realized by current cellular systems under 3 GHz [8, 10]. Furthermore, the relatively short wavelength of an mmW signal, which incorporates leading radiofrequency integrated circuit technologies, renders the implementation of an antenna with numerous (≥ 32) elements with small dimension possible. Consequently, future wireless networks can be equipped with massive MIMO systems to provide an extremely high gain, electrically steerable array, and adaptive beamforming arrays. Furthermore, these systems can be built in the base station, on the terminal device, or within a chip [8, 12].

Despite the benefits of using the mmW band, numerous substantial challenges must be addressed before the wireless systems in these bands can be realized, especially for the array antenna design.

- (1) In the mmW region, designing electromagnetic circuit elements is difficult because of the sensitivity in fabrication requirements and the high insertion loss in wave propagation. Slight misalignments of parameters on the order of 0.1 mm can change the characteristics of the circuit element and cause unexpected consequences.
- (2) Greater antenna gain for the same physical antenna size is attained because of the smaller wavelength of the mmW signal. However, the reliance on highly directional transmissions necessitates design changes to current cellular systems [13].
- (3) Fabricating structures and fixing connectors when transitioning to the other transmission lines require care. The fringing fields over the transition region on the panel launch transmission line feed have capacitive or inductive input impedance resulting in distortion and poor matching performance.

This paper reports on the recent progress in designing a prototype mmW antenna array for massive MIMO applications; the array involves a 64-element microstrip antenna array operating at 38 GHz. In Section 2.1, the system

configuration of the proposed mmW microstrip antenna array is discussed in detail. This section also outlines the minimum mean square error [14, 15] and least mean squares (LMS) [14] adaptive algorithms, which show great improvement in signal-to-noise ratio (SNR) by placing nulls in interference directions. Section 2.2 presents the design of a prototype mmW antenna array using a microstrip patch antenna printed on a low-temperature cofired ceramic (LTCC) substrate. Section 3 describes the experimental study of the mmW microstrip antenna arrays, namely, 64-element microstrip patch antennas and a reference antenna for self-calibration [16]. Concluding remarks are provided in Section 4.

2. Analysis and Design

2.1. System Configuration. The functional block diagram of an M -element massive MIMO system for future networks is depicted in Figure 1. During transmission, the optimal weighting vector (\mathbf{W}_{opt}) is computed to generate high gain radiation fields along the signal directions (θ_0, ϕ_0) and synthesize nulls on other unlined user equipment (UE) directions (θ_j, ϕ_j); this minimizes channel interference. Therefore, when the SNR increases, a high-quality signal is achieved in the radio line between BS and UE for high-throughput performance. Similarly, the incoming signal and interference in the directions received by the array are amplified, down-converted, and transformed to the baseband signal from analog to digital format. While the radiation pattern is synthesized with the high gain in the signal direction and nulls in the interference directions, a closed-loop adaptive processor modifies the received signals in a fading environment by computing the optimal weighting vector (\mathbf{W}_{opt}). An equally spaced d -space M -element antenna array is subjected to this process.

Figure 2 illustrates the design concept of the proposed mmW active antenna array for massive MIMO systems, indicating that it comprises the following components: (1) 64-element microstrip patch antennas; (2) 16 front-end modules;

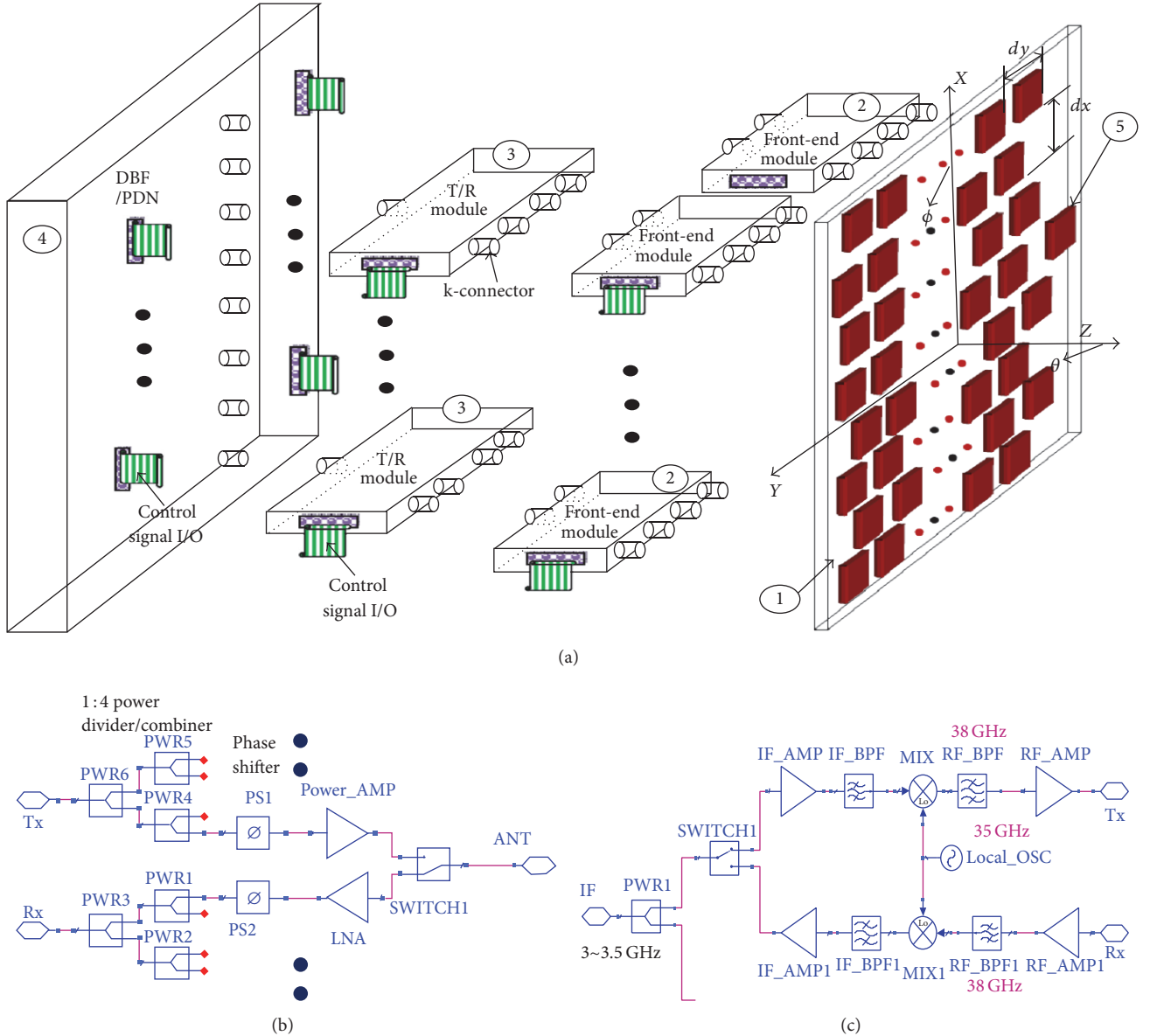


FIGURE 2: (a) Design concept of the mmW active antenna array for massive MIMO systems, comprising (1) 64-element microstrip patch antennas, (2) 16 front-end modules, (3) eight T-R modules, (4) an eight-channel digital beamforming network and power distribution network, and (5) a reference antenna integrated with a T-R module. (b) Schematic of the front-end module on one channel. (c) Schematic of the T-R module on one channel.

(3) eight transmitter-receiver (T-R) modules; (4) a power distribution network; and (5) a reference antenna integrated with a T-R module, which is applied to the system self-calibration using the phase-match method [16].

The antenna array comprises a set of polarized elements in the position vector ($\mathbf{D} = [\mathbf{d}_1, \mathbf{d}_2, \dots, \mathbf{d}_m, \dots, \mathbf{d}_M]$), where \mathbf{d}_m denotes the location of the m th antenna element. For plane waves that propagate in a locally homogeneous medium, the wave \mathbf{K} is defined as

$$\mathbf{K} = \frac{2\pi}{\lambda} [\sin \theta \cos \phi \quad \sin \theta \sin \phi \quad \cos \theta]^T, \quad (1)$$

where λ represents the wavelength at frequency f ; θ and ϕ are the azimuthal angle and angle of elevation of the far-field source, respectively; and T denotes the matrix transpose.

When the time phase factor $e^{j2\pi ft}$ is omitted, the far-field pattern of the simultaneously excited adaptive antenna array becomes

$$f(\theta, \phi) = \mathbf{W}^H \cdot e^{-j\mathbf{K}^T \cdot \mathbf{D}} \xi(\theta, \phi) = \mathbf{W}^H \cdot \mathbf{E}(\theta, \phi), \quad (2)$$

where

$$\mathbf{W} = [w_1, w_2, \dots, w_M]^T, \quad (3)$$

$$\mathbf{E}(\theta, \phi) = \mathbf{e}^{-j\mathbf{K}^T \cdot \mathbf{D}} \xi(\theta, \phi).$$

The polarized element pattern function for an individual element is denoted by $\xi(\theta, \phi)$, and w_i ($w_i = c_i e^{j\psi_i}$) represents the complex weighting coefficient with an amplitude of c_i and phase of ψ_i at the i th element of the weight vector \mathbf{W} , which is generated by the adaptive algorithm. The Hermitian transpose, which combines transposition and conjugation, is denoted by \mathbf{H} , and the radiation pattern of the array is denoted by $f(\theta, \phi)$. For a given radial vector (defined by angles ϕ and θ), $f(\theta, \phi)$ yields the magnitude of the array response in the $\hat{\phi}$ and $\hat{\theta}$ directions.

The system performance enhancement of the massive MIMO system was assessed using adaptive algorithms in a noisy environment. The received signal of a single antenna in an additive white Gaussian noise channel is represented by $x(t) = S(t) + n(t)$, where $S(t)$ denotes the received signal in the direction (θ_0, ϕ_0) and $n(t)$ denotes the noise. The adaptive beamformer with the selected algorithm is then derived using the conventional phased array approach at radiofrequency (RF) or intermediate frequency (IF) [14, 15]. The signals collected from each of the antenna elements are processed and summed in the analog devices and downconverted to the baseband. The weighting process in the RF and IF analog domains is relatively inflexible and can become complex as the number of space-division multiple-access channels increases. The digital-domain, or digital beamforming (DBF), approach has numerous advantages [17, 18] but is also disadvantaged by its unavailability, high cost, increased signal bandwidth, and the dynamic range of characteristics of analog-to-digital and digital-to-analog converters.

In this paper, the mean squared error (MSE) is minimized by using the LMS algorithm [14, 19, 20] as an example of selected adaptive DBF. In discrete time, at time index k and period T_s , $t = kT_s$, the input signal vector of an equally spaced M -element array (Figure 1) is

$$\mathbf{X}_k = [x_{1,k}, x_{2,k}, \dots, x_{m,k}, \dots, x_{M,k}], \quad (4)$$

where $x_{m,k}$ is the transmitted narrowband signal in a complex envelope and m is the number of antenna elements at k . Moreover, \mathbf{W}_k is the weight vector at k , which can be applied in the analog portion of the receiver using phase shifters and attenuators, or in the digital domain after digitizing and filtering the signal. For narrowband arrays, the output is the linear combination of the sampled inputs that are multiplied with complex weights:

$$y_k = \mathbf{X}_k^H \cdot \mathbf{W}_k. \quad (5)$$

The optimal solution that minimizes MSE leads to the Wiener-Hopf solution [14] and is given by

$$\mathbf{W}_k = \mathbf{R}_{xx}^{-1} \cdot \mathbf{r}_{xd}, \quad (6)$$

where \mathbf{R}_{xx} denotes the input correlation or covariance matrix and \mathbf{r}_{xd} is the cross-correlation vector between the received and training (or desired) signals.

For stationary input data, the process requires only the time to yield adequate estimates of \mathbf{R}_{xx} and \mathbf{r}_{xd} . \mathbf{R}_{xx}^{-1} is then computed and the optimal weight vector is determined. However, because matrix inversion is nontrivial, particularly when conducted using a digital signal processor, iterative techniques easily yield the optimal solution in a limited time. The updated equation of these iterative approaches is generally expressed by the LMS algorithm [18] given by

$$\mathbf{W}_{k+1} = \mathbf{W}_k - \Delta (\mathbf{G}_k), \quad (7)$$

where Δ represents the step-size value and is allowed to change at every iteration and \mathbf{G}_k denotes the gradient or derivative of the MSE with respect to the weight vector (\mathbf{W}_k):

$$\mathbf{G}_k = -2\mathbf{r}_{xd} + 2\mathbf{R}_{xx}\mathbf{W}_k. \quad (8)$$

Stochastic gradient algorithms attempt to determine the optimal solution by continually stepping in the negative direction of the gradient. Thus, the weight vector is adjusted toward the minimum optimal MSE surface. Therefore, the adaptive weighting vector can be computed with the DBF unit (Figure 1) by using (7); the adaptive weighting vector is then fed into transceivers to adjust the amplitude and phase of each patch antenna through the automatic gain controller and phase shifter. Consequently, the far-field pattern of the simultaneously excited adaptive antenna array can be achieved and the SNR can be maximized to optimize the system performance under fading environments.

Figure 3(a) indicates that the computed element gain of a single patch antenna of 6.86 dBi, which is achieved using HFSS and the theoretical directivity gain improvement for a massive MIMO system with a 64-element array antenna and element spacing of $dx = 5.5$ mm and $dy = 8.5$ mm, is 18 dB according to (2). The beamwidth of the array pattern is approximately 5° and 6° on the Az- and El-planes (x - z and y - z planes), respectively, and $\pm 25^\circ$ beams are capable of electronic steering in the coverage region. Furthermore, when the MSE adaptive algorithms in (5) and (6) are applied, the massive MIMO can synthesize the radiation pattern with nulls in the interference directions (i.e., $(\theta, \phi) = (13^\circ, 0^\circ)$, $(30^\circ, 0^\circ)$, $(50^\circ, 0^\circ)$) to increase the system SNR (Figure 3(b)). Figures 3(c) and 3(d) illustrate plots of the 3D and 2D contour radiation patterns of the array, respectively.

2.2. Microstrip Antenna Array Design. Considering the drawbacks of working at the Ka band frequencies discussed in Section 1, we employed the microstrip antennas for this prototype study because the manufacturing process for microstrip type antenna, with the help of modem-printed circuit technology adapted to testing and constructing purposes, is simpler, less expensive, and faster than that of other types of antennas. Moreover, if manufactured carefully, the products are almost identical, implying that verification of the design microstrip prototype antenna will also be satisfactory for other copies of the antenna. However, the microstrip antennas have notable disadvantages, such as low power handling and narrow frequency bandwidth.

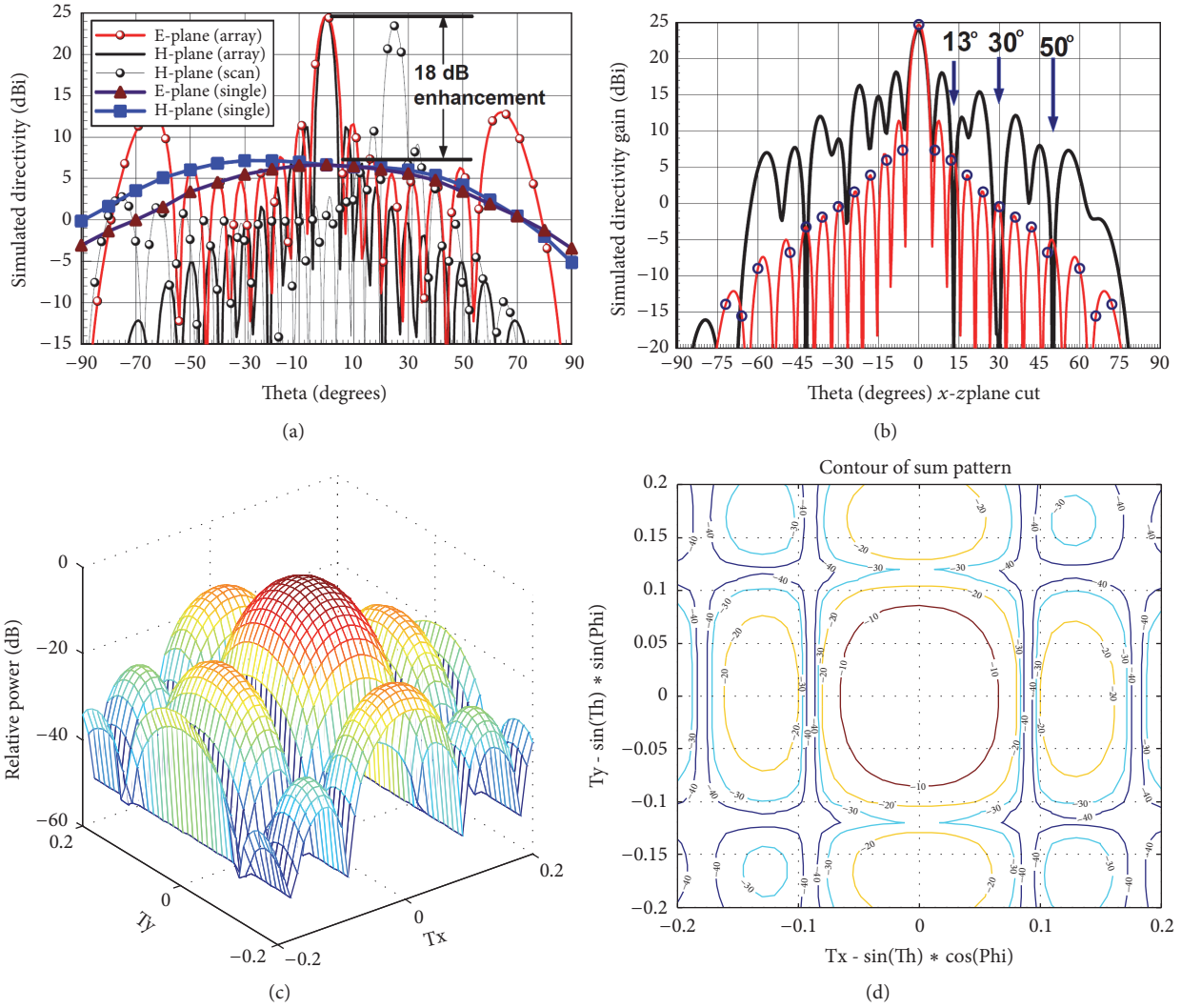


FIGURE 3: (a) Comparison of the simulated radiation patterns of a single antenna using HFSS and a 64-element array antenna with element spacing of $dx = 5.5$ mm and $dy = 8$ mm through (2) in E- and H-planes (x - z and y - z planes). (b) Comparison of the H-plane radiation pattern with and without the adaptive algorithm, demonstrating the nulls on the interference directions (θ° and ϕ°) of 13° and 0° , 30° and 0° , and 50° and 0° , respectively. (c) 3D radiation pattern of the array. (d) 2D contour of the radiation patterns.

Many feeding design methods can be applied to excite microstrip patch antennas, but a perpendicular coaxial transition is the most suitable for mmW applications, because this method's measurements indicate a return loss better than 14 dB and an insertion loss better than 0.4 dB from DC to 40 GHz [21, 22]. Therefore, we proposed the mmW antenna array comprising 64-element perpendicular coax-fed microstrip patch antennas that resonate at 38 GHz (Figure 4). The mmW microstrip patch array is integrated with eight subarrays, each comprising eight microstrip patches printed on the RF substrate with a thickness of 15 mil. The element spacing of the array is arranged in a triangular lattice ($dx = 5.5$ mm; $dy = 8.5$ mm) to obtain a beam scanning azimuth angle of $\pm 25^\circ$ when maintaining maximum room to allocate the modified k-connector.

A key parasite of perpendicular transition is the inductance triggered by ground currents that must flow around the circumference of the coax outer conductor to reach

the underside of the microstrip section. Therefore, in each subarray, substrates with the printed microstrip patches were soldered on a modified k-connector with four ground pins on the four corners of the connector base to secure the antenna (Figure 5(a)). After all of the subarrays were integrated, nine screws were used to fix the RF substrate of each subarray onto the back plane of the array (Figure 5(b)). Subsequently, the array was placed in a tin stove for wave soldering reflow. After all subarrays were soldered on the back plane of the array, all of the screws were removed.

3. Numerical and Experimental Study

The design approach of the microstrip patch printed on the LTCC substrate with a dielectric constant of 5.9 and thickness of 15 mil was verified using HFSS (Figure 6). The transition effects of the coaxially fed launcher were considered in the simulation.

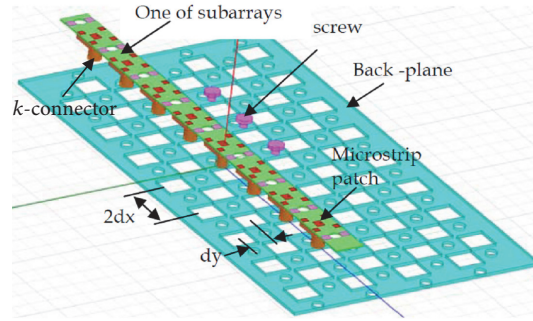


FIGURE 4: Design concept of the proposed mmW microstrip antenna array.

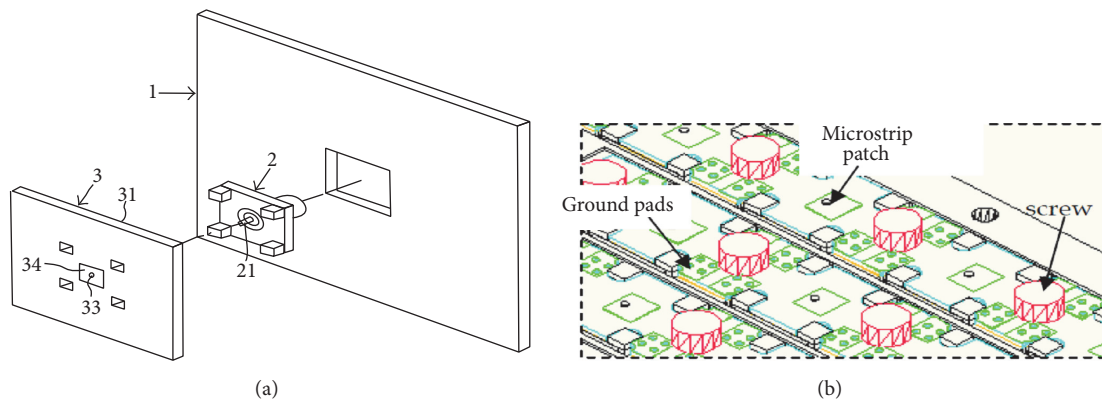


FIGURE 5: (a) Design of a single microstrip patch. (b) Close look of the assembled array.

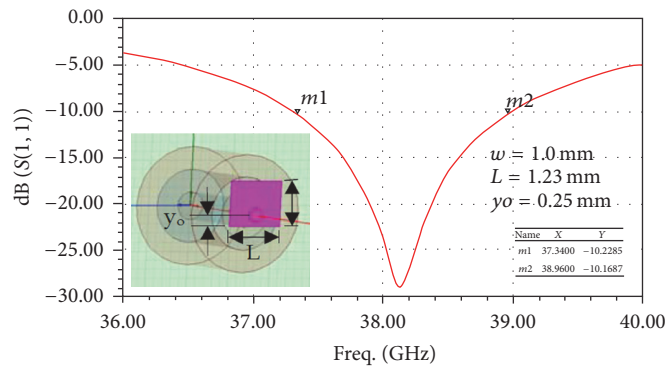


FIGURE 6: Simulated S_{11} of a single microstrip antenna patch; inset shows the simulation layout.

The simulation results (Figure 6) showed a return loss of less than 10 dB at the frequencies of interest ranging from 37.34 to 38.89 GHz. To experimentally verify this design approach, two identical mmW microstrip patch antenna arrays were built for testing (Figure 7). The measurement setup was established by connecting one patch with two mmW microstrip patch arrays, which were placed face-to-face 19.5 cm apart (Figure 8).

Two-port S-parameters were measured using the Rohde & Schwarz ZVA40 vector network analyzer (Figure 9). The simulated S_{11} (solid line in Figure 9) was computed using a single microstrip patch to reduce computing time but the measured S_{11} (the solid line with diamond shapes) and S_{22} (the solid line with rectangular shapes) corresponded to the center element of two microstrip antenna arrays (Figure 8). Thus, the discrepancy between the measured and simulated

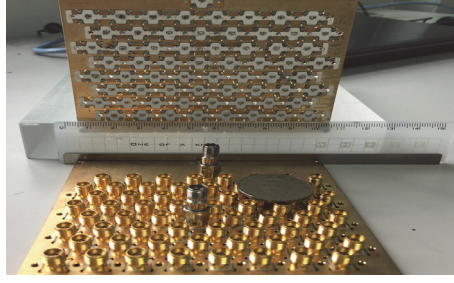


FIGURE 7: Photograph of two identical mmW microstrip arrays for testing.

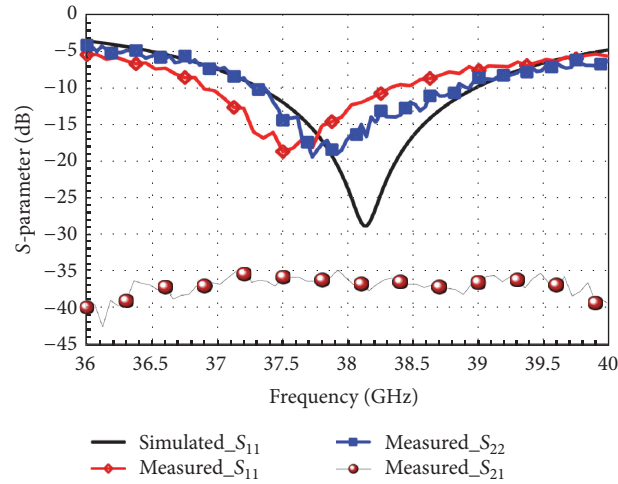

 FIGURE 8: Measurement setup established by connecting one patch to two arrays, placing two arrays face-to-face at a distance of $R = 19.5$ cm, and testing the 2-port S-parameters using the Rohde & Schwarz ZVA40 vector network analyzer.


FIGURE 9: Measured S-parameters of the test setup (Figure 8).

data (Figure 9) can be attributed to the reactive loading effect caused by the mutual coupling.

Next, the Friis power transmission formula [23] was used to calculate the maximum antenna power gain (in the central forward direction of the antenna):

$$\mathbf{G}_r \mathbf{G}_t = \mathbf{G}^2 = \left(\frac{\mathbf{P}_r}{\mathbf{P}_t} \right) \left(\frac{4\pi\mathbf{R}}{\lambda_0} \right)^2 = |\mathbf{S}_{21}|^2 \left(\frac{4\pi\mathbf{R}}{\lambda_0} \right)^2, \quad (9)$$

where \mathbf{G}_r and \mathbf{G}_t are the power gains of the receiving and transmitting antennas, respectively, and \mathbf{P}_t and \mathbf{P}_r are the transmitted and received powers, respectively. Because the

two antennas are identical, $\mathbf{G}_t = \mathbf{G}_r = \mathbf{G}$, and the power ratio $\mathbf{P}_r/\mathbf{P}_t$ is the measured direct transmission coefficient $|\mathbf{S}_{21}|^2$, which was obtained using the vector network analyzer. By substituting the measured $|\mathbf{S}_{21}|$ into (9), the measured maximum antenna power gain was plotted against frequencies ranging from 36.0 to 40 GHz to compare with simulation data (Figure 10); they indicated an acceptable agreement. The measured gain of a single microstrip patch was approximately 6.8 dBi at 38 GHz.

Finally, the radiation pattern at the center element of the prototype mmW array (Figure 7) was measured at OIT

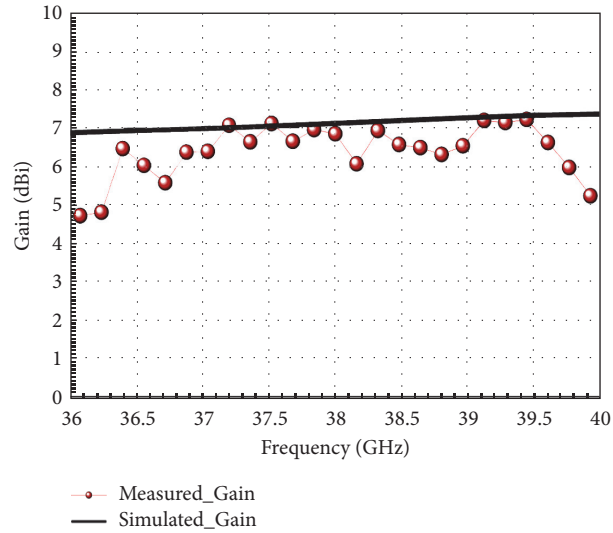


FIGURE 10: Comparison of the gain measured by (9) and the gain simulated using HFSS on a single microstrip patch antenna.

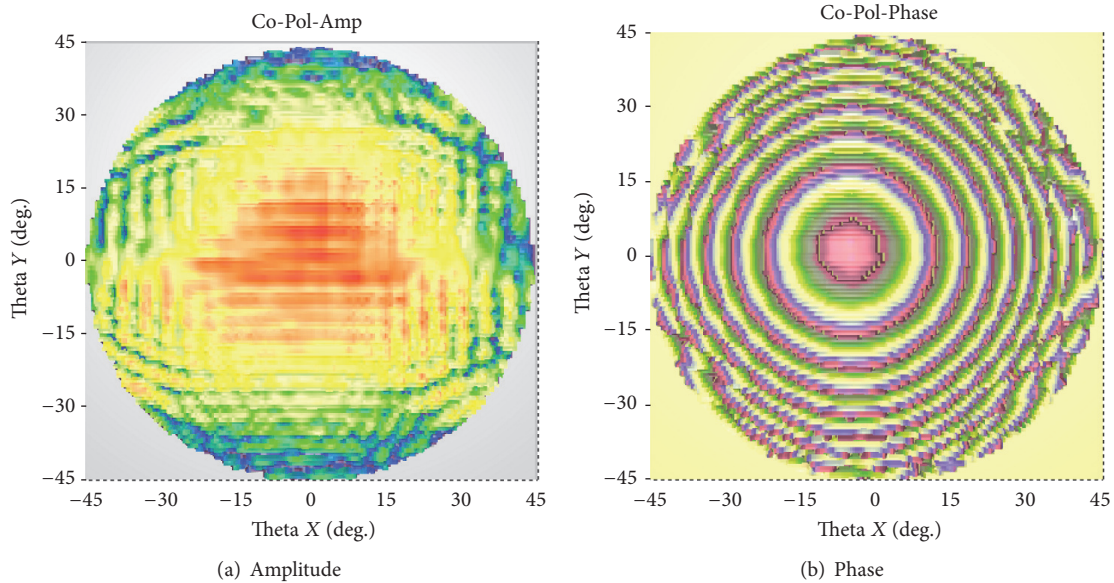


FIGURE 11: Measured (a) amplitude and (b) phase of the aperture field of the mmW microstrip antenna array excited at the center element.

near- and far-field test ranges. The measured amplitude and phase of the aperture field are plotted in Figures 11(a) and 11(b), respectively. Meanwhile, Figures 12(a) and 12(b) display photographs of the tested setup, and Figure 12(c) illustrates plots of the measured Co-Pol and Cross-Pol for the 2D radiation pattern cuts in the x - y and x - z planes at 37.75 GHz.

4. Conclusion

Our design prototype for an mmW microstrip antenna array operating at the Ka band frequency range for 5G communication system applications is presented using 64-element microstrip patches printed on an LTCC substrate with a thickness of 15 mil and a dielectric constant of 5.9.

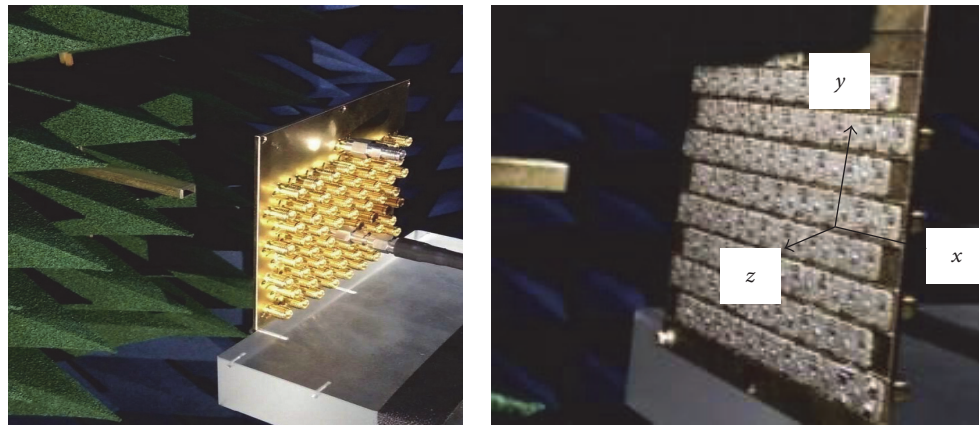
Our numerical and experimental study revealed acceptable agreement between the measured and simulated return losses and antenna power gain performance. This confirms that a microstrip patch antenna array with a high radiation gain performance in an mmW range is feasible for future 5G applications.

Competing Interests

The authors declare that they have no competing interests.

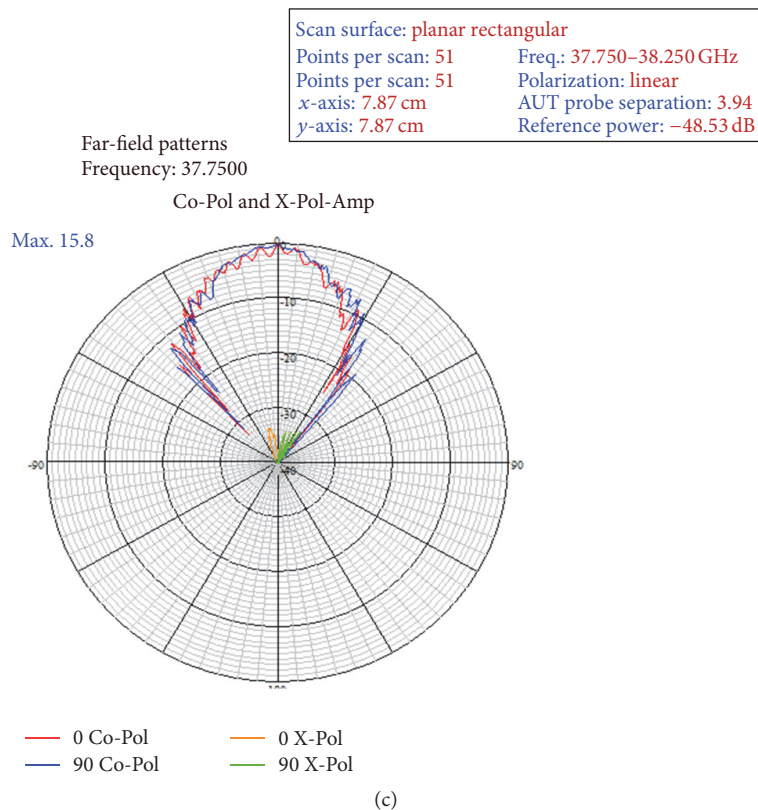
Acknowledgments

The authors thank the Chung-Shan Institute of Science and Technology (Taiwan) for financially supporting this research



(a)

(b)



(c)

FIGURE 12: (a) Amplitude and (b) phase photographs of the tested setup of the mmW microstrip antenna array. (c) Measured 2D Co-Pol and Cross-Pol radiation patterns.

(CSIST-A71-V1XX) and thank Kevin Peng for assisting in the manufacture and integration of the array.

References

- [1] J. Thompson, X. Ge, H.-C. Wu et al., "5G wireless communication systems: prospects and challenges [Guest Editorial]," *IEEE Communications Magazine*, vol. 52, no. 2, pp. 62–64, 2014.
- [2] M. S. Pandey, M. Kumar, A. Panwar, and I. Singh, "A survey: wireless mobile technology generations with 5G," *International Journal of Engineering Research and Technology*, vol. 2, no. 4, 2013.
- [3] Ericsson, "More than 50 billion connected devices," White Paper. [Online], http://www.akos-rs.si/files/Telekomunikacije/Digitalna_agenda/Internetni_protokol_Ipv6/More-than-50-billion-connected-devices.pdf.
- [4] Cisco, *Cisco Visual Network Index: Global Mobile Traffic Forecast Update*, 2013.
- [5] Ericsson, "Traffic and market data report," 2011.
- [6] UMTS Forum, *Mobile Traffic Forecasts: 2010–2020 Report*, UMTS Forum, Zürich, Switzerland, 2011.
- [7] P. E. Mogensen, K. Pajukoski, B. Raaf et al., "B4G local area: high level requirements and system design," in *Proceedings of the*

- IEEE Globecom Workshops (GC Wkshps '12)*, pp. 613–617, IEEE, Anaheim, Calif, USA, December 2012.
- [8] T. S. Rappaport, J. N. Murdock, and F. Gutierrez, “State of the art in 60-GHz integrated circuits and systems for wireless communications,” *Proceedings of the IEEE*, vol. 99, no. 8, pp. 1390–1436, 2011.
- [9] F. Khan and Z. Pi, “Millimeter wave mobile broadband (MMB): unleashing the 3–300 GHz spectrum,” in *Proceedings of the 34th IEEE Sarnoff Symposium*, March 2011.
- [10] Z. Pi and F. Khan, “An introduction to millimeter-wave mobile broadband systems,” *IEEE Communications Magazine*, vol. 49, no. 6, pp. 101–107, 2011.
- [11] P. Pietraski, D. Britz, A. Roy, R. Pragada, and G. Charlton, “Millimeter wave and terahertz communications: feasibility and challenges,” *ZTE Communications*, vol. 10, no. 4, pp. 3–12, 2012.
- [12] Y. P. Zhang and D. Liu, “Antenna-on-chip and antenna-in-package solutions to highly integrated millimeter-wave devices for wireless communications,” *IEEE Transactions on Antennas and Propagation*, vol. 57, no. 10, pp. 2830–2841, 2009.
- [13] S. Rangan, T. S. Rappaport, and E. Erkip, “Millimeter-wave cellular wireless networks: potentials and challenges,” *Proceedings of the IEEE*, vol. 102, no. 3, pp. 366–385, 2014.
- [14] B. Widrow, L. J. Griffiths, P. E. Mantey, and B. B. Goode, “Adaptive antenna systems,” *Proceedings of the IEEE*, vol. 55, no. 12, pp. 2143–2159, 1967.
- [15] W. F. Gabriel, “Adaptive array—an introduction,” *Proceeding of IEEE*, vol. 55, no. 12, pp. 2144–2159, 1967.
- [16] C.-N. Hu, “A novel method for calibrating deployed active antenna arrays,” *IEEE Transactions on Antennas and Propagation*, vol. 63, no. 4, pp. 1650–1657, 2015.
- [17] J. E. Hudson, *Adaptive Array Principles (IEEE Electromagnetic Waves Series)*, Institution of Engineering and Technology, Stevenage, UK, 1981.
- [18] J. G. Proakis, *Digital Communications*, McGraw-Hill, New York, NY, USA, 4th edition, 2001.
- [19] M. Wennström, *On MIMO systems and adaptive arrays for wireless communication [Ph.D. thesis]*, Uppsala University, Uppsala, Sweden, 2002.
- [20] G. Tsoulos, M. Beach, and J. McGeehan, “Space division multiple access (SDMA) field trials. Part 2: calibration and linearity issues,” *IEE Proceedings-Radar, Sonar and Navigation*, vol. 145, no. 1, pp. 79–84, 1998.
- [21] M. Morgan and S. Weinreb, “A millimeter-wave perpendicular coax-to-microstrip transition,” in *Proceedings of the IEEE MSS-S International Microwave Symposium Digest*, pp. 817–820, June 2002.
- [22] J. Chenkin, “DC to 40 GHz coaxial-to-microstrip transition for 100- μ m-thick GaAs substrates,” *IEEE Transactions on Microwave Theory and Techniques*, vol. 37, pp. 1147–1150, 1989.
- [23] D. K. Misra and K. M. Devendra, *Radio-Frequency and Microwave Communications Circuits-Analysis and Design*, Ch. 2.4 Antenna Systems, John Wiley & Son, Inc, Hoboken, NJ, USA, 2nd edition, 2004.

Research Article

Enhanced Next Generation Millimeter-Wave Multicarrier System with Generalized Frequency Division Multiplexing

Hidekazu Shimodaira,¹ Joongheon Kim,² and Ali S. Sadri³

¹*NTT DOCOMO, Inc., Tokyo, Japan*

²*School of Computer Science and Engineering, Chung-Ang University, Seoul, Republic of Korea*

³*mmWave Standards and Advanced Technology (mSAT) Team, Intel Corporation, San Diego, CA, USA*

Correspondence should be addressed to Joongheon Kim; joongheon@gmail.com

Received 25 July 2016; Revised 7 November 2016; Accepted 14 November 2016

Academic Editor: Imdad Khan

Copyright © 2016 Hidekazu Shimodaira et al. This is an open access article distributed under the Creative Commons Attribution License, which permits unrestricted use, distribution, and reproduction in any medium, provided the original work is properly cited.

Orthogonal Frequency Division Multiplexing (OFDM) is a popular multicarrier technique used to attain high spectral efficiencies. It also has other advantages such as multipath tolerance and ease of implementation. However, OFDM based systems suffer from high Peak-to-Average Power Ratio (PAPR) problem. Because of the nonlinearity of the power amplifiers, the high PAPR causes significant distortion in the transmitted signal for millimeter-wave (mmWave) systems. To alleviate the high PAPR problem, this paper utilizes Generalized Frequency Division Multiplexing (GFDM) which can achieve high spectral efficiency as well as low PAPR. In this paper, we show the performance of GFDM using the IEEE 802.11ad multicarrier frame structures. IEEE 802.11ad is considered one of the most successful industry standards utilizing unlicensed mmWave frequency band. In addition, this paper indicates the feasibility of using GFDM for the future standards such as IEEE 802.11ay. This paper studies the performance improvements in terms of PAPR reduction for GFDM. Based on the performance results, the optimal numbers of subcarriers and subsymbols are calculated for PAPR reduction while minimizing the Bit Error Rate (BER) performance degradation. Moreover, transmitter side ICI (Inter-carrier Interference) reduction is introduced to reduce the receiver load.

1. Introduction

The demands for wireless data communications have been increasing year by year. Recently, transmitting pictures or movies through a wireless channel is very popular and even 4K resolution ultra-high definition (UHD) video can be transmitted in real-time over the wireless channel. In order to support this kind of massive wireless data transmissions, ultra-wide channel bandwidths are essentially required. Among various candidates, millimeter-wave (mmWave) wireless communication technology is one of promising ultra-wideband wireless communication technologies in order to realize multi-gigabit-per-second (multi-Gbps) ultra-high speed wireless data communications. For instance, 60 GHz mmWave channels have a bandwidth of 2.16 GHz [1].

Among several mmWave wireless technologies, this paper mainly focuses on 60 GHz IEEE 802.11ad as it is the most successful standard in mmWave research societies [1, 2]. However, the proposed methodologies are applicable for other

mmWave standards including 28 GHz and 38 GHz mmWave frequency bands [3–6]. The IEEE 802.11ad (hereinafter referred to as 11ad) is one of the mmWave wireless communication systems which uses 60 GHz ISM (Industry-Science-Medical) band. In more detail, 57–66 GHz is allocated to the 60 GHz ISM band and 11ad separates this 9 GHz band into four channels of 2.16 GHz bandwidth each. 11ad supports two types of transmission schemes, Single Carrier (SC) and Orthogonal Frequency Division Multiplexing (OFDM) transmission, and theoretical maximum throughput reaches about 7 Gbps using the OFDM transmission scheme. OFDM efficiently utilizes system bandwidth based on (i) subcarrier orthogonality and (ii) intersymbol interference (ISI) mitigation due to the narrow band characteristics in each subcarrier. However, parallel transmission using large number of subcarriers increases Peak-to-Average Power Ratio (PAPR) [7–9]. In 60 GHz communication systems, the demand for power amplifier is more severe than that of microwave systems and hence high PAPR

is undesirable. In order to tackle this problem there are two major approaches: (i) applying PAPR reduction techniques for OFDM and (ii) introducing new waveforms.

The first approach, that is, the PAPR reduction techniques for OFDM, has been studied extensively in the literature. One such PAPR reduction technique is transmit signal clipping [10–12]. This technique sets a threshold value and just clips the high amplitudes. Since some transmit signals are distorted and undesired signals are radiated by clipping, the clipped signals are filtered before transmission. The other commonly used PAPR reduction technique is signal companding. This technique applies nonlinear compression to the transmit signals to suppress the signal peak values [13–15]. Partial Transmit Sequences (PTS) technique [16–18] divides subcarriers into segments and modulates each block. After modulation, phase rotation factor is applied to each partial sequence in time domain, and the subsegments are combined. Selected Mapping (SLM) technique makes several OFDM modulated signals where each OFDM modulation has its own different phase weight and chooses the best one from candidates [19–21].

The second approach, that is, new waveform design for the next generation wireless systems, has been currently investigated actively. From the view point of PAPR reduction, Filter Bank Multicarrier (FBMC) is one of the well-investigated waveforms [22]. FBMC applies pulse shaping filter to each subcarrier. The filter bank structure can be adapted to the clipping technique [23, 24]. However since clipping technique induces not only the out-of-band radiation but also the in-band distortion, the system becomes more complicated. Generalized Frequency Division Multiplexing (GFDM) [25, 26] is also one of the new waveform candidates and it can reduce PAPR efficiently utilizing more straightforward methods. GFDM can flexibly configure the symbol structure; that is, the number of subcarriers can be configured by introducing time domain slicing. Since GFDM can have the characteristics of both single carrier and multicarrier transmission, low PAPR and high spectral efficiency can be achieved simultaneously by applying appropriate configuration.

This paper focuses on GFDM and proposes GFDM frame design for 11ad to be fully in compliance with standards. The validity of the proposed frame structure is shown through intensive numerical simulations. Based on the PAPR and Bit Error Rate (BER) simulation results, the best GFDM configuration for 11ad system is determined. The computational complexity of GFDM is analyzed and a low complexity modulator/demodulator is proposed. Using the scheme proposed in this paper, the performance of current multicarrier mmWave standards can be improved in terms of the throughput for various mmWave systems such as backhaul in line-of-sight (LOS), fronthaul in LOS, and access networks in both LOS and non-LOS (NLOS).

The remaining sections are organized as follows. Section 2 explains OFDM and GFDM briefly and introduces the 11ad OFDM structure. Section 3 proposes a new GFDM frame structure for 11ad. Section 4 introduces a novel low complexity interference canceller for GFDM. PAPR and BER comparison is shown in Section 5. Section 6 analyzes the

computational complexity of modulation/demodulation architectures. Finally, conclusion and future work are provided in Section 7.

2. System Overview

In this section, we first discuss the OFDM and GFDM symbol structures and then describe the 11ad OFDM system architecture.

2.1. Overview of OFDM. OFDM is one of the well-known multicarrier transmission schemes [27–31]. It is widely employed by several wireless systems including Digital Terrestrial Television Broadcasting, LTE (Long Term Evolution), and IEEE 802.11a/g/n/ac/ad. Since OFDM transmits signals in parallel utilizing many subcarriers, each subcarrier bandwidth becomes narrow and thus the ISI is mitigated. Moreover, thanks to the FFT (Fast Fourier Transform) algorithm in OFDM structures, computational and implementation costs can be reduced.

The mathematical expression of an OFDM transmission symbol is as follows;

$$x[n] = \sum_{k=0}^{N-1} d_k \exp\left(j2\pi \frac{nk}{N}\right), \quad (1)$$

where $x[n]$ is the transmission symbol of n th time sample and k and N are the subcarrier index and the total number of subcarriers, respectively. d_k in (1) is the QAM (Quadrature Amplitude Modulation) modulated symbol transmitted on the k th subcarrier. Equation (1) describes parallel transmission of N modulated symbols (d_0, d_1, \dots, d_{N-1}) using N orthogonal subcarriers. Please note that (1) is equivalent to the definition of IDFT (Inverse Discrete Fourier Transform), and hence the transmitted data symbols in (1) can be rewritten as follows:

$$\mathbf{x} = \mathbf{F}^H \mathbf{d}$$

$$\mathbf{x} = [x[0] \ x[1] \ \dots \ x[N-1]]^T \in \mathbb{C}^N$$

$$\mathbf{F} = \begin{bmatrix} w_N^{0 \cdot 0} & w_N^{0 \cdot 1} & \dots & w_N^{0 \cdot (N-1)} \\ w_N^{1 \cdot 0} & w_N^{1 \cdot 1} & \dots & w_N^{1 \cdot (N-1)} \\ \vdots & \vdots & \ddots & \vdots \\ w_N^{(N-1) \cdot 0} & w_N^{(N-1) \cdot 1} & \dots & w_N^{(N-1) \cdot (N-1)} \end{bmatrix} \in \mathbb{C}^{N \times N} \quad (2)$$

$$\mathbf{d} = [d_0 \ d_1 \ \dots \ d_{N-1}]^T \in \mathbb{C}^N,$$

where $w_N = \exp(-j(2\pi/N))$ is a primitive N th root of unity. $(\cdot)^T$ and $(\cdot)^H$ represent transpose and conjugate transpose, respectively. Figure 1 shows how to map modulated symbols on the time-frequency resource grid in OFDM.

On the receiver side, received signals can be demodulated using DFT operation.

2.2. Overview of GFDM. As the name suggests, GFDM generalizes the multicarrier modulation schemes, SC and OFDM,

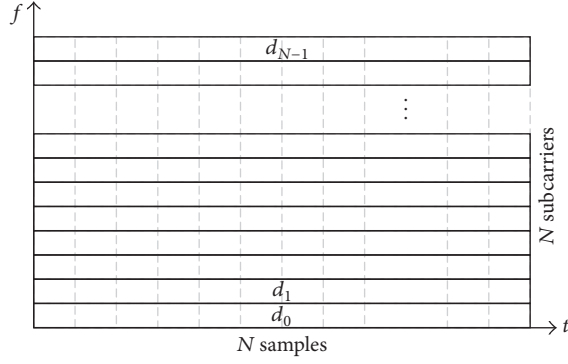


FIGURE 1: OFDM symbol mapping structure.

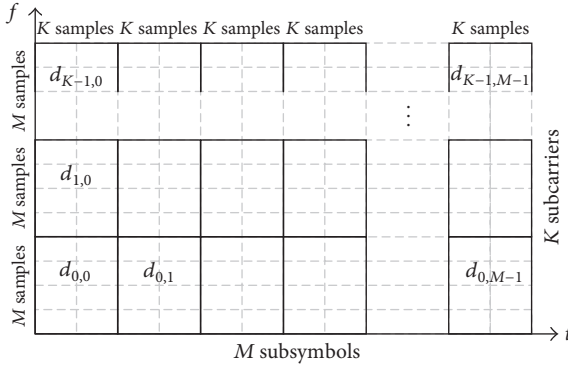


FIGURE 2: GFDM symbol mapping structure.

by controlling the system design parameters. In GFDM, a time-frequency resource grid is sliced in both frequency and time domains. QAM modulated symbols are mapped on each time-frequency resource block. Figure 2 shows the mapping illustration of GFDM where K and M stand for the number of subcarriers and number of subsymbols, respectively. Each resource block has $K \times M$ sample points. Therefore if $K \times M = N$ is satisfied, the amount of transmission data with GFDM will be equivalent to the amount of transmission data with OFDM during same symbol duration in same bandwidth. In order to localize each resource block, pulse shaping filter is applied.

The mathematical expression of GFDM transmission signal is as follows:

$$\begin{aligned}
 x[n] &= \sum_{k=0}^{K-1} \sum_{m=0}^{M-1} (d_{k,m} \delta[n - mK]) \\
 &\quad * g[n \bmod N] \exp\left(j2\pi \frac{nk}{K}\right) \\
 &= \sum_{k=0}^{K-1} \sum_{m=0}^{M-1} \underbrace{d_{k,m} \tilde{g}[n - mK]}_{x_k[n]} \exp\left(j2\pi \frac{nk}{K}\right) \\
 &= \sum_{k=0}^{K-1} x_k[n] \exp\left(j2\pi \frac{nk}{K}\right),
 \end{aligned} \tag{3}$$

where $(*)$ represents the convolution operation. In (3), $\tilde{g}[n - mK] \triangleq g[(n - mK) \bmod N]$ is the pulse shaping filter with mK time shifting. The modulo operation in (3) is equivalent to the tail biting process which makes filter convolution circular [32]. The GFDM modulation procedure is enumerated below and also shown in Figure 3.

- (1) Symbol sequence is divided into K parallel blocks, with each containing M QAM modulated symbols.
- (2) The QAM modulated symbol $d_{k,m}$ is upsampled by a factor N .
- (3) Pulse shaping filter is applied and the subsymbols are summed up in time domain.
- (4) Filtered symbols are upconverted to the corresponding subcarrier frequency.
- (5) All symbols are summed up.

In case of $M = 1$ and rectangular pulse shaping filter, (3) reduces to (1). In case of $K = 1$, (3) is equivalent to SC transmission. For this reason, this scheme is denoted as GFDM.

Equation (3) can be rewritten as a linear equation $\mathbf{x} = \mathbf{A}\mathbf{d}$. The matrix \mathbf{A} and vector \mathbf{d} are as follows:

$$\mathbf{A} = [\mathbf{G}_0 \circ \mathbf{W}_K \ \cdots \ \mathbf{G}_{M-1} \circ \mathbf{W}_K] \in \mathbb{C}^{N \times KM}$$

$$\mathbf{G}_m = \underbrace{[\tilde{\mathbf{g}}_m \ \tilde{\mathbf{g}}_m \ \cdots \ \tilde{\mathbf{g}}_m]}_K \in \mathbb{C}^{N \times K}$$

$$\tilde{\mathbf{g}}_m = [\tilde{g}[-mK] \ \tilde{g}[1 - mK] \ \cdots \ \tilde{g}[(N-1) - mK]]^T \in \mathbb{C}^N$$

$$\mathbf{W}_K = \begin{bmatrix} w_K^{0,0} & w_K^{0,1} & \cdots & w_K^{0,(K-1)} \\ w_K^{1,0} & w_K^{1,1} & \cdots & w_K^{1,(K-1)} \\ \vdots & \vdots & \ddots & \vdots \\ w_K^{(N-1),0} & w_K^{(N-1),1} & \cdots & w_K^{(N-1),(K-1)} \end{bmatrix} \in \mathbb{C}^{N \times K} \tag{4}$$

$$\mathbf{d} = [\mathbf{d}_0^T \ \cdots \ \mathbf{d}_m^T \ \cdots \ \mathbf{d}_{M-1}^T]^T \in \mathbb{C}^{KM}$$

$$\mathbf{d}_m = [d_{0,m} \ d_{1,m} \ \cdots \ d_{K-1,m}]^T \in \mathbb{C}^K,$$

where the operation (\circ) represents the Hadamard product.

This paper assumes that the receiver employs correlation detector. The correlation receiver is realized by multiplying \mathbf{A}^H to the received GFDM symbols. Since \mathbf{A} contains upconversion term for each subcarrier, downconversion can be performed through \mathbf{A}^H operation. Figure 4 shows normalized absolute value of $\mathbf{A}^H \mathbf{A}$. As shown in the figure, intercarrier interference (ICI) appears due to the nonorthogonality of subcarriers.

2.3. WiGig/IEEE 802.11ad OFDM Frame Structure. The 11ad OFDM frame is composed of five fields as defined in the standard, that is, Short Training Field (STF), Channel Estimation Field (CEF), Header, OFDM symbols, and optional training

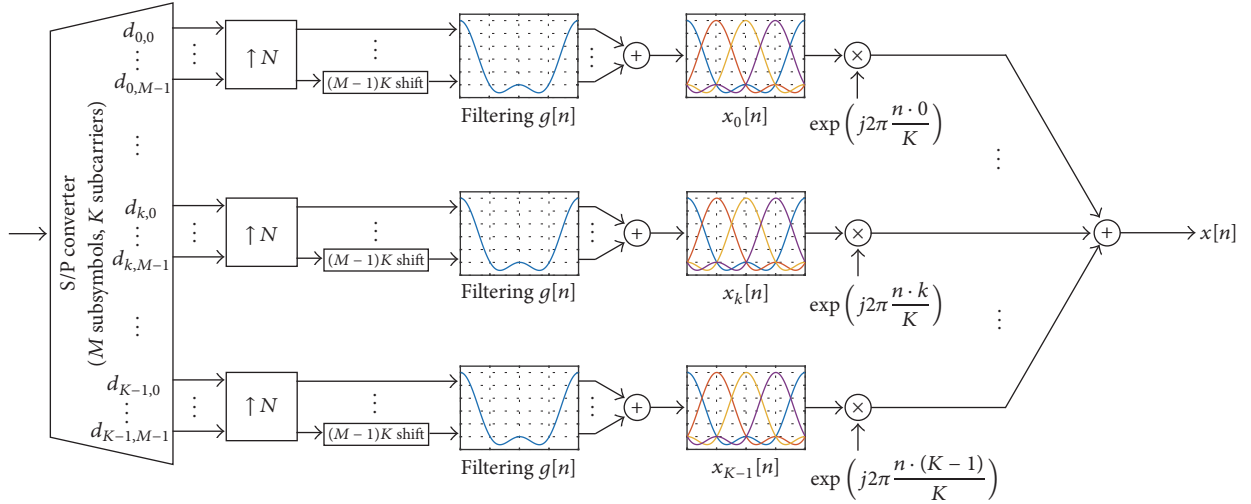
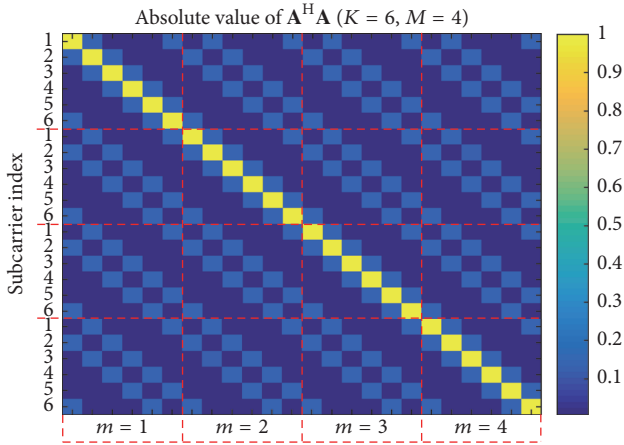


FIGURE 3: GFDM modulation block diagram.

FIGURE 4: ICI effect of the GFDM (Root Raised Cosine filter with roll-off factor 0.1. $K = 6, M = 4$).

fields. Since the header and optional training fields do not impact the performance, these fields are ignored in this paper.

The STF is used for the carrier frequency offset (CFO) estimation and autogain control (AGC) configuration. After CFO compensation and AGC, propagation channels are estimated using CEF. These two fields use Golay complementary sequence with $\pi/2$ -shift BPSK modulation [33]. Figure 5 shows the STF and CEF structures of control PHY (for control signal transmission), SC PHY, and OFDM PHY.

$G_{a_{128}}$ and $G_{b_{128}}$ in Figure 5 stand for 128-bit Golay complementary sequences. $G_{u_{512}}$ and $G_{v_{512}}$ are not the 512-bit Golay complementary sequences; however they are constructed with the concatenation of $G_{a_{128}}$ and $G_{b_{128}}$. The 11ad receiver can distinguish each frame due to the difference between STF and CEF. The last $-G_{a_{128}}$ in STF indicates the end of STF or the start point of CEF.

The OFDM symbol follows these preamble fields. The number of OFDM symbols within one packet varies according to the transmitted data and MCS (Modulation and

TABLE 1: WiGig/IEEE 802.11ad OFDM parameters.

Parameter	Value
Number of IDFT/DFT points	512
Number of data subcarriers	336
Number of pilot subcarriers	16 ($\pm 10, 30, 50, 70, 90, 110, 130, 150$)
Number of DC subcarriers	3 ($-1, 0, 1$)
Number of guard band subcarriers	157 ($-256 \sim -178, 178 \sim 255$)
Subcarrier frequency spacing	5.15625 MHz (2640 MHz/512)
OFDM sample rate	2640 MHz
OFDM symbol period	0.194 usec
Cyclic prefix duration	48.4 ns = 0.194 usec \times 25%

Coding Scheme). Table 1 shows important parameter configurations and corresponding values of 11ad OFDM. This paper proposes the GFDM frame structure for 11ad based on these parameters.

3. GFDM for IEEE 802.11ad Systems

GFDM has a potential to reduce the PAPR while achieving high throughput performance. However, in order to utilize GFDM in 11ad, transmission system has to be in compliance with the standard. This section proposes the designs of GFDM spectrum and pilot symbols.

3.1. GFDM DC Null and Guard Band Design. If there are no constraints, multicarrier transmission systems use entire bandwidth by separating several subcarriers. However if the “transmission system” is considered, DC subcarrier and guard band subcarrier have to be nullified to avoid DC offset

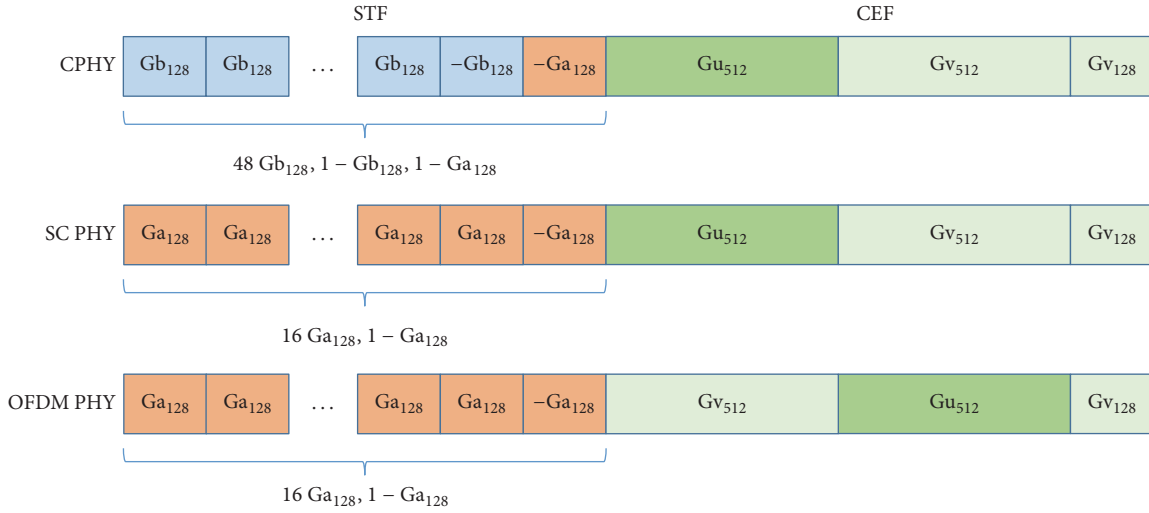


FIGURE 5: WiGig/IEEE 802.11ad preamble structure.

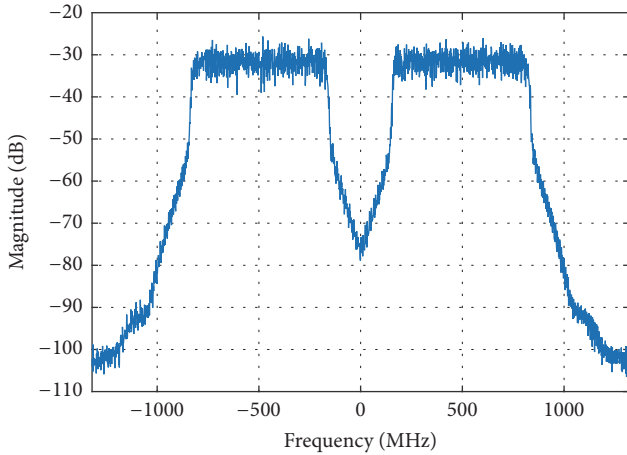


FIGURE 6: GFDM spectrum with DC nulling ($K = 8, M = 64$).

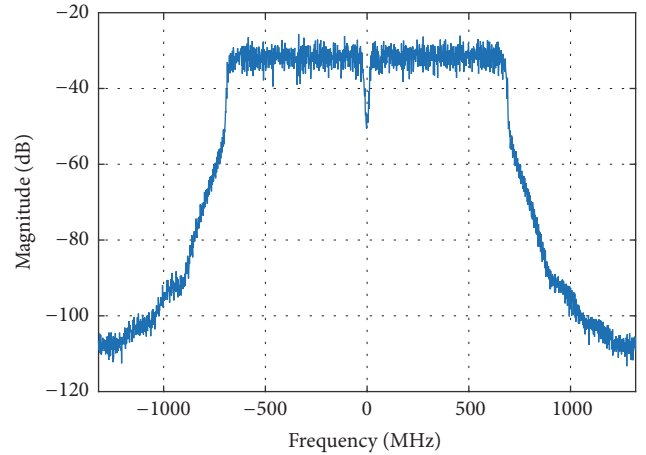


FIGURE 7: GFDM spectrum with DC nulling and frequency shift ($K = 8, M = 64$).

and interference for other channels or other systems. Based on Table 1, the GFDM transmission system for 11ad is designed.

Since GFDM uses small number of subcarriers to reduce PAPR, the subcarrier bandwidth becomes larger than that of OFDM. In the case of OFDM, DC nulling and guard band insertion are just setting zero to the corresponding subcarriers. In the GFDM case, this method results in the waste of frequency resources. Figure 6 shows the spectrum of conventional DC nulling and guard band insertion in the case of $K = 8$. Since the subcarrier spacing in this case is 330 MHz ($2640 \text{ MHz}/8$), DC null is very wide, and therefore fine-adjustment of guard bands is impossible. In addition, additional guard band insertion is required because this spectrum cannot satisfy 11ad requirement. Consequently, frequency resources are wasted.

This paper proposes subcarrier upshifting/downshifting methods to avoid the wasting of resources. As shown in Figure 3, GFDM modulation has upconversion blocks at

the last part. By introducing additional frequency shifting block, wide DC null can be shrunk. This can be done by downshifting the lower side ($k = 0, 1, \dots, K/2$) and upshifting the higher side ($k = K/2 + 1, K/2 + 2, \dots, K$). Figure 7 shows the result of this process. As evident from the figure, the DC null is reduced. Moreover, this frequency shifting enables the fine-adjustment of guard bands.

In the case of OFDM, the number of guard band subcarriers is 157; therefore GFDM system should employ the equivalent bandwidth corresponding to guard bands. The bandwidths corresponding to the guard band and the number of guard band subcarriers for GFDM are computed as follows:

$$B_g = 157 \times \frac{2640 \text{ MHz}}{512} \tag{5}$$

$$N_{g,\text{GFDM}} = \left\lceil \frac{B_g}{2640 \text{ MHz}/K} \right\rceil,$$

where B_g and $N_{g,\text{GFDM}}$ are the bandwidths corresponding to the guard band and the number of guard band subcarriers for GFDM, respectively. The operation $\lceil \cdot \rceil$ represents rounding function. The proposed 1lad GFDM system employs these values.

The mathematical expression of GFDM modulation matrix, \mathbf{A} , including the frequency shifting is given below:

$$\mathbf{A} = \left[\mathbf{G}_0 \circ \widetilde{\mathbf{W}}_K \quad \mathbf{G}_1 \circ \widetilde{\mathbf{W}}_K \quad \cdots \quad \mathbf{G}_{M-1} \circ \widetilde{\mathbf{W}}_K \right] \in \mathbb{C}^{N \times KM}$$

$$\widetilde{\mathbf{W}}_K = \begin{bmatrix} w_K^{0 \cdot 0} v_{\Delta f_0}^0 & \cdots & w_K^{0 \cdot (K-1)} v_{\Delta f_K}^0 \\ w_K^{1 \cdot 0} v_{\Delta f_0}^1 & \cdots & w_K^{1 \cdot (K-1)} v_{\Delta f_K}^1 \\ \vdots & \ddots & \vdots \\ w_K^{(N-1) \cdot 0} v_{\Delta f_0}^{N-1} & \cdots & w_K^{(N-1) \cdot (K-1)} v_{\Delta f_K}^{N-1} \end{bmatrix} \in \mathbb{C}^{N \times K} \quad (6)$$

$$v_{\Delta f_k} = \exp \left(\text{sgn} \left(k - \frac{N_{g,\text{GFDM}}}{2} \right) j 2\pi \Delta f \right),$$

where $\text{sgn}(\cdot)$ is sign function which returns the sign of the argument. Δf is the frequency shift.

3.2. GFDM Pilot Symbol Design. In 1lad OFDM PHY, pilot symbols are mapped onto the specific subcarriers over all time. The pilot symbols are used for the phase derotation at the receiver side. The pilot symbols have to be inserted since received signals cannot be demodulated under existence of the phase rotation. However, in the case of GFDM, if the pilot symbol is transmitted using specific subcarrier over all time, it results in the waste of resources due to the wide subcarrier bandwidth. This paper introduces a scattered pilot structure similar to the one in LTE packet. Figure 8 shows the time-frequency grid of one GFDM symbol. The yellow symbol represents the pilot symbol. The number of pilot symbols is 16 (same as OFDM) and they are mapped onto the lowest subcarrier and the highest subcarrier in a zigzag manner to avoid the ICI effect. Time domain spacing is $\lfloor M/16 \rfloor$ to be widely scattered. The phase tracking performance is shown in Figure 9. The upper plot corresponds to OFDM and the lower plot corresponds to GFDM. As expected, there is no significant difference between these two results.

4. Interchannel Interference Cancellation

As described in Section 2.2, the received GFDM symbol can be demodulated by multiplying \mathbf{A}^H . However as shown in Figure 4, the ICI effect is significant and it degrades the Bit Error Rate (BER) performance. The ICI reduction schemes for GFDM have been studied and the algorithm named Double Sided Serial Interference Cancellation (DSIC) [34] shows good performance results. However, this ICI reduction scheme is affected by channel equalization errors and noise effects. Moreover, the special blocks for ICI reduction are needed because ICI estimation is done per subcarrier. This complexity comes from the assumption that ICI should be mitigated at the receiver side. The ICI of GFDM is completely

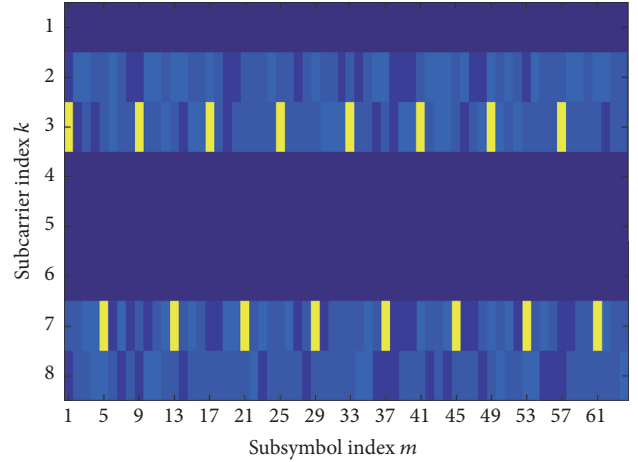


FIGURE 8: Pilot symbol insertion for GFDM symbol ($K = 8, M = 64$).

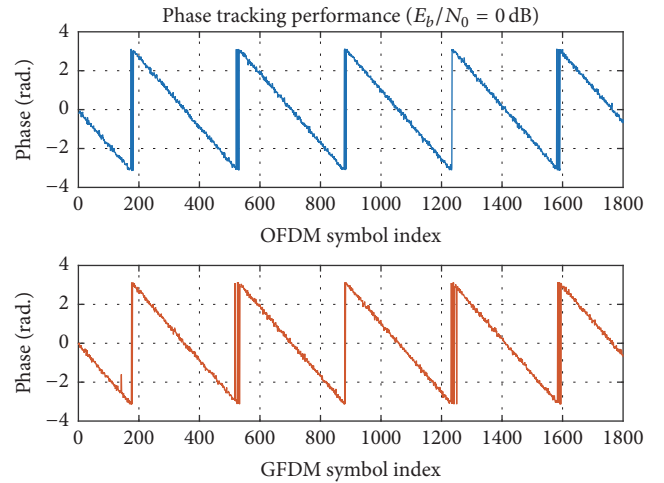


FIGURE 9: Phase tracking performance comparison.

different from the problem in OFDM. This ICI in GFDM is self-interference arose due to subcarrier nonorthogonality. Therefore, the transmitter should be able to estimate the ICI values before the wireless transmission without any noise effects. This paper introduces a transmitter side ICI reduction scheme for GFDM. The proposed ICI reduction block is illustrated as shown in Figure 10.

\mathbf{d} and $\bar{\mathbf{d}}$ are original QAM modulated symbol and ICI subtracted symbol, respectively. In addition, iterative calculation is desired in order to reduce ICI effects effectively because ICI subtraction leads to another ICI. This ICI reduction block is constructed with GFDM modulator, GFDM demodulator, and adder. According to the fact that the device which has GFDM should have both modulator and demodulator, this ICI reduction block does not require special additional block.

5. Simulation Study

5.1. Deriving M and K for Improved Performance. As presented in previous sections, 1lad GFDM system performance

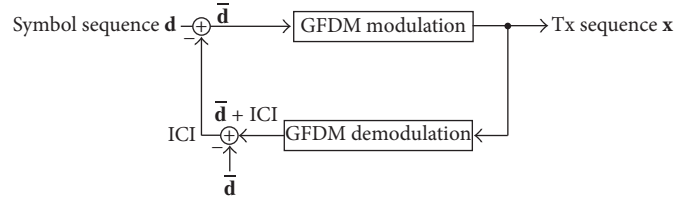


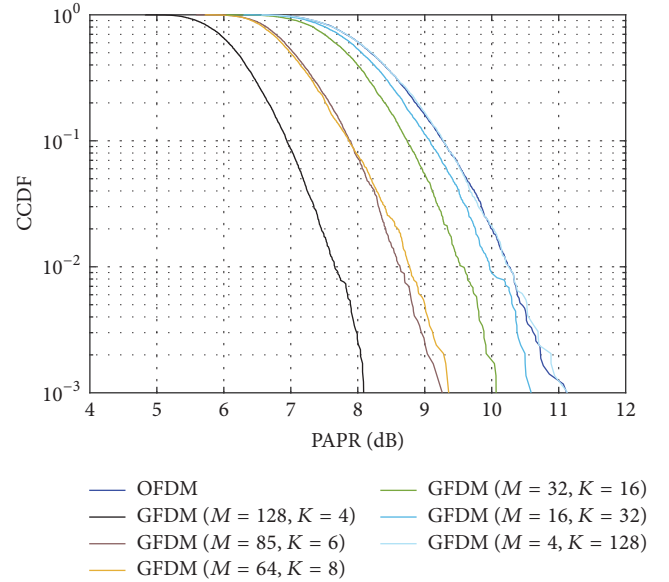
FIGURE 10: Transmitter side ICI reduction block diagram.

TABLE 2: IEEE 802.11ad GFDM parameters.

Parameter	Value
Number of subcarriers K	4, 6, 8, 16, 32, 128
Number of subsymbols M	$\lfloor 512/K \rfloor$
Number of pilot symbols	16
Number of DC subcarriers	1
Number of guard band subcarriers	$N_{g,GFDM}$
GFDM sample rate	2640 MHz
GFDM symbol period	$(K \times M)/2640$ usec
Cyclic prefix duration	$48.4 \text{ ns} + (512 - K \times M)/2640$ MHz
Channel model	11ad cubicle LOS/NLOS (far laptop) [35]
Carrier frequency offset	0–10 MHz (random generated)
Pulse shaping filter	Root Raised Cosine
Roll-off factor α	0.1, 0.2, 0.3, 0.4
Modulation and coding scheme	11ad MCS 16, 20, 24 [33]
Number of ICI canceler iterations	1–4

is evaluated in terms of PAPR and BER. The simulation parameters are provided in Table 2. The second term of the cyclic prefix is for the symbol length adjustment when $K \times M \neq 512$. For the simple derivation, GFDM with K subcarriers and M subsymbols is derived as (K, M) -GFDM hereafter.

5.1.1. PAPR Comparison. Figure 11 shows the complementary cumulative distribution function (CCDF) of PAPR. This simulation assumes QPSK transmission with the roll-off factor $\alpha = 0.1$. Although the PAPR value changes if other modulation schemes are employed, relativity is not changed. In the view point of PAPR, $(4, 128)$ -GFDM achieves the best performance due to the small number of subcarriers. However, in this case, the number of guard band subcarriers is 1; that is, $N_{g,GFDM} = 1$. Therefore, the effective number of subcarriers is only two. It means that one $(4, 128)$ -GFDM symbol can only transmit $2 \times 128 = 256$ symbols. To make matters worth, it contains pilot symbols. Consequently, $(4, 128)$ -GFDM can only transmit 240 data symbols with one GFDM symbol. Therefore $(4, 128)$ -GFDM degrades throughput performance. On the other hand, in $(6, 85)$ -GFDM and $(8, 64)$ -GFDM case, they still show good PAPR performance. From

FIGURE 11: PAPR comparison between OFDM and GFDM (QPSK, $\alpha = 0.1$).

the throughput point of view, 324 and 240 data symbols can be transmitted using $(6, 85)$ -GFDM and $(8, 64)$ -GFDM, respectively. Therefore $(6, 85)$ -GFDM can achieve the best PAPR performance while it maintains throughput performance. If there is no guard band insertion, it is obvious that the throughput performances are same between all configurations and PAPR performance can be improved by decreasing the number of subcarriers. Therefore only from the view point of PAPR, SC is the best solution. However, SC is strongly affected by the multipath effect. Based on these issues, this paper concludes that $(6, 85)$ -GFDM is the best in order to maintain high throughput as well as good PAPR performance. Hereafter, performance evaluation focuses the $(6, 85)$ -GFDM.

Figure 12 shows PAPR dependency on roll-off factor α . As shown in Figure 12, 16QAM and 64QAM show no significant difference, while QPSK shows remarkable performance improvement. If $\alpha = 0.4$ is considered, PAPR performance reaches the performance of $(4, 128)$ -GFDM.

5.1.2. BER Performance Comparison. Figure 13 compares the BER performance of OFDM and several GFDM configuration systems in LOS environment. As shown in Figure 13,

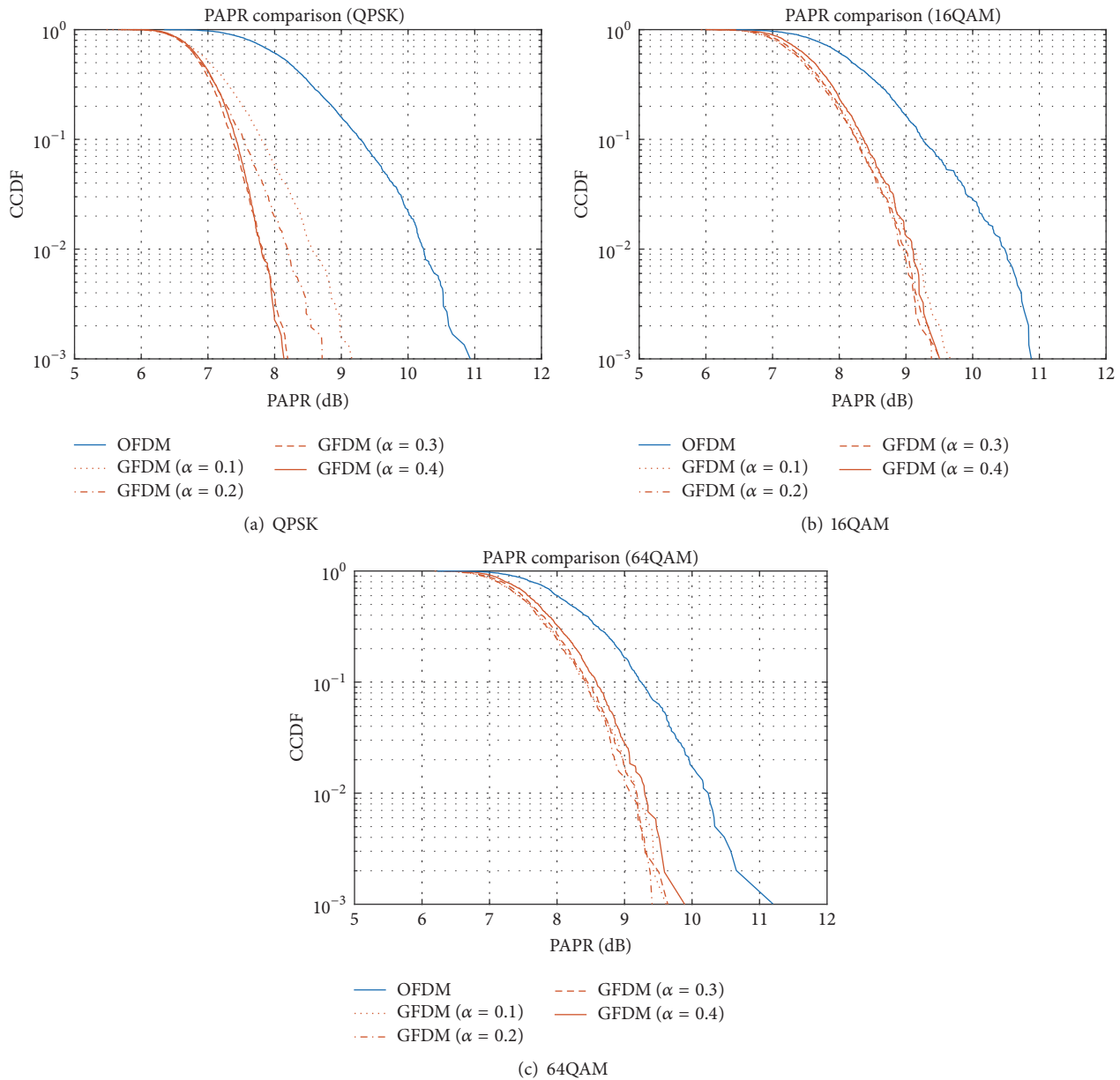


FIGURE 12: PAPR dependency on roll-off factor.

there is no significant difference in the BER values for different iterations. Two iterations are sufficient to achieve good BER performance. In addition, the OFDM and GFDM show similar BER performances in the best case. These performance results indicate that (6, 85)-GFDM can reduce PAPR up to 3 dB without compromising the system throughput.

Figure 14 shows the BER performance in NLOS environment. It can be seen that the GFDM is significantly better than the OFDM system. This is because of the channel equalization error effect becoming more dominant in NLOS conditions. This error causes frequency selectivity. Since OFDM uses narrow band subcarriers, this effect degrades BER performance. On the other hand, GFDM is relatively more robust

to this effect because of the wide bandwidths of the subcarriers.

6. Computational Complexity

Theoretically, GFDM modulation and demodulation can be realized by simply multiplying the modulation matrix \mathbf{A} as described in Section 2.2. However this simple approach requires high computational costs, that is, the large number of complex multiplications. In addition, constructing modulation matrix \mathbf{A} also requires high computational costs because it is constructed with the Hadamard product of complex

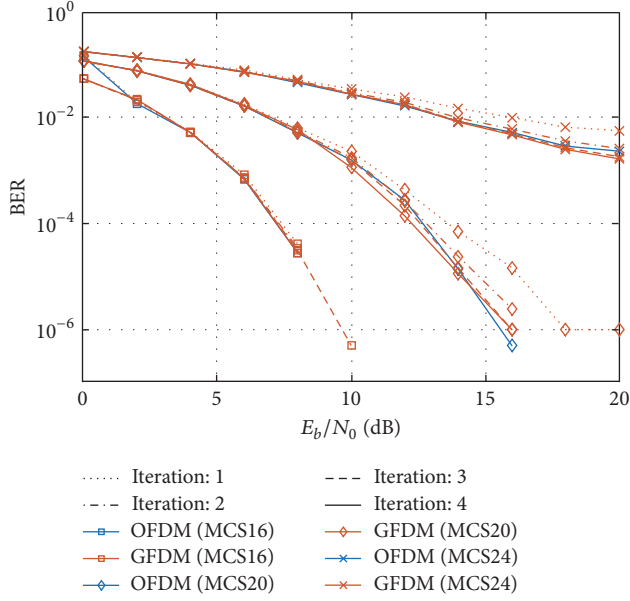


FIGURE 13: BER comparison between OFDM and GFDM (MCS 16, 20, and 24, $\alpha = 0.1$, LOS).

matrix. In order to reduce the number of complex multiplications, modulation and demodulation blocks should be reconfigured so that FFT can be used. Equation (3) can be rewritten as follows:

$$\begin{aligned}
 x[n] &= \sum_{k=0}^{K-1} \sum_{m=0}^{M-1} d_{k,m} \tilde{g}[n - mK] \exp\left(j2\pi \frac{nk}{K}\right) \\
 &= \sum_{m=0}^{M-1} \tilde{g}[n - mK] \underbrace{\sum_{k=0}^{K-1} d_{k,m} \exp\left(j2\pi \frac{nk}{K}\right)}_{\text{IDFT}} \\
 &= \sum_{m=0}^{M-1} \tilde{g}[n - mK] D_m[n \bmod K],
 \end{aligned} \quad (7)$$

where $D_m[n \bmod K]$ is IDFT of $d_{k,m}$. Since $n = 0, 1, \dots, KM - 1$, $D_m[n]$ becomes circular repetition sequence. Equation (7) shows that $x[n]$ can be computed using IDFT and summing up the filtered M sequences. The total number of the complex multiplications involved in GFDM modulator is $(K \log K (\text{IFFT}) + MK (\text{Filtering})) \times M = (\log K + M)MK$.

Similarly, GFDM demodulation can be described as follows:

$$\begin{aligned}
 \hat{d}_{k',m'} &= \sum_{n=0}^{KM-1} \tilde{g}[n - m'K] x[n] \exp\left(-j2\pi \frac{nk'}{K}\right) \\
 &= \sum_{l=0}^{M-1} \sum_{n=lK}^{(l+1)K-1} \tilde{g}[n - m'K] x[n] \exp\left(-j2\pi \frac{nk'}{K}\right) \\
 &= \sum_{l=0}^{M-1} \sum_{n'=0}^{K-1} \tilde{g}[n' + lK - m'K] x[n' + lK] \exp\left(-j2\pi \frac{k'n'}{K}\right)
 \end{aligned}$$

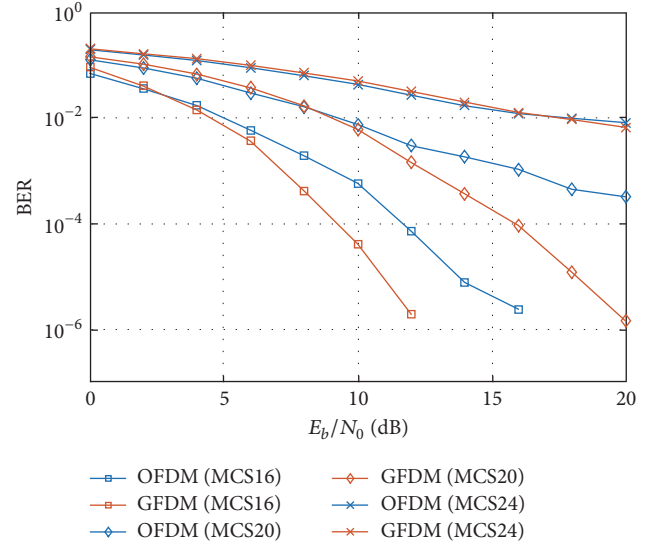


FIGURE 14: BER comparison between OFDM and GFDM (MCS 16, 20, and 24, $\alpha = 0.1$, NLOS).

$$\begin{aligned}
 &\cdot \frac{k'(n' + lK)}{K} \\
 &= \underbrace{\sum_{l=0}^{M-1} \tilde{g}[n' + lK - m'K] x[n' + lK]}_{\text{Correlation receiver}} \sum_{n'=0}^{K-1} \exp\left(-j2\pi \frac{k'n'}{K}\right) \\
 &\cdot \frac{k'n'}{K} = \underbrace{\sum_{n'=0}^{K-1} D_{m'}[n'] \exp\left(-j2\pi \frac{k'n'}{K}\right)}_{\text{DFT}}.
 \end{aligned} \quad (8)$$

Thus, the total number of the complex multiplications involved in GFDM demodulator is $(K \log K (\text{FFT}) + MK (\text{Filtering})) \times M = (\log K + M)MK$.

The modified modulation and demodulation blocks according to these equations are as illustrated in Figure 15.

Originally, the computational costs of matrix multiplication are M^2K^2 . Therefore, the computational cost of this modulation/demodulation blocks becomes $(\log K + M)MK / M^2K^2 = (\log K + M) / MK = 0.17$ for $(K, M) = (6, 85)$. Thus, the proposed structure can reduce about 83% of the computational cost. In [36], the proposed GFDM transceiver architecture cannot apply the FFT/IFFT blocks. In contrast, our proposed architecture can utilize the FFT/IFFT blocks and it can drastically reduce the computational cost.

7. Concluding Remarks and Future Work

This study has investigated the methodology for adapting GFDM to one of the most successful standards, that is, IEEE 802.11ad. It shows that the proposed GFDM frame structure is fully in compliance with the existing IEEE 802.11ad. Moreover, this study extends the ICI reduction technique to be suitable for IEEE 802.11ad wireless systems. The intensive

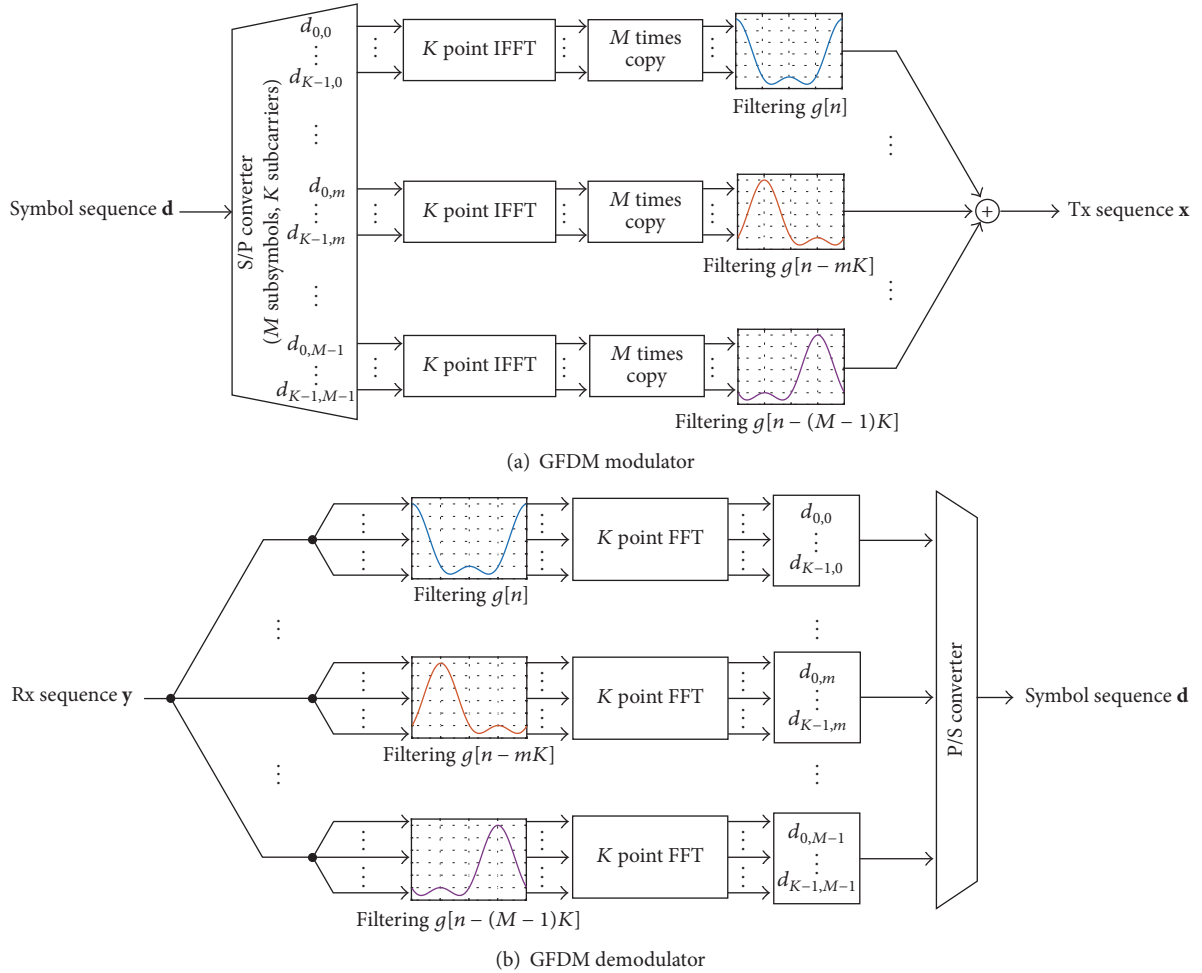


FIGURE 15: GFDM modulator and demodulator block.

performance evaluation results in this paper reveal that (6,85)-GFDM could achieve good PAPR and throughput performance simultaneously. The proposed efficient GFDM modulation/demodulation block can reduce computational costs by about 83%. The proposed method is applicable for other mmWave standards in IEEE 802.11ay and 5G mmWave cellular networks.

As a future research direction, it is possible to conduct more intensive performance evaluation considering the radio frequency (RF) impairments including power amplifier non-linearity, IQ imbalance, phase noises, and so forth.

Competing Interests

The authors declare that they have no competing interests.

Acknowledgments

This work was supported by Intel Next Generation and Standards (NGS) funds and also by National Research Foundation of Korea (NRF Korea) under Grant 2016R1C1B1015406.

References

- [1] J. Kim, Y. Tian, S. Mangold, and A. F. Molisch, "Joint scalable coding and routing for 60 GHz real-time live HD video streaming applications," *IEEE Transactions on Broadcasting*, vol. 59, no. 3, pp. 500–512, 2013.
- [2] J. Kim, Y. Tian, S. Mangold, and A. F. Molisch, "Quality-aware coding and relaying for 60 GHz real-time wireless video broadcasting," in *Proceedings of the IEEE International Conference on Communications (ICC '13)*, pp. 5148–5152, Budapest, Hungary, June 2013.
- [3] Y. Azar, G. N. Wong, K. Wang et al., "28 GHz propagation measurements for outdoor cellular communications using steerable beam antennas in New York city," in *Proceedings of the IEEE International Conference on Communications (ICC '13)*, pp. 5143–5147, Budapest, Hungary, June 2013.
- [4] H. Zhao, R. Mayzus, S. Sun et al., "28 GHz millimeter wave cellular communication measurements for reflection and penetration loss in and around buildings in New York city," in *Proceedings of the IEEE International Conference on Communications (ICC '13)*, pp. 5163–5167, Budapest, Hungary, June 2013.
- [5] T. S. Rappaport, F. Gutierrez, E. Ben-Dor, J. N. Murdock, Y. Qiao, and J. I. Tamir, "Broadband millimeter-wave propagation

- measurements and models using adaptive-beam antennas for outdoor urban cellular communications,” *IEEE Transactions on Antennas and Propagation*, vol. 61, no. 4, pp. 1850–1859, 2013.
- [6] W. Roh, J.-Y. Seol, J. Park et al., “Millimeter-wave beamforming as an enabling technology for 5G cellular communications: theoretical feasibility and prototype results,” *IEEE Communications Magazine*, vol. 52, no. 2, pp. 106–113, 2014.
- [7] S. Shepherd, J. Orriss, and S. Barton, “Asymptotic limits in peak envelope power reduction by redundant coding in orthogonal frequency-division multiplex modulation,” *IEEE Transactions on Communications*, vol. 46, no. 1, pp. 5–10, 1998.
- [8] T. Jiang, M. Guizani, H.-H. Chen, W. Xiang, and Y. Wu, “Derivation of PAPR distribution for OFDM wireless systems based on extreme value theory,” *IEEE Transactions on Wireless Communications*, vol. 7, no. 4, pp. 1298–1305, 2008.
- [9] T. Jiang and Y. Wu, “An overview: peak-to-average power ratio reduction techniques for OFDM signals,” *IEEE Transactions on Broadcasting*, vol. 54, no. 2, pp. 257–268, 2008.
- [10] J. Armstrong, “Peak-to-average power reduction for OFDM by repeated clipping and frequency domain filtering,” *Electronics Letters*, vol. 38, no. 5, pp. 246–247, 2002.
- [11] H. Ochiai and H. Imai, “On clipping for peak power reduction of OFDM signals,” in *Proceedings of the IEEE Global Telecommunications Conference (GLOBECOM '00)*, San Francisco, Calif, USA, December 2000.
- [12] Y.-C. Wang and Z.-Q. Luo, “Optimized iterative clipping and filtering for PAPR reduction of OFDM signals,” *IEEE Transactions on Communications*, vol. 59, no. 1, pp. 33–37, 2011.
- [13] X. Wang, T. T. Tjhung, and C. S. Ng, “Reduction of peak-to-average power ratio of OFDM system using a companding technique,” *IEEE Transactions on Broadcasting*, vol. 45, no. 3, pp. 303–307, 1999.
- [14] X. Huang, J. Lu, J. Zheng, K. B. Letaief, and J. Gu, “Companding transform for reduction in peak-to-average power ratio of OFDM signals,” *IEEE Transactions on Wireless Communications*, vol. 3, no. 6, pp. 2030–2039, 2004.
- [15] T. Jiang, Y. Yang, and Y.-H. Song, “Exponential companding technique for PAPR reduction in OFDM systems,” *IEEE Transactions on Broadcasting*, vol. 51, no. 2, pp. 244–248, 2005.
- [16] S. H. Müller and J. B. Huber, “OFDM with reduced peak-to-average power ratio by optimum combination of partial transmit sequences,” *Electronics Letters*, vol. 33, no. 5, pp. 368–369, 1997.
- [17] S.-J. Ku, C.-L. Wang, and C.-H. Chen, “A reduced-complexity PTS-based PAPR reduction scheme for OFDM systems,” *IEEE Transactions on Wireless Communications*, vol. 9, no. 8, pp. 2455–2460, 2010.
- [18] L. Yang, R. S. Chen, Y. M. Siu, and K. K. Soo, “PAPR reduction of an OFDM signal by use of PTS with low computational complexity,” *IEEE Transactions on Broadcasting*, vol. 52, no. 1, pp. 83–86, 2006.
- [19] R. W. Bäuml, R. F. H. Fischer, and J. B. Huber, “Reducing the peak-to-average power ratio of multicarrier modulation by selected mapping,” *Electronics Letters*, vol. 32, no. 22, pp. 2056–2057, 1996.
- [20] S. H. Han and J. H. Lee, “Modified selected mapping technique for PAPR reduction of coded OFDM signal,” *IEEE Transactions on Broadcasting*, vol. 50, no. 3, pp. 335–341, 2004.
- [21] C.-P. Li, S.-H. Wang, and C.-L. Wang, “Novel low-complexity SLM schemes for PAPR reduction in OFDM systems,” *IEEE Transactions on Signal Processing*, vol. 58, no. 5, pp. 2916–2921, 2010.
- [22] B. Farhang-Boroujeny, “OFDM versus filter bank multicarrier,” *IEEE Signal Processing Magazine*, vol. 28, no. 3, pp. 92–112, 2011.
- [23] Z. Kollár and P. Horváth, “PAPR reduction of FBMC by clipping and its iterative compensation,” *Journal of Computer Networks and Communications*, vol. 2012, Article ID 382736, 11 pages, 2012.
- [24] N. Van Der Neut, B. T. Maharaj, F. H. De Lange, G. Gonzalez, F. Gregorio, and J. Cousseau, “PAPR reduction in FBMC systems using a smart gradient-project active constellation extension method,” in *Proceedings of the 21st International Conference on Telecommunications (ICT '14)*, pp. 134–139, Lisbon, Portugal, May 2014.
- [25] G. Fettweis, M. Krondorf, and S. Bittner, “GFDM—generalized frequency division multiplexing,” in *Proceedings of the IEEE Vehicular Technology Conference (VTC '09)*, Barcelona, Spain, April 2009.
- [26] N. Michailow, M. Matthe, I. S. Gaspar et al., “Generalized frequency division multiplexing for 5th generation cellular networks,” *IEEE Transactions on Communications*, vol. 62, no. 9, pp. 3045–3061, 2014.
- [27] A. Y. Panah, R. G. Vaughan, and R. W. Heath Jr., “Optimizing pilot locations using feedback in OFDM systems,” *IEEE Transactions on Vehicular Technology*, vol. 58, no. 6, pp. 2803–2814, 2009.
- [28] E. Bedeer, O. A. Dobre, M. H. Ahmed, and K. E. Baddour, “Rate-interference Tradeoff in OFDM-based cognitive radio systems,” *IEEE Transactions on Vehicular Technology*, vol. 64, no. 9, pp. 4292–4298, 2015.
- [29] S. Bokharaiee, H. H. Nguyen, and E. Shwedyk, “Blind spectrum sensing for OFDM-based cognitive radio systems,” *IEEE Transactions on Vehicular Technology*, vol. 60, no. 3, pp. 858–871, 2011.
- [30] J. Ylioinas and M. Juntti, “Iterative joint detection, decoding, and channel estimation in turbo-coded MIMO-OFDM,” *IEEE Transactions on Vehicular Technology*, vol. 58, no. 4, pp. 1784–1796, 2009.
- [31] C. Shin, R. W. Heath Jr., and E. J. Powers, “Blind channel estimation for MIMO-OFDM systems,” *IEEE Transactions on Vehicular Technology*, vol. 56, no. 2, pp. 670–685, 2007.
- [32] H. H. Ma and J. K. Wolf, “On tail biting convolutional codes,” *IEEE Transactions on Communications*, vol. 34, no. 2, pp. 104–111, 1986.
- [33] IEEE P802.11 TGad, “PHY/MAC Complete Proposal Specification,” May 2010.
- [34] R. Datta, N. Michailow, M. Lentmaier, and G. Fettweis, “GFDM interference cancellation for flexible cognitive radio phy design,” in *Proceedings of the 76th IEEE Vehicular Technology Conference (VTC '12)*, Quebec, Canada, September 2012.
- [35] IEEE P802.11 TGad, “Channel Models for 60 GHz WLAN Systems,” May 2010.
- [36] N. Michailow, I. Gaspar, S. Krone, M. Lentmaier, and G. Fettweis, “Generalized frequency division multiplexing: analysis of an alternative multi-carrier technique for next generation cellular systems,” in *Proceedings of the 9th International Symposium on Wireless Communication Systems (ISWCS '12)*, pp. 171–175, August 2012.

Research Article

Pilot Contamination Mitigation via a Novel Time-Shift Pilot Scheme in Large-Scale Multicell Multiuser MIMO Systems

Zhangkai Luo,¹ Huali Wang,¹ and Wanghan Lv²

¹Department of Electrical and Computer Engineering, PLA University of Science and Technology, Nanjing 210007, China

²School of Electronic and Optical Engineering, Nanjing University of Science and Technology, Nanjing 210094, China

Correspondence should be addressed to Huali Wang; huali.wang@ieee.org

Received 7 July 2016; Accepted 19 September 2016

Academic Editor: Masood Ur-Rehman

Copyright © 2016 Zhangkai Luo et al. This is an open access article distributed under the Creative Commons Attribution License, which permits unrestricted use, distribution, and reproduction in any medium, provided the original work is properly cited.

We propose a novel time-shift pilot scheme to mitigate the pilot contamination in large-scale multicell multiuser MIMO (LS-MIMO) systems. In the proposed scheme, the length of the uplink training pilot sequence is equal to the cell number; that is to say, the same pilot sequence is used within a cell, while for different cells, pilot sequences are mutually orthogonal. Moreover, users within a cell transmit the same pilot sequence in a time-shift manner during the channel estimation stage and in this way all user terminals' channel state information can be estimated without contamination. The asymptotic channel orthogonality is studied in the LS-MIMO system, with which the mutual interference among cells caused by data and pilot sequences can be cancelled with the successive interference cancellation (SIC) method. We explore the superiority of the proposed scheme in channel coefficient estimation, uplink data detection, and downlink data transmission steps. Theoretical analysis and simulation results demonstrate that the proposed time-shift pilot design can alleviate the pilot contamination problem and improve the performance of the considered system significantly compared with the popular orthogonal pilots.

1. Introduction

Large-scale multicell multiuser MIMO (LS-MIMO) system is a novel and a promising network architecture, which provides breakthrough data rate by using a large excess of service-antennas over user terminals (UTs). Indeed, adding more antennas is always helpful for increasing throughput, reducing radiated power, offering uniformly great service everywhere in the cell, and simplifying signal processing [1–5].

For the LS-MIMO system, channel state information (CSI) estimation is a challenging issue for achieving multi-antenna gain. Generally, uplink training is often used to obtain CSI in time-division duplex (TDD) systems due to channel reciprocity. However, the required resource for orthogonal pilot sequences increases dramatically as the user number grows large. Besides, as the number of base station (BS) antennas tends to infinite, additive Gaussian noise and uncorrelated interferences vanish, and the only remaining is the correlated intercell interferences caused by users having the same pilot sequences in other cells [5]. Under the limitation of finite pilot sequence length, it is inevitable to

reuse the same set of orthogonal pilot sequences in adjacent cells, which causes the pilot contamination and brings a quick saturation to the system's performance. Thus, pilot contamination is a bottleneck which limits the performance advantages LS-MIMO can offer [6, 7].

Recent studies make an effort to address this problem [8–12]. Although they tried to alleviate the pilot contamination between multiple cells, they still used orthogonal pilot sequences in a signal cell which means a large pilot resource consumption especially when coherence interval is short and the user number is large in LS-MIMO systems [13].

Inspired by the idea in [13], in this paper, we propose a novel time-shift pilot scheme to mitigate the pilot contamination while considering the pilot resource consumption in the LS-MIMO system. As we know, in [13], the pilot sequence is transmitted in a time-shift manner to save more resource. Here, we extend this technology to the LS-MIMO system to deal with the pilot contamination problem. The main aspect of this extension is the proposal and analysis of the performance of the pilot scheme that alleviates the pilot contamination. In the proposed pilot scheme, the number of

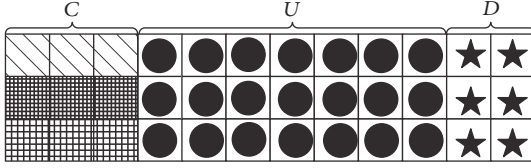


FIGURE 1: Conventional pilot scheme.

mutually orthogonal pilot sequences is equal to the number of cells and users within a cell transmit the same pilot sequence in a time-shift manner. In this way, all BSs can estimate the channel coefficients at the same time. Furthermore, the interference caused by data and pilot sequences can be cancelled by exploiting the asymptotic channel orthogonality combined with the SIC method in LS-MIMO systems [13]. We explore the superiority of the proposed scheme in channel coefficient estimation, uplink data detection, and downlink data transmission. Simulation results demonstrate that the proposed pilot scheme can alleviate the pilot contamination and achieve a high data rate. Moreover, the achievable rate grows with the BS antenna number with the proposed pilot scheme, while the achievable rate saturates rapidly with the conventional scheme.

This paper is organized as follows. In Section 2, we describe the system model and the conventional pilot sequence scheme. Then in Section 3, we study the problem of the proposed pilot scheme including channel coefficient estimation and data detection in uplink and downlink data transmission stage. In Section 4, we analyze the performance of the proposed method in terms of the achievable rate. In Section 5, we present numerical simulation results and show that the proposed pilot scheme can solve the pilot contamination and achieve a much better performance than the conventional pilot scheme.

2. System Model

We consider a cellular system composed of L cells, each consisting of K served signal-antenna users and one BS with M antennas. Let p_p , p_u , and p_d be the pilot sequence SNR, the uplink data SNR, and the downlink data SNR, respectively. Denote the channel coefficient from the k th user in the l th cell to the i th cell as $\mathbf{g}_{lki} = \sqrt{\beta_{lki}}\mathbf{h}_{lki}$, $i = 1, 2, \dots, L$, $k = 1, 2, \dots, K$, where the small-scale fading vector $\mathbf{h}_{lki} \sim \mathcal{CN}(0, \mathbf{I}_M)$ is statistically independent across users and β_{lki} models the large-scale fading, which is assumed to be constant and known a priori.

We assume a block fading model, where the small-scale fading vector remains constant during a coherence block of T symbols and is independent in different coherence blocks. In TDD systems, the channel coefficients are the same for both uplink and downlink data transmission in a coherence interval.

The conventional transmission system with orthogonal pilot sequences is shown in Figure 1. We give a coherence block for analysis, as the remaining coherence blocks can be analyzed in the same way. Each coherence interval is assumed

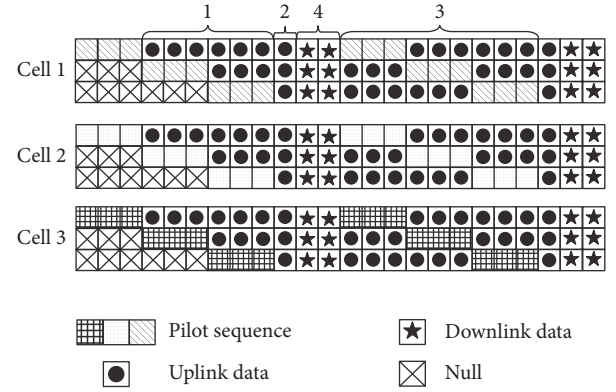


FIGURE 2: Proposed pilot scheme.

to be organized in three phases: U symbol periods for uplink data transmission, D symbol periods for downlink data transmission, and C symbol periods for uplink pilot sequences transmission. Therefore, the length of one coherence interval is $T = D + C + U$.

In conventional transmission system, orthogonal pilot sequences are assigned to each user to prevent pilot contamination within one cell, while they cannot prevent pilot contamination between cells. On the other hand, the length of pilot sequence is C ($C > K$), which is too large when K is large in LS-MIMO system. In such case, a lot of resource is consumed by transmitting pilot sequences.

Now, we give some notational definitions. x represents the index of the coherence interval.

$\mathbf{y}_i^m[x] \in \mathbb{C}^{M \times L}$ denotes the data received by the i th BS when the m th UTs of all cells transmit pilot sequences.

$\mathbf{z}_i^m[x] \in \mathbb{C}^{M \times L}$ denotes the additive noise received by the i th BS when the m th UTs of all cells transmit pilot sequences.

$\phi_l \in 1 \times L$ denotes the pilot sequence used in the l th cell.

$\mathbf{q}_{lki}^m[x] \in \mathbb{C}^{1 \times L}$ denotes the data transmitted by the t th user in the l th cell to the i th cell when the m th UTs of all cells transmit pilot sequences.

$\mathbf{q}_{lki}[x] \in \mathbb{C}^{1 \times L}$ denotes the data transmitted by the t th user in the l th cell to the i th cell when all channel coefficients have been estimated.

$\mathbf{g}_{lki}[x]$ denotes the channel coefficient between the k th user in the l th cell and the BS of the i th cell.

$\mathbf{s}_i^t[x] \in \mathbb{C}^{1 \times L}$ denotes the data transmitted by the l th BS to the t th user in the same cell.

$\sigma_{lki,x}^2$ denotes the variance of the channel coefficient between the k th user in the l th cell and the BS of the i th cell.

3. Time-Shift Orthogonal Pilot Scheme

To alleviate the problem of pilot contamination and the waste of resources, a novel time-shift orthogonal pilot scheme is proposed in this section, which reduces the length of pilot sequence for each UT and guarantees the system performance due to the merit of asymptotic channel orthogonality when the number of BS antennas is large. The proposed scheme is shown in Figure 2, obviously, the length of pilot sequence is equal to the cell number and for UTs in one

cell, the same pilot sequence is transmitted in a time-shift manner. We assume that all cells transmit all kinds of data synchronously.

In the first coherence interval, the first UTs of each cell transmit the pilot sequence while other UTs mute so that each cell can estimate their first UTs' channel coefficients \mathbf{g}_{iki} , $i = 1, 2, \dots, L$, $k = 1, 2, \dots, K$, without contamination. At the same time, cross channel coefficients \mathbf{g}_{lki} , $i, l = 1, 2, \dots, L$, $i \neq l$, $k = 1, 2, \dots, K$, can also be estimated, which can be used later for interference cancellation. When the second UTs of each cell transmit their pilot sequences, the first UTs transmit uplink data and other UTs still mute. In short, when the k th UTs of each cell transmit pilot sequences, the UTs whose index is less than k transmit the uplink data. Besides, the interference from other users can be cancelled by using SIC method with the estimated channel coefficients, which will be described later.

Then the estimated channel coefficients within one cell or between cells are used in the following uplink data reception, downlink data transmission, and interference cancellation steps. After the first coherence interval, UTs in all cells transmit uplink data except the ones that transmit pilot sequence to update their channel coefficients during the CSI estimation stage.

It is clear that, for all UTs, the length of the pilot sequence depends on the cell number L , and pilot sequences in different cells are mutually orthogonal to guarantee there is no pilot contamination among cells. Within a cell, UTs transmit the same pilot sequence in a time-shift manner so that we can conduct the channel coefficient estimation one by one without contamination.

3.1. Uplink Data Transmission in the First Interval. When the first UTs in all cells transmit pilot sequences in the first coherence interval, the $M \times L$ vector received by the i th $i = 1, 2, \dots, L$, BS is

$$\mathbf{y}_i^1 [1] = \sqrt{P_p} \sum_{l=1}^L \mathbf{g}_{l1i} [1] \phi_l + \mathbf{z}_i^1, \quad (1)$$

where $\mathbf{z}_i \in M \times L$ is the additive noise and the entries of \mathbf{z}_i are i.i.d. $\mathcal{CN}(0, 1)$ random variables and that all gains are scaled accordingly. The i th BS estimates the channel coefficients by using Minimum Mean Squared Error (MMSE) as

$$\hat{\mathbf{g}}_{l1i} [1] = \frac{\sqrt{P_p} \beta_{l1i}}{1 + \sum_{l=1}^L P_p \beta_{l1i}} \mathbf{y}_i^1 [1] \phi_l^H, \quad (2)$$

where $i, l = 1, 2, \dots, L$. According to MMSE estimation, $g_{l1i} [1] = \hat{g}_{l1i} [1] + \tilde{g}_{l1i} [1]$, $\hat{\mathbf{g}}_{l1i} [1] \sim \mathcal{CN}(0, \sigma_{l1i}^2 \mathbf{I}_M)$, and $\tilde{\mathbf{g}}_{l1i} \sim \mathcal{CN}(0, \varepsilon_{l1i}^2 \mathbf{I}_M)$ are the estimation errors which are independent of $\hat{g}_{l1i} [1]$, where $\varepsilon_{l1i}^2 = \beta_{l1i} - \sigma_{l1i}^2$ and $\sigma_{l1i}^2 = P_p \beta_{l1i}^2 / (1 + \sum_{l=1}^L P_p \beta_{l1i})$. Once each BS obtains the first UTs' channel coefficients to its cell, the first UTs transmit the uplink data, while the next UTs transmit pilot sequences.

We describe the data received at the i th BS when the m th UTs ($m > 1$) transmit pilot sequences as

$$\mathbf{y}_i^m [1] = \sqrt{P_p} \sum_{l=1}^L \mathbf{g}_{lmi} [1] \phi_l + \sqrt{P_u} \sum_{l=1}^L \sum_{t=1}^{m-1} \mathbf{g}_{lti} [1] \mathbf{q}_{lti}^m [1] + \mathbf{z}_i^m [1]. \quad (3)$$

Then the estimated channel coefficients are applied to the detection of the first UTs' uplink data as

$$\hat{\mathbf{q}}_{l1i}^m [1] = \frac{\hat{\mathbf{g}}_{l1i}^H [1]}{\sqrt{P_u} \|\hat{\mathbf{g}}_{l1i} [1]\|^2} \mathbf{y}_i^m \quad (4a)$$

$$= \frac{\hat{\mathbf{g}}_{l1i}^H [1]}{\|\hat{\mathbf{g}}_{l1i} [1]\|^2} \hat{\mathbf{g}}_{l1i} \mathbf{q}_{l1i}^m [1] + \frac{\hat{\mathbf{g}}_{l1i}^H [1]}{\|\hat{\mathbf{g}}_{l1i} [1]\|^2} \tilde{\mathbf{g}}_{l1i} \mathbf{q}_{l1i}^m [1] + \frac{\sqrt{P_p} \sum_{l=1}^L \hat{\mathbf{g}}_{l1i}^H [1] \mathbf{g}_{lmi} [1]}{\sqrt{P_u} \sum_{l=1}^L \|\hat{\mathbf{g}}_{l1i} [1]\|^2} \phi_l \quad (4b)$$

$$+ \sum_{l=1}^L \sum_{t=2}^{m-1} \frac{\hat{\mathbf{g}}_{l1i}^H [1] \mathbf{g}_{lti} [1]}{\|\hat{\mathbf{g}}_{l1i} [1]\|^2} \mathbf{q}_{lti}^m [1] + \frac{\hat{\mathbf{g}}_{l1i}^H [1] \mathbf{z}_i^m}{\sqrt{P_u} \|\hat{\mathbf{g}}_{l1i} [1]\|^2} = \mathbf{q}_{l1i}^m [1], \quad (4c)$$

where $\|\cdot\|$ denotes the 2-norm.

According to the properties of MMSE estimation, the estimated channel coefficient $\hat{\mathbf{g}}_{l1i} [1]$ is independent of $\tilde{\mathbf{g}}_{l1i} [1]$, $\mathbf{g}_{l1i} [1]$, and \mathbf{z}_i^m . We divide both the numerators and the denominators in (4b) by M and we get (4c) by applying Lemma 1 which describes the limit results of random vectors [14].

Lemma 1. Let \mathbf{p} and \mathbf{q} be two mutually independent vectors whose elements are i.i.d. zero-mean random variables with $E\{|p_i|^2\} = \sigma_p^2$ and $E\{|q_i|^2\} = \sigma_q^2$ and then $\lim_{M \rightarrow \infty} (\mathbf{p}^H \mathbf{p} / M) \xrightarrow{a.s.} \sigma_p^2$ and $\lim_{n \rightarrow \infty} (\mathbf{p}^H \mathbf{q} / M) \xrightarrow{a.s.} 0$, where $\xrightarrow{a.s.}$ denotes almost sure convergence.

When all channel coefficients have been estimated, the data received at the i th BS is

$$\mathbf{y}_i^u [1] = \sqrt{P_u} \sum_{l=1}^L \sum_{t=1}^K \mathbf{g}_{lti} [1] \mathbf{q}_{lti} [1] + \mathbf{z}_i [1]. \quad (5)$$

Then we can use the similar method as in (4a), (4b), and (4c) to get the first UTs' uplink data

$$\hat{\mathbf{q}}_{l1i} [1] = \frac{\hat{\mathbf{g}}_{l1i}^H [1]}{\sqrt{P_u} \|\hat{\mathbf{g}}_{l1i} [1]\|^2} \mathbf{y}_i^u = \mathbf{q}_{l1i} [1]. \quad (6)$$

It is clear that, with the proposed pilot scheme, we get the first UTs' data of all cells without contamination. As for the other UTs in the first coherence interval, we combine the SIC method with the MMSE method to conduct the channel coefficient estimation. Then next, the m th UTs' channel coefficients estimations are taken for an example.

We assume that the data $\hat{\mathbf{q}}_{lti}[1]$ estimated by the way in (6) is accurate and can replace the real $\mathbf{q}_{lti}[1]$. Then, the interference caused by the other UTs' data when the m th UTs transmit pilot sequences can be removed by $\hat{\mathbf{q}}_{lti}[1]$ and $\hat{\mathbf{g}}_{lti}[1]$ ($t < m \leq K$), which are obtained before the present period [13]. The data received by the i th BS after processing is

$$\begin{aligned} f_i^m [1] &= \left(\mathbf{y}_i^m [1] - \sqrt{P_u} \sum_{l=1}^L \sum_{t=1}^{m-1} \hat{\mathbf{g}}_{lti} [1] \hat{\mathbf{q}}_{lti}^m [1] \right) \varphi_n^H \\ &= \left(\sqrt{P_p} \sum_{l=1}^L \mathbf{g}_{lmi} [1] \varphi_l \right) \varphi_n^H \\ &\quad + \left(\sqrt{P_u} \sum_{l=1}^L \sum_{t=1}^{m-1} \tilde{\mathbf{g}}_{lti} [1] \mathbf{q}_{lti}^m [1] + \mathbf{z}_i^m [1] \right) \varphi_n^H \\ &= \sqrt{P_p} \mathbf{g}_{nmi} [1] + \mathbf{o}_i^m [1], \end{aligned} \quad (7)$$

where $n = 1, 2, \dots, L$, $m = 2, 3, \dots, K$, and $\mathbf{o}_i^m[1]$ denotes the interference consisting of the estimation error and noise item. Obviously, by changing n , we can estimate the channel coefficients of the m th UTs in different cells to the i th cell. Based on the assumption that $\mathbf{q}_{lti}^m[1]$ is an independent Gaussian sequence and $\tilde{\mathbf{g}}_{lti}[1] \sim \mathcal{CN}(0, \varepsilon_{lti,1}^2 \mathbf{I}_M)$, we get

$$E \left[(\mathbf{o}_i^m [1]) (\mathbf{o}_i^m [1])^H \right] = \left(P_u \sum_{l=1}^L \sum_{t=1}^{m-1} \varepsilon_{lti,1}^2 + 1 \right) \mathbf{I}_M. \quad (8)$$

Note that $\mathbf{o}_i^m[1]$ is independent of $\mathbf{g}_{nmi}[1]$, and then we get the MMSE estimation of $\mathbf{g}_{nmi}[1]$ as

$$\hat{\mathbf{g}}_{nmi} [1] = \frac{\sqrt{P_p} \beta_{nmi}}{P_p \beta_{nmi} + P_u \sum_{l=1}^L \sum_{t=1}^{m-1} \varepsilon_{lti,1}^2 + 1} f_i^m [1]. \quad (9)$$

In the same way, the estimated channel coefficient can be decomposed as $\mathbf{g}_{nmi}[1] = \hat{\mathbf{g}}_{nmi}[1] + \tilde{\mathbf{g}}_{nmi}[1]$. From the properties of MMSE estimation, $\tilde{\mathbf{g}}_{nmi}[1] \sim \mathcal{CN}(0, \varepsilon_{nmi,1}^2 \mathbf{I}_M)$, where $\varepsilon_{nmi,1}^2 = \beta_{nmi} - \sigma_{nmi,1}^2$ and

$$\sigma_{nmi,1}^2 = \frac{P_p \beta_{nmi}^2}{P_u \sum_{l=1}^L \sum_{t=1}^{m-1} \varepsilon_{lti,1}^2 + 1 + P_p \beta_{nmi}}. \quad (10)$$

Next step, we use the estimated channel coefficients to detect the k th UTs' uplink data when the m th ($m > k$) UTs transmit pilot sequences. As the estimated channel coefficient $\hat{\mathbf{g}}_{nki}[1]$ is independent of $\mathbf{g}_{nki}[1]$ and similar to the steps in (4a), (4b), and (4c), at the i th BS, the detected data of the k th UT in the n th cell is

$$\hat{\mathbf{q}}_{nki}^m = \frac{\hat{\mathbf{g}}_{nki}^H [1] \mathbf{y}_i^m [1]}{\sqrt{P_u} \|\hat{\mathbf{g}}_{nki}^H [1]\|^2} = \mathbf{q}_{nki}^m. \quad (11)$$

Similar results can be gotten when UTs of all cells transmit uplink data

$$\hat{\mathbf{q}}_{nki} = \frac{\hat{\mathbf{g}}_{nki}^H [1] \mathbf{y}_i^u [1]}{\sqrt{P_u} \|\hat{\mathbf{g}}_{nki}^H [1]\|^2} = \mathbf{q}_{nki}. \quad (12)$$

From above equations, each BS can get all UTs' CSI and detect their uplink data in the first coherence interval.

Besides, the estimated channel coefficients can be used for the following downlink data precoding and interference cancellation.

In the next part, we will study the downlink data transmission with the proposed pilot scheme.

3.2. Downlink Data Transmission in the First Interval. With the estimated channel information, each BS calculates the beamforming vector to its k th UT in the normalized version that

$$\mathbf{w}_{ik} [1] = \frac{\hat{\mathbf{g}}_{iki} [1]}{\sqrt{K} \|\hat{\mathbf{g}}_{iki} [1]\|}. \quad (13)$$

The data received by the k th UT in the i th cell is

$$y_{ik}^d [1] = \sqrt{P_d} \sum_{l=1}^L \sum_{t=1}^K \mathbf{g}_{ikl}^H [1] \mathbf{w}_{lt} [1] \mathbf{s}_{lt} [1] + \mathbf{v}_{ik} [1], \quad (14)$$

where $\mathbf{v}_{ik}[1]$ is the unit variance additive white Gaussian noise in the downlink data transmission.

Note that the beamforming vector $\hat{\mathbf{g}}_{iki}[1]$ is independent of $\tilde{\mathbf{g}}_{iki}[1]$ and $\mathbf{g}_{lti}[1]$ ($(l, t) \neq (i, k)$), and we rewrite the norm of the estimated channel information as $\|\hat{\mathbf{g}}_{iki}[1]\| = a_{iki,1} \sqrt{M}$. The scalar $a_{iki,1} = \|\hat{\mathbf{g}}_{iki}[1]\| / \sqrt{M}$; we can derive the asymptotic behavior of $a_{iki,1}^2$ that $\lim_{M \rightarrow \infty} a_{iki,1}^2 \xrightarrow{a.s.} \sigma_{iki,1}^2$ [12] and then

$$\lim_{M \rightarrow \infty} \|\hat{\mathbf{g}}_{iki} [1]\| \xrightarrow{a.s.} \sqrt{M} \sigma_{iki,1}. \quad (15)$$

Then the downlink data estimation at the k th UT in the i th cell is

$$\hat{\mathbf{s}}_{ik} [1] = \frac{\sqrt{K} y_{ik}^d [1]}{\sqrt{P_d} \|\hat{\mathbf{g}}_{iki} [1]\|} \quad (16a)$$

$$\begin{aligned} &= \sum_{l=1}^L \sum_{t=1}^K \mathbf{g}_{ikl}^H [1] \frac{\hat{\mathbf{g}}_{ltl} [1]}{\|\hat{\mathbf{g}}_{ltl} [1]\|^2} \mathbf{s}_{lt} [1] \\ &\quad + \frac{\sqrt{K}}{\sqrt{M P_d}} \mathbf{v}_{ik} [1] \\ &= \hat{\mathbf{g}}_{iki}^H [1] \frac{\hat{\mathbf{g}}_{iki} [1]}{\|\hat{\mathbf{g}}_{iki} [1]\|^2} \mathbf{s}_{ik} [1] \\ &\quad + \hat{\mathbf{g}}_{iki}^H [1] \frac{\hat{\mathbf{g}}_{iki} [1]}{\|\hat{\mathbf{g}}_{iki} [1]\|^2} \mathbf{s}_{ik} [1] \end{aligned} \quad (16b)$$

$$\begin{aligned} &+ \sum_{\substack{l=1 \\ (l,t) \neq (i,k)}}^L \sum_{t=1}^K \mathbf{g}_{ikl}^H [1] \frac{\hat{\mathbf{g}}_{ltl} [1]}{\|\hat{\mathbf{g}}_{ltl} [1]\|^2} \mathbf{s}_{lt} [1] \\ &\quad + \frac{\sqrt{K}}{\sqrt{M P_d}} \mathbf{v}_{ik} [1] \\ &= \mathbf{s}_{ik} [1], \end{aligned} \quad (16c)$$

where we divide both the numerators and denominators in (16b) by M , and when $M \rightarrow \infty$, according to (15), the only left is the desired signal. In later intervals, we have the similar analytical approach for downlink data transmission.

The power of the interference plus noise is

$$\begin{aligned}
I_{ik,1}^m &= p_u \left| \hat{\mathbf{g}}_{iki}^H [1] \tilde{\mathbf{g}}_{iki} [1] \right|^2 + p_u \sum_{l=1}^L \sum_{t=1}^{m-1} \left| \hat{\mathbf{g}}_{iki}^H [1] \mathbf{g}_{lmi} [1] \right|^2 \\
&\quad + p_p \sum_{l=1}^L \left| \hat{\mathbf{g}}_{iki}^H [1] \mathbf{g}_{lmi} [1] \right|^2 + \left| \hat{\mathbf{g}}_{iki}^H [1] \mathbf{z}_{ik} [1] \right|^2 \\
&= M \sigma_{iki,1}^2 \left(p_u \sum_{l=1}^L \sum_{t=1}^{m-1} \beta_{lmi} - p_u \sigma_{iki,1}^2 + 1 + p_p \sum_{l=1}^L \beta_{lmi} \right). \tag{24}
\end{aligned}$$

According to (20), the achievable uplink rate is

$$\begin{aligned}
R_{ik,1}^m &= \log \left(1 + \frac{p_u (M+1) \sigma_{iki,1}^2}{p_u \sum_{l=1}^L \sum_{t=1}^{m-1} \beta_{lmi} - p_u \sigma_{iki,1}^2 + 1 + p_p \sum_{l=1}^L \beta_{lmi}} \right). \tag{25}
\end{aligned}$$

4.2. Uplink Data Transmission in the Second Part. After the channel coefficient estimation stage, all UTs transmit uplink data and this part exists in every coherence interval. Without loss of generality, we take the j th coherence interval for an example. The data of the k th UT received at the i th BS can be represented as

$$\begin{aligned}
\mathbf{y}_{ik}^u [j] &= \sqrt{p_u} \hat{\mathbf{g}}_{iki}^H [j] \hat{\mathbf{g}}_{iki} [j] + \sqrt{p_u} \tilde{\mathbf{g}}_{iki}^H [j] \tilde{\mathbf{g}}_{iki} [j] \\
&\quad + \sqrt{p_u} \sum_{l=1}^L \sum_{t=1}^K \hat{\mathbf{g}}_{iki}^H [j] \mathbf{g}_{lmi} [j] \mathbf{q}_{lmi} [j] \\
&\quad + \hat{\mathbf{g}}_{iki}^H [j] \mathbf{z}_i [j]. \tag{26}
\end{aligned}$$

The power of the desired signal is

$$P_{ik,j}^u = p_u (M^2 + M) \sigma_{iki,j}^4. \tag{27}$$

The power of the interference plus noise is

$$I_{ik,j}^u = M \sigma_{iki,j}^2 \left(1 + p_u \sum_{l=1}^L \sum_{t=1}^K \beta_{lmi} - p_u \sigma_{iki,j}^2 \right). \tag{28}$$

Then, the achievable uplink rate is

$$R_{ik,j}^u = \log \left(1 + \frac{p_u (M+1) \sigma_{iki,j}^2}{1 + p_u \sum_{l=1}^L \sum_{t=1}^K \beta_{lmi} - p_u \sigma_{iki,j}^2} \right). \tag{29}$$

4.3. Uplink Data Transmission in the Third Part. In this part, channel coefficient estimation is contaminated by all the other UTs' uplink data. When the m th UTs transmit pilot sequences, the data detection of the k th ($k > m$) UTs should use the estimated channel coefficients in the previous

coherence interval. For example, the data of the k th UT received at the i th BS can be represented as

$$\begin{aligned}
\mathbf{y}_{ik}^m [j] &= \sqrt{p_u} \hat{\mathbf{g}}_{iki}^H [j_1] \hat{\mathbf{g}}_{iki} [j_1] \mathbf{q}_{iki}^m [j] \\
&\quad + \sqrt{p_u} \tilde{\mathbf{g}}_{iki}^H [j_1] \tilde{\mathbf{g}}_{iki} [j_1] \mathbf{q}_{iki}^m [j] \\
&\quad + \sqrt{p_p} \sum_{l=1}^L \mathbf{g}_{lmi} [j] \varphi_l \\
&\quad + \sqrt{p_u} \sum_{l=1}^L \sum_{t=1}^{m-1} \mathbf{g}_{lmi} [j] \mathbf{q}_{lmi}^m [j] \\
&\quad + \sqrt{p_u} \sum_{l=1}^L \sum_{t=m+1}^K \mathbf{g}_{lmi} [j-1] \mathbf{q}_{lmi}^m [j] + \mathbf{z}_i^m [j], \tag{30}
\end{aligned}$$

where $j_1 = (j, j < m; j-1, j > m)$. The power of the desired signal is

$$P_{ik,j}^m = p_u (M^2 + M) \sigma_{iki,j}^4. \tag{31}$$

The power of the interference plus noise is

$$\begin{aligned}
I_{ik,j}^m &= M \sigma_{iki,j}^2 \left(1 + p_p \sum_{l=1}^L \beta_{lmi} + p_u \sum_{l=1}^L \sum_{t=1, t \neq m}^K \beta_{lmi} \right. \\
&\quad \left. - p_u \sigma_{iki,j}^2 \right). \tag{32}
\end{aligned}$$

The achievable uplink data rate is

$$\begin{aligned}
R_{ik,j}^m &= \log \left(1 + \frac{p_u (M+1) \sigma_{iki,j}^2}{1 + p_p \sum_{l=1}^L \beta_{lmi} + p_u \sum_{l=1}^L \sum_{t=1, t \neq m}^K \beta_{lmi} - p_u \sigma_{iki,j}^2} \right). \tag{33}
\end{aligned}$$

4.4. Downlink Data Transmission in the Fourth Part. After uplink data transmission stage, BSs transmit data to UTs with the estimated channel coefficients. According to (13) and (14), the data received by the k th UT of the i th cell can be rewritten as

$$\begin{aligned}
\mathbf{y}_{ik}^d [j] &= \sqrt{p_d} \sum_{l=1}^L \sum_{t=1}^K \hat{\mathbf{g}}_{iki}^H [j] \mathbf{w}_{lt} [j] \mathbf{s}_{lt} [j] + \mathbf{v}_{ik} [j] \\
&= \sqrt{p_d} \frac{(\hat{\mathbf{g}}_{iki}^H [j] + \tilde{\mathbf{g}}_{iki}^H [j]) \hat{\mathbf{g}}_{iki} [j]}{\sqrt{K} \|\hat{\mathbf{g}}_{iki} [j]\|} \mathbf{s}_{ik} [j] \\
&\quad + \sqrt{p_d} \sum_{l=1}^L \sum_{t=1}^K \frac{\hat{\mathbf{g}}_{iki}^H [j] \hat{\mathbf{g}}_{lmi} [j]}{\sqrt{K} \|\hat{\mathbf{g}}_{lmi} [j]\|} \mathbf{s}_{lt} [j] + \mathbf{v}_{ik} [j]. \tag{34}
\end{aligned}$$

Applying similar analytical procedures for the uplink, it is not hard to get the UT's downlink achievable rate

$$R_{ik,j}^d = \log \left(1 + \frac{p_d (M+1) \sigma_{iki,j}^2}{K p_d \sum_{l=1}^L \beta_{ikl} - p_d \sigma_{iki,j}^2 + K} \right). \quad (35)$$

4.5. Conventional Transmission as a Benchmark. For data transmission with the conventional pilot scheme, as shown in Figure 1, it is obvious that the transmit pattern is the same during every coherence interval. Hence, the uplink data of the k th UTs received at the i th BS is [12]

$$\begin{aligned} \mathbf{y}_{ik}^u &= \mathbf{g}_{iki}^H \left(\sqrt{p_u} \sum_{l=1}^L \sum_{t=1}^K \mathbf{g}_{lti} q_{lt} + \mathbf{v}_{ik} \right) \\ &= \left(\sqrt{p_p} \sum_{l=1}^L \mathbf{g}_{lki} + \mathbf{z}_{ik} \right)^H \left(\sqrt{p_u} \sum_{l=1}^L \sum_{t=1}^K \mathbf{g}_{lti} q_{lt} + \mathbf{v}_{ik} \right) \\ &= \sum_{l_1=1}^L \sum_{l_2=1}^L \sum_{t=1}^K \sqrt{p_u p_p} \mathbf{g}_{l_1 k i}^H \mathbf{g}_{l_2 t i} q_{l_2 t} + \sqrt{p_p} \sum_{l=1}^L \mathbf{g}_{l k i}^H \mathbf{v}_{ik} \\ &\quad + \sqrt{p_u} \sum_{l=1}^L \sum_{t=1}^K \mathbf{z}_{ik}^H \mathbf{g}_{l t i} q_{lt} + \mathbf{z}_{ik}^H \mathbf{v}_{ik}. \end{aligned} \quad (36)$$

$$\zeta_{ik}^u$$

$$= \frac{(M+1) \beta_{iki}^2}{\left(\sum_{l_1=1}^L \sum_{l_2=1, l_2 \neq l_1}^L \sum_{t=1}^K \beta_{l_1 k i} \beta_{l_2 t i} + \sum_{t=1, t \neq k}^K \beta_{i k t} \beta_{t i} + \sum_{l=1, l \neq i}^L (M+1) \beta_{l k i}^2 + \sum_{l=1, l \neq i}^L \sum_{t=1, t \neq k}^K \beta_{l k i} \beta_{t i} + (1/p_u) \sum_{l=1}^L \beta_{l k i} + 1/p_p p_u K + (1/p_p) \sum_{l=1}^L \sum_{t=1}^K \beta_{l t i} \right)}, \quad (38)$$

$$R_{ik}^u = \log(1 + \zeta_{ik}^u).$$

For conventional downlink data transmission, consider the pilot contamination and the data received by the k th UT in the i th cell is

$$\begin{aligned} \mathbf{y}_{ik}^d &= \sqrt{p_d} \sum_{l=1}^L \sum_{t=1}^K \mathbf{g}_{lki}^H \mathbf{w}_{l t i} \mathbf{s}_{lt} + \mathbf{v}_{ik} = \frac{\sqrt{p_d}}{\sqrt{K}} \\ &\cdot \sum_{l=1}^L \sum_{t=1}^K \mathbf{g}_{lki}^H \frac{\widehat{\mathbf{g}}_{l t i}}{\|\widehat{\mathbf{g}}_{l t i}\|} \mathbf{s}_{lt} + \mathbf{v}_{ik} = \frac{\sqrt{p_d}}{\sqrt{K}} \sum_{l=1}^L \sum_{t=1}^K \frac{\mathbf{g}_{l k i}^H}{\|\widehat{\mathbf{g}}_{l t i}\|} \\ &\cdot \left(\sqrt{p_p} \sum_{l_1=1}^L \mathbf{g}_{l_1 t i} + \mathbf{z}_i \right) \mathbf{s}_{lt} + \mathbf{v}_{ik} \end{aligned}$$

$$\zeta_{ik}^d$$

$$= \frac{(M^2 + M) \beta_{iki}^2}{\left(\sum_{l=1, l \neq i}^L (M^2 + M) \beta_{ikl}^2 + \sum_{l=1}^L \sum_{t=1, t \neq k}^K \beta_{ikl}^2 + \sum_{l=1}^L \sum_{t=1}^K \sum_{l_1=1, l_1 \neq i}^L (\beta_{ikl}^2 \beta_{l_1 t i}^2 / \beta_{l t i}^2) + (1/p_p) \sum_{l=1}^L \sum_{t=1}^K (\beta_{ikl}^2 / \beta_{l t i}^2) + K/p_p \right)}, \quad (40)$$

$$R_{ik}^d = \log(1 + \zeta_{ik}^d).$$

Then the power of the received signal is

$$\begin{aligned} P_{ik}^u &= p_u p_p \left\{ \mathbf{g}_{iki}^H \mathbf{g}_{iki} \right\} \text{desired signal} \\ &\quad + p_u p_p \sum_{l_1=1}^L \sum_{l_2=1}^L \sum_{t=1}^K \left| \mathbf{g}_{l_1 k i}^H \mathbf{g}_{l_2 k i} \right| \\ &\quad + p_u p_p \sum_{l=1, l \neq i}^L \sum_{t=1, t \neq k}^K \left| \mathbf{g}_{l k i}^H \mathbf{g}_{l t i} \right|^2 + p_p \sum_{l=1}^L \left| \mathbf{g}_{l k i}^H \mathbf{v}_{ik} \right|^2 \\ &\quad + p_u p_p \sum_{t=1, t \neq k}^K \left| \mathbf{g}_{i k t}^H \mathbf{g}_{t i} \right|^2 + p_u p_p \sum_{l=1, l \neq i}^L \left| \mathbf{g}_{l k i}^H \mathbf{g}_{l k i} \right|^2 \\ &\quad + p_u \sum_{l=1}^L \left| \mathbf{z}_{ik}^H \mathbf{g}_{l t i} \right|^2 + \left| \mathbf{z}_{ik}^H \mathbf{v}_{ik} \right|^2. \end{aligned} \quad (37)$$

According to Lemma 2, we get the achievable rate of the k th UT

$$\begin{aligned} &= \frac{\sqrt{p_d p_p}}{\sqrt{K}} \left(\frac{\mathbf{g}_{iki}^H \mathbf{g}_{iki} \mathbf{s}_{ik}}{\|\widehat{\mathbf{g}}_{iki}\|} + \sum_{l=1}^L \sum_{t=1}^K \sum_{l_1=1, l_1 \neq i}^L \mathbf{g}_{l k i}^H \frac{\mathbf{g}_{l_1 t i}}{\|\widehat{\mathbf{g}}_{l_1 t i}\|} \mathbf{s}_{l_1 t} \right. \\ &\quad + \sum_{l=1, l \neq i}^L \mathbf{g}_{l k i}^H \frac{\mathbf{g}_{l k l}}{\|\widehat{\mathbf{g}}_{l k l}\|} \mathbf{s}_{lk} + \frac{1}{\sqrt{p_p}} \sum_{l=1}^L \sum_{t=1}^K \frac{\mathbf{g}_{l k i}^H \mathbf{z}_i \mathbf{s}_{lt}}{\|\widehat{\mathbf{g}}_{l t i}\|} \\ &\quad \left. + \sum_{l=1}^L \sum_{t=1, t \neq k}^K \mathbf{g}_{l k i}^H \frac{\mathbf{g}_{i t l}}{\|\widehat{\mathbf{g}}_{i t l}\|} \mathbf{s}_{lt} \right) + \mathbf{v}_{ik}. \end{aligned} \quad (39)$$

Similar analytical procedures are applied and the achievable rate can be represented as

For further comprehension, we divide both the numerators and denominators in (40) by M , and when $M \rightarrow \infty$, we get

$$\zeta_{ik}^d = \frac{\beta_{iki}^2}{\sum_{l=1, l \neq i}^L \beta_{ikl}^2} \quad (41)$$

which is the same as the result in [13].

Comparing (25), (29), and (33) with (38) and (35) with (40), the achievable rate in the conventional pilot scheme has large denominators due to pilot contamination, which is not the case in the proposed pilot scheme. Therefore, from all the above theoretical analysis, the proposed pilot scheme can achieve a better tradeoff between pilot resource consumption and CSI estimation accuracy and it outperforms the conventional one in many scenarios. In the next section, we will show the superiority of the proposed pilot scheme by some numerical results.

5. Numerical Results

In this section, some numerical results are shown about the proposed pilot scheme. The achievable rate of uplink and downlink data transmission are added up for better performance comparison and the average achievable rate of each cell is used as a performance indicator. Besides, the overall power of the conventional pilot scheme and the proposed pilot scheme is set to be the same.

The scenarios simulated here consist of a cellular system with K users uniformly distributed in each cell and the cell number is set to 3. Without loss of generality, assume that large-scale fading coefficients from the BS to the UTs in the same cell are 1 and each BS is equipped with $M = 128$ antennas. For simplicity, we set $p_u = p_p = p_d$.

First, we calculate the average achievable rate of each cell and compare our proposed pilot scheme with the conventional one under different coherence intervals N_c when SNR varies from -40 dB to 60 dB. In this simulation, the cross large-scale fading coefficients which are the coefficients from the BS to the UTs in other cells are all set to 0.5 ($\beta_c = 0.5$). The result is shown in Figure 3.

The simulation result in Figure 3 shows the superiority of the proposed pilot scheme in mitigating the pilot contamination. The average achievable rate of the proposed scheme with different N_c surpasses the conventional one when SNR varies from -8 dB to 60 dB and still grows with SNR, while that of the conventional pilot design tends to saturate in a low SNR. Besides, a larger N_c brings more CSI estimation error which leads to a smaller average achievable rate. However, N_c does not impact more on the comparison.

Then we set $N_c = 3$ and compare the performance between two pilot scheme under different cross large-scale fading coefficients β_c .

Figure 4 shows the average achievable rate for β_c from 0.4 to 0.7 under varying SNR condition. Obviously, from (9) and (10), a large β_c brings more CSI estimation error for the proposed pilot scheme which has a negative effect on the average achievable rate, while that of the conventional one

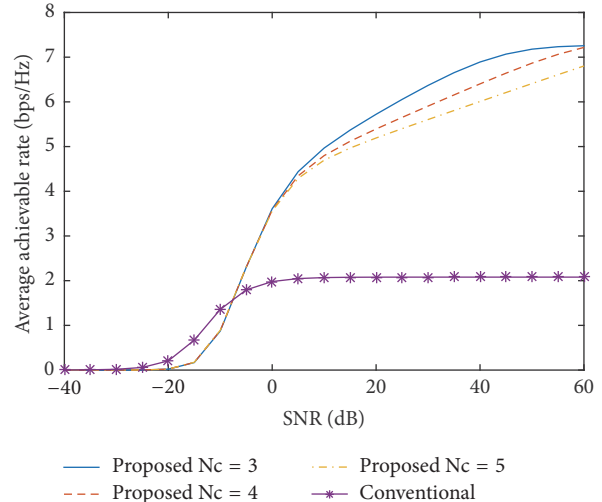


FIGURE 3: Average achievable rate comparison versus different N_c ($T = 15$, $D = 3$, and $K = 3$).

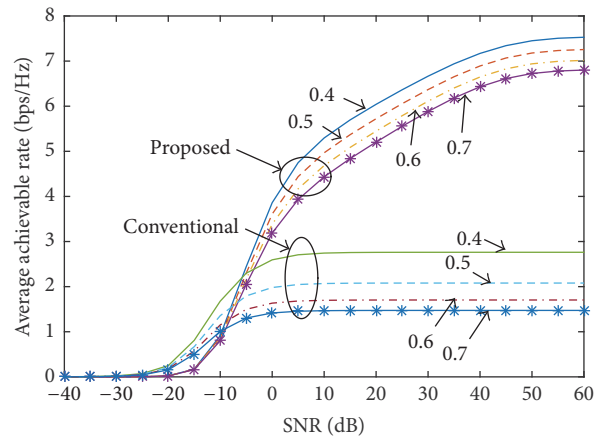


FIGURE 4: Average achievable rate comparison versus different β_c ($T = 15$, $D = 3$, and $K = 3$).

suffers from the pilot contamination and achieves a much lower average achievable rate than the proposed one.

In Figure 5, we investigate the influence of the antenna number on the average achievable rate. It can be observed that the proposed pilot scheme clearly outperforms conventional one over the whole range of antenna number. It is also evident that the average achievable rate of the proposed pilot scheme grows with the antenna number while that of the conventional one does not change. This strengthens the superiority of the proposed pilot scheme.

6. Conclusion

This paper proposes a novel time-shift pilot scheme in TDD large-scale multicell multiuser MIMO system, in which, UTs within a cell transmit the same pilot sequence in a time-shift manner while pilot sequences assigned to different cells are mutually orthogonal. By using this pilot scheme, we can effectively alleviate the pilot contamination. Simulation

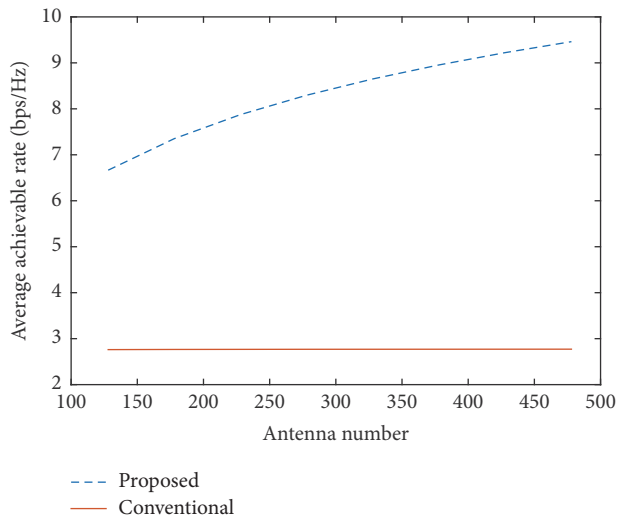


FIGURE 5: Average achievable rate comparison versus antenna number ($T = 15$, $D = 3$, $K = 3$, $SNR = 30$ dB, and $N_c = 3$).

results show that the performance of the proposed scheme outperforms the conventional one under several different scenarios and particularly the proposed pilot is more potential when the antenna number is large. However, a large coherence interval N_c and cross large-scale fading coefficients β_c will bring more CSI estimation errors which is not good for the overall achievable rate. Our next work will focus on this problem to investigate a higher performance method.

Competing Interests

The authors declare that there is no conflict of interests regarding the publication of this paper.

References

- [1] E. G. Larsson, O. Edfors, F. Tufvesson, and T. L. Marzetta, "Massive MIMO for next generation wireless systems," *IEEE Communications Magazine*, vol. 52, no. 2, pp. 186–195, 2014.
- [2] L. Lu, G. Y. Li, A. L. Swindlehurst, A. Ashikhmin, and R. Zhang, "An overview of massive MIMO: benefits and challenges," *IEEE Journal on Selected Topics in Signal Processing*, vol. 8, no. 5, pp. 742–758, 2014.
- [3] T. L. Marzetta, "Massive MIMO: an introduction," *Bell Labs Technical Journal*, vol. 20, pp. 11–12, 2015.
- [4] F. Rusek, D. Persson, B. K. Lau et al., "Scaling up MIMO: opportunities and challenges with very large arrays," *IEEE Signal Processing Magazine*, vol. 30, no. 1, pp. 40–60, 2013.
- [5] H. Shuangfeng, I. Chih-Lin, X. Zhikun, and C. Rowell, "Large-scale antenna systems with hybrid analog and digital beamforming for millimeter wave 5G," *IEEE Communications Magazine*, vol. 53, no. 1, pp. 186–194, 2015.
- [6] X. Yan, H. Yin, M. Xia, and G. Wei, "Pilot sequences allocation in TDD massive MIMO systems," in *Proceedings of the IEEE Wireless Communications and Networking Conference (WCNC '15)*, pp. 1488–1493, March 2015.
- [7] N. Liang, W. Zhang, and C. Shen, "An uplink interference analysis for massive MIMO systems with MRC and ZF receivers," in *Proceedings of the IEEE Wireless Communications and Networking Conference (WCNC '15)*, pp. 310–315, San Francisco, Calif, USA, March 2015.
- [8] H. Yin, D. Gesbert, M. C. Filippou, and Y. Liu, "Decontaminating pilots in massive MIMO systems," in *Proceedings of the IEEE International Conference on Communications (ICC '13)*, pp. 3170–3175, IEEE, Budapest, Hungary, June 2013.
- [9] T. E. Bogale and L. B. Le, "Pilot optimization and channel estimation for multiuser massive MIMO systems," in *Proceedings of the 48th Annual Conference on Information Sciences and Systems (CISS '14)*, pp. 1–6, Princeton, NJ, USA, March 2014.
- [10] A. Hu, T. Lv, H. Gao, Y. Lu, and E. Liu, "Pilot design for large-scale multi-cell multiuser MIMO systems," in *Proceedings of the IEEE International Conference on Communications (ICC '13)*, pp. 5381–5385, Budapest, Hungary, June 2013.
- [11] D. Wang, X. Wang, X. Yang, Y. Zhao, and W. Wan, "Design of downlink training sequences for FDD massive MIMO systems," in *Proceedings of the IEEE International Conference on Communications (ICC '15)*, pp. 4570–4575, London UK, June 2015.
- [12] F. Fernandes, A. Ashikhmin, and T. L. Marzetta, "Inter-cell interference in noncooperative TDD large scale antenna systems," *IEEE Journal on Selected Areas in Communications*, vol. 31, no. 2, pp. 192–201, 2013.
- [13] X. Zheng, H. Zhang, W. Xu, and X. You, "Semi-orthogonal pilot design for massive MIMO systems using successive interference cancellation," in *Proceedings of the IEEE Global Communications Conference (GLOBECOM '14)*, pp. 3719–3724, Austin, Tex, USA, December 2014.
- [14] H. Q. Ngo, E. G. Larsson, and T. L. Marzetta, "Energy and spectral efficiency of very large multiuser MIMO systems," *IEEE Transactions on Communications*, vol. 61, no. 4, pp. 1436–1449, 2013.
- [15] A. I. Khuri, *Advanced Calculus with Applications in Statistics*, vol. 486, John Wiley & Sons, 2003.

Research Article

Connectivity Analysis of Millimeter-Wave Device-to-Device Networks with Blockage

Haejoon Jung¹ and In-Ho Lee²

¹The Department of Information and Telecommunication Engineering, Incheon National University, Incheon 22012, Republic of Korea

²The Department of Electrical, Electronic and Control Engineering, Hankyong National University, Anseong 456-749, Republic of Korea

Correspondence should be addressed to In-Ho Lee; ihlee@hknu.ac.kr

Received 3 August 2016; Revised 8 October 2016; Accepted 17 October 2016

Academic Editor: Mohammad Abdul Matin

Copyright © 2016 H. Jung and I.-H. Lee. This is an open access article distributed under the Creative Commons Attribution License, which permits unrestricted use, distribution, and reproduction in any medium, provided the original work is properly cited.

We consider device-to-device (D2D) communications in millimeter-wave (mm Wave) for the future fifth generation (5G) cellular networks. While the mm Wave systems can support multiple D2D pairs simultaneously through beamforming with highly directional antenna arrays, the mm Wave channel is significantly more susceptible to blockage compared to microwave; mm Wave channel studies indicate that if line-of-sight (LoS) paths are blocked, reliable mm Wave communications may not be achieved for high data-rate applications. Therefore, assuming that an outage occurs in the absence of the LoS path between two wireless devices by obstructions, we focus on connectivity of the mm Wave D2D networks. We consider two types of D2D communications: direct and indirect schemes. The connectivity performances of the two schemes are investigated in terms of (i) *the probability to achieve a fully connected network* P_{FC} and (ii) *the average number of reliably connected devices* γ . Through analysis and simulation, we show that, as the network size increases, P_{FC} and γ decrease. Also, P_{FC} and γ decrease, when the blockage parameter increases. Moreover, simulation results indicate that the hybrid direct and indirect scheme can improve both P_{FC} and γ up to about 35% compared to the nonhybrid scheme.

1. Introduction

With rapidly growing volume of mobile devices, the demand for capacity in mobile broadband communications increases dramatically. As a result, wireless industry is required to seek greater capacity and find new wireless spectrum beyond fourth generation (4G) standards. For this reason, fifth generation (5G) is envisioned to have significantly greater spectrum allocations at millimeter-wave (mm Wave) frequency bands, highly directional antenna arrays, larger coverage area, lower infrastructure costs, and higher aggregate capacity for many simultaneous users [1, 2]. While microwave communication systems suffer from the limited spectrum, the bandwidths of several gigahertz could be available at mm Wave frequencies for 5G communication systems.

Moreover, instead of the complete control at the infrastructure side, 5G systems will exploit intelligence at the device side within different layers of the protocol stack by allowing device-to-device (D2D) connectivity [3]. The

direct communications between nearby mobile devices can provide higher spectrum utilization, enhanced throughput, and better energy efficiency, while facilitating new peer-to-peer applications and location-based services such as 3GPP Proximity Services (ProSe) [4] and IEEE 802.15 Peer-Aware Communications (PAC) [5]. Along the lines of the increasing demand of such high-rate local services, local D2D communications have been studied as underlay to Long Term Evolution-Advanced (LTE-A) 4G cellular networks [6]. As highlighted in [6, 7], the main challenge of a D2D-enabled air interface for the cellular networks is how to share wireless resources between cellular and D2D communications. For instance, the local D2D communications should use orthogonal channels or opportunistically access the spectrum occupied by cellular communications.

In this context, we consider D2D communications in the mm Wave frequency bands for the future cellular network, because the mm Wave can aid a resource sharing scheme between the D2D and cellular communications, which supports

noninterfering concurrent links. To be specific, directional antenna arrays in mm Wave can reduce cochannel interference and improve spatial reuse of communication systems through large beamforming gain. This characteristic of mm Wave systems is also desirable to guarantee connectivity between a huge number of devices in the future wireless networks [8]. In other words, thanks to highly directional beam in mm Wave, a user equipment (UE) can communicate with another UE in proximity over a D2D link, which enables multiple D2D pairs to use the same radio resources simultaneously.

However, compared to microwave, an mm Wave communication channel experiences higher path-loss and is susceptible to blockage such as walls, trees, or even human bodies, as revealed in [2, 9, 10]. Hence, the mm Wave communication channel is a nearly bimodal channel depending on the existence of line-of-sight (LoS) path [11]. Based on this property of the mm Wave propagation, a new channel model is introduced in [12], which characterizes large-scale blockage effects using random shape theory [13]. The model proposed in [12] shows that the probability of a blockage event between two radios increases exponentially, as the separation between the two increases. This propagation model has been applied to analyze various wireless communication systems using mm Wave. The author of [14] derives the outage probability improved by macrodiversity with multiple base stations (BSs), assuming the outage event occurs when the LoS path is blocked. The authors in [15] analyze the coverage and rate performance in mm Wave cellular networks. Moreover, [16] presents the outage performance of the mm Wave wireless backhaul link between a 5G macro base station (MBS) and small-cell base stations (SBSs). Assuming Poisson point process (PPP) on the plane, the stochastic geometry used in these studies is known to be an effective tool to evaluate system performances in the cellular networks [17].

In this paper, based on the framework in [12, 14], we consider D2D connectivity in mm Wave networks. Reliable D2D connections are required for D2D data transmissions as well as cellular data offloading onto D2D connections, which can provide considerable wireless capacity gains [18]. In mm Wave 5G cellular networks, two kinds of D2D communications can be enabled: *direct communications* between two wireless devices in proximity and *indirect communications*, which connect two devices through base station(s) [8]. In this paper, we investigate both types of the D2D communications assuming a network consisting of one mm Wave BS and multiple wireless devices distributed according to a two-dimensional Poisson point process (PPP).

The contributions of this paper are fourfold. First, we derive the probability distribution, mean, and variance of the interdevice distance (i.e., the distance between two randomly located devices). Second, we derive the probability that the D2D network is *fully connected*, which means that all the wireless devices have reliable communication links to each other [19]. Third, we also quantify the D2D connectivity in terms of the average number of reliable connections (or communication links) both for the direct and indirect D2D

communication systems. Lastly, we consider a hybrid scheme, in which both the direct and indirect communications can be selectively used and present the simulation results to compare the performances of the direct and indirect schemes.

This paper is organized as follows. The system model is introduced in Section 2. The direct and indirect D2D communication systems are analyzed in Sections 3 and 4, respectively. Numerical results are presented in Section 5. Conclusions are provided in Section 6.

2. System Model

We consider a 5G cellular network enabled with D2D communications with two tiers: the cell tier and the device tier. The conventional cellular communications are supported by the cell (macro or small-cell) tier, while D2D communications are covered by the device tier. The BS may have a full or partial control over the D2D communications depending on the system architecture to establish and manage the D2D links. In this paper, we focus on the connectivity of the D2D links, which indicates the potential extent of cellular data offloading onto D2D connections. Thus, the analysis in this paper does not depend on specific design aspects of the network architecture. Based on [12], we focus on outdoor environments.

We assume mm Wave 5G communication systems as shown in Figures 1(a) and 1(b), which illustrate direct and indirect D2D communications, respectively. In both cases, we assume N devices are uniformly distributed over Area \mathcal{S} (i.e., the area of the gray circle with radius R) with intensity λ , which means the average number of devices per unit area (i.e., devices/m²), according to homogeneous PPP [20]. We assume a quasi-stationary scenario, where the network topology is stationary while D2D communications are performed.

For the indirect D2D communications in Figure 1(b), at the center of the circle, there exists a single mm Wave BS, which can be a small-cell BS with low power and low cost in heterogeneous networks. We note that we do not consider indirect (multihop) communications via devices as relays, because of the complexity to build a multihop route with directional antennas in the mobile scenario. In both types of D2D networks, the number of the devices in the network is assumed to be N , which is a random variable following Poisson probability distribution as $P_N(n) = ((\lambda\pi R^2)^n / n!)e^{-\lambda\pi R^2}$, where $P_N(n)$ is the probability that there are n devices in Area \mathcal{S} , and n is a nonnegative integer. Therefore, the average number of the devices is given by $\mathbb{E}\{N\} = \lambda\pi R^2$, where $\mathbb{E}\{\cdot\}$ is the expectation operator.

As in [15], for analytical tractability, we assume the sectored antenna model, which characterizes key features of an antenna pattern. As noted in [8], the interference issue by concurrent cochannel links with omnidirectional antennas is of little concern in the mm Wave communications with highly directional antenna arrays. We assume that directional beamforming is performed at devices as well as the mm Wave BS. We note a half-duplex system is assumed. Therefore, instead of the interference-limited performance metric

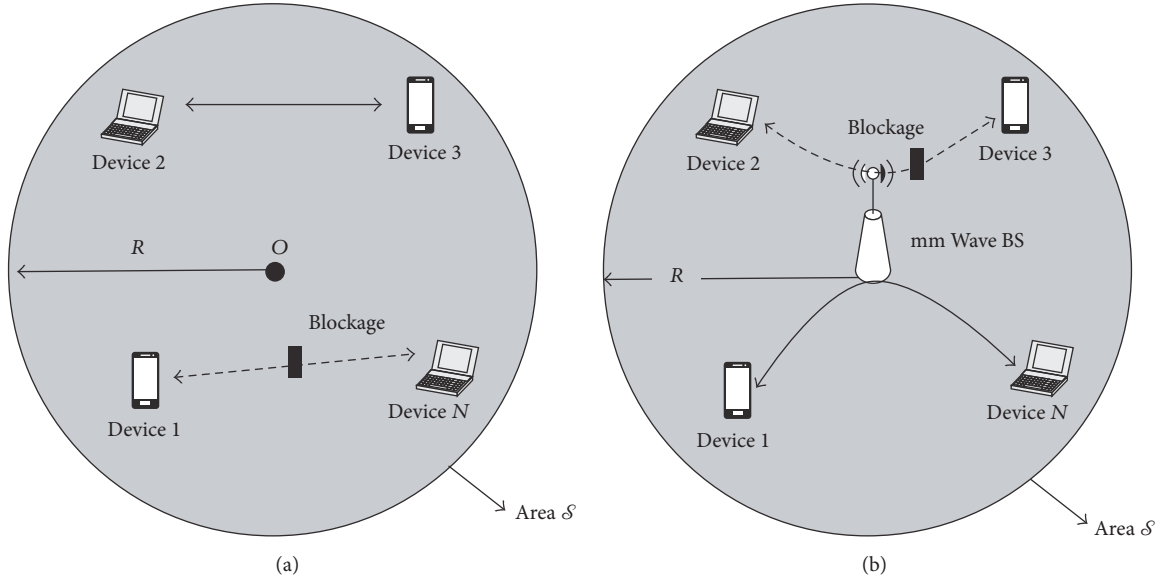


FIGURE 1: Two types of mm Wave D2D communications: (a) direct D2D communications and (b) indirect D2D communications.

(e.g., signal-to-noise-plus-interference ratio), the blockage problem of line-of-sight (LoS) paths may induce an outage event in mm Wave communications, especially for high-speed data transfer in multimedia or interactive applications. As in [12, 14, 16], blockages are assumed to be impenetrable. Also, following [12, 14, 16], we define an outage event as the case that the LoS path is blocked by obstacles.

In case of the direct D2D communications, suppose $d_{i,j}$ is the distance between devices i and j . As in [12, 14–16], the probability of no blockage in the LoS path between the two devices is $P_{\text{LoS},i,j} = e^{-\beta d_{i,j}}$, where β is the parameter that captures density and size of obstacles, which cause an outage due to blockage. The greater β means obstacles with higher density and larger sizes, which results in lower $P_{\text{LoS},i,j}$ [12]. In this paper, we assume $P_{\text{LoS},i,j}$ can be interpreted as the probability that the communication link between devices i and j is reliable. In other words, if the LoS path is blockage-free, we declare the corresponding communication (or connection) is reliable.

As in [12, 14, 15], for analytical tractability, we assume the blockage events on different mm Wave links are mutually independent. For example, if there are three wireless terminals 1, 2, and 3, where they can be either the mm Wave BS or a device, the three possible communication links (i.e., 1-2, 1-3, and 2-3) have independent outage events. In general, depending on the location of wireless terminals, blockage events are not independent. For example, if the angle between two links with a common end-point or start-point (e.g., 1-2 and 1-3) is narrow enough, the two D2D links might experience the same blockage effect. Therefore, the probability of a fully connected D2D network derived in this paper may be an upper bound as the references of system design and analysis. Moreover, we note that the numerical results in [12] show that the error caused by the *independent link assumption* is minor and acceptable in accuracy.

3. Direct D2D Communications

In this section, we consider direct D2D communications, which do not require infrastructure such as BSs. With directional antenna arrays in mm Wave, noninterfering concurrent D2D pairs are able to share radio resources, which significantly enhances network capacity. Assuming the spatially uniform distribution of the devices, we will explore various aspects of the direct D2D communications.

3.1. Probability Distribution of $d_{i,j}$. To investigate the performance of the mm Wave communications between two devices, we first consider the probability distribution function (PDF) of $d_{i,j}$, since $P_{\text{LoS},i,j}$ is a function of $d_{i,j}$, which is a random variable. Using Crofton's *fixed point theorem* in [21], we derive the PDF of $d_{i,j}$. Fixed point theorem permits the evaluation of some definite integrals without directly performing the integrations, which is especially useful to derive geometric probability distributions. Suppose that there are n points $\xi_1, \xi_2, \dots, \xi_n$, which are randomly distributed on a domain \mathcal{S} . Let Q be an event that depends on the position of the n points, and let $d\mathcal{S}$ be an infinitesimal boundary of \mathcal{S} . Then, Crofton's fixed point theorem gives the following formula:

$$d \Pr [Q] = \frac{n (\Pr [Q | \xi_1 \in d\mathcal{S}] - \Pr [Q])}{\mathcal{S}} d\mathcal{S}, \quad (1)$$

where $\Pr [Q | \xi_1 \in d\mathcal{S}]$ is the probability that Q occurs when one of the random points ξ_1 is on the boundary $d\mathcal{S}$ of \mathcal{S} .

To derive the PDF of $d_{i,j}$, suppose that Q is the event that two points (i.e., $n = 2$) in the circle with the radius R (i.e., $\mathcal{S} = \pi R^2$) are separated by a distance between x and $x + dx$, as shown in Figure 2. Also, let C be the event that one point is on the circumference $d\mathcal{S}$. The probability of the event Q is

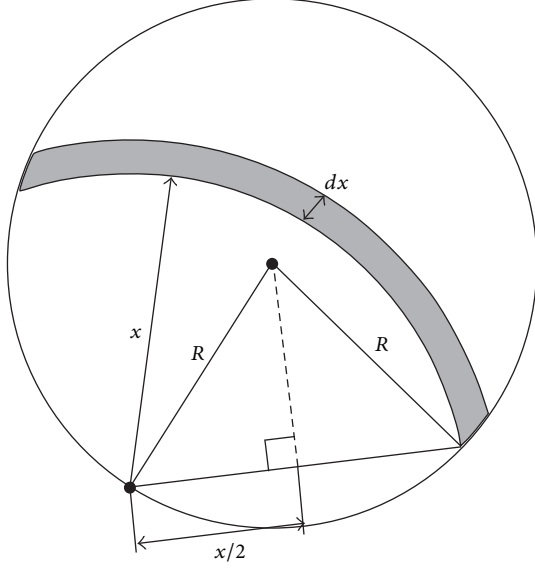


FIGURE 2: Illustration to derive the PDF of $d_{i,j}$.

denoted by $\Pr[Q]$, and the conditional probability of Q given C is denoted by $\Pr[Q | C]$. From (1), we have

$$\begin{aligned} d \Pr [Q] &= \frac{2 (\Pr [Q | C] - \Pr [Q])}{\mathcal{S}} d\mathcal{S} \\ &= \frac{2 (\Pr [Q | C] - \Pr [Q])}{\pi R^2} 2\pi R dR \\ &= \frac{4 (\Pr [Q | C] - \Pr [Q])}{R} dR, \end{aligned} \quad (2)$$

where $\Pr[Q | C]$ is given by

$$\Pr [Q | C] = \frac{2x dx \cos^{-1} (x/2R)}{\pi R^2}. \quad (3)$$

Therefore, when plugging (3) into (2), it gives

$$R d \Pr [Q] + 4 \Pr [Q] dR = \frac{8x dx \cos^{-1} (x/2R)}{\pi R^2} dR. \quad (4)$$

Multiplying both sides by R^3 , we obtain

$$\begin{aligned} R^4 d \Pr [Q] + 4R^3 \Pr [Q] dR \\ = \frac{8R x dx \cos^{-1} (x/2R)}{\pi} dR. \end{aligned} \quad (5)$$

Thus, if we integrate both sides, it gives

$$\begin{aligned} R^4 \Pr [Q] &= \frac{4x^2 dx}{\pi} \int \frac{2R}{x} \cos^{-1} \left(\frac{x}{2R} \right) dR \\ &= \frac{x dx}{\pi} \left(4R^2 \cos^{-1} \left(\frac{x}{2R} \right) - 2xR \sqrt{1 - \frac{x^2}{4R^2}} \right) + K, \end{aligned} \quad (6)$$

where the constant $K = 0$, because $\Pr[Q] = 0$ when $R = x/2$. Hence, the PDF of $d_{i,j}$ is expressed as

$$\begin{aligned} f_{d_{i,j}} (x) &= \frac{\Pr [Q]}{dx} \\ &= \frac{2x}{\pi R^2} \left(2 \cos^{-1} \left(\frac{x}{2R} \right) - \frac{x}{R} \sqrt{1 - \frac{x^2}{4R^2}} \right), \end{aligned} \quad (7)$$

where $0 < x < 2R$. The derived PDF in (7) is the same as [22]. The mean and variance of $d_{i,j}$ are given by $\mathbb{E}\{d_{i,j}\} = 128R/45\pi$ and $\mathbb{V}\{d_{i,j}\} = R^2 - (128R/45\pi)^2$, respectively.

3.2. Fully Connected Network via Direct D2D Communications. In this section, we derive the probability that all the wireless devices are interconnected via direct D2D communications in mm Wave. Suppose a Bernoulli random variable $U_{i,j}$ is defined as

$$U_{i,j} = \begin{cases} 1, & \text{w.p. } P_{\text{LoS};i,j} = \exp(-\beta d_{i,j}), \\ 0, & \text{w.p. } 1 - P_{\text{LoS};i,j} = 1 - \exp(-\beta d_{i,j}), \end{cases} \quad (8)$$

where if $U_{i,j} = 1$, it means that the mm Wave link between devices i and j is reliable. In other words, following assumption of impenetrable blockage in [12, 14], we declare an outage event of the direct D2D transmission between devices i and j , when $U_{i,j} = 0$. If there are N (≥ 2) devices, there can exist $\binom{N}{2} = N(N-1)/2$ possible mm Wave links between any two devices as in [19] (with N devices or nodes in a network, the maximum number of concurrent ‘‘active’’ D2D links (or pairs) is $N/2$). However, we consider all the possible link combinations among N devices $\binom{N}{2} = N(N-1)/2$ to check if the network is fully connected). When all of the $N(N-1)/2$ direct D2D links are reliable, we assume that the network is *fully connected* [19], which can be regarded as a fully meshed network [23].

Therefore, the probability to achieve the fully connected network can be represented as

$$P_{\text{FC}} = \frac{\sum_{n=2}^{\infty} \Pr [\text{all } U_{i,j} \text{'s are one} | N = n] \Pr [N = n]}{\Pr [N \geq 2]}, \quad (9)$$

where $1 \leq i, j \leq n$, where $i \neq j$. With the independent link assumption as in [12, 14], the conditional probability in (9) can be simplified as

$$\Pr [\text{all } U_{i,j} \text{'s are one} | N = n] = \left(\mathbb{E} \{ e^{-\beta d_{i,j}} \} \right)^{n(n-1)/2}, \quad (10)$$

where the distance $d_{i,j}$ between devices i and j follows the PDF in (7). Suppose $\mathcal{A} = \mathbb{E}\{e^{-\beta d_{ij}}\}$, which can be calculated by Taylor expansion as follows:

$$\begin{aligned} \mathcal{A} &= \int_0^{2R} e^{-\beta x} f_{d_{i,j}} (x) dx \\ &\approx \left[1 + \frac{\beta^2}{2} \left(R^2 - \left(\frac{128R}{45\pi} \right)^2 \right) \right] \exp \left(-\beta \frac{128R}{45\pi} \right). \end{aligned} \quad (11)$$

Thus, P_{FC} in (9) can be simplified as

$$\begin{aligned} P_{FC} &= \mathbb{E} \left\{ \mathcal{A}^{N(N-1)/2} \mid N \geq 2 \right\} \\ &= \frac{\sum_{n=2}^{\infty} \mathcal{A}^{n(n-1)/2} \cdot \Pr [N = n]}{\Pr [N \geq 2]} \\ &= \frac{\sum_{n=2}^{\infty} \mathcal{A}^{n(n-1)/2} \cdot \left((\lambda\pi R^2)^n / n! \right) e^{-\lambda\pi R^2}}{1 - \exp(-\lambda\pi R^2) (1 + \lambda\pi R^2)}. \end{aligned} \quad (12)$$

3.3. Ratio of Reliable Direct D2D Connections. If the fully connected network cannot be achieved, we can estimate the average number of reliably connected devices through direct D2D communications. If we define a set $T_{\text{dir}} := \{U_{i,j} \mid U_{i,j} = 1\}$, its cardinality $|T_{\text{dir}}|$ is the number of the reliable direct D2D links. Thus, for $N \geq 2$, the ratio of the reliable D2D connections to all of the possible D2D pairs in the network can be derived as

$$\begin{aligned} \gamma_{\text{dir}} &= \frac{1}{\Pr [N \geq 2]} \sum_{n=2}^{\infty} \frac{\mathbb{E} \{ |T_{\text{dir}}| \mid N = n \}}{n(n-1)/2} \Pr [N = n] \\ &= \mathcal{A}, \end{aligned} \quad (13)$$

where $\mathbb{E} \{ |T_{\text{dir}}| \mid N = n \}$ is in fact the mean of binomial distribution $B(n(n-1)/2, p = \mathcal{A})$, which gives $\mathbb{E} \{ |T_{\text{dir}}| \mid N = n \} = \mathcal{A}n(n-1)/2$. As a result, $\gamma_{\text{dir}} = \mathcal{A}$, and it is not a function of the device density λ .

3.4. Impacts of System Parameters. In this section, we consider the impacts of the network size R and the blockage parameter β on P_{FC} and γ_{dir} . The analysis in this section will be verified by comparing with the simulation results in Section 5.

3.4.1. Radius R . To analyze the impact of the network size indicated by R , we first need to investigate the derivative of \mathcal{A} in (11) in terms of R as below:

$$\begin{aligned} \frac{d\mathcal{A}}{dR} &= -\frac{\beta e^{-128\beta R/45\pi}}{91125\pi^3} \left[\left(8\beta \sqrt{2025\pi^2 - 16384R} \right. \right. \\ &\quad \left. \left. + \frac{737280\pi - 91125\pi^3}{16\sqrt{2025\pi^2 - 16384}} \right)^2 259200\pi^2 \right. \\ &\quad \left. - \left(\frac{737280\pi - 91125\pi^3}{16\sqrt{2025\pi^2 - 16384}} \right)^2 \right], \end{aligned} \quad (14)$$

which satisfies $d\mathcal{A}/dR < 0$ for any β and R . Therefore, $\gamma_{\text{dir}} = \mathcal{A}$ is a decreasing function of R . Moreover, we can find that $P_{FC} \rightarrow 0$ as $R \rightarrow \infty$.

3.4.2. Blockage Parameter β . As in the previous section regarding R , we find the derivative of \mathcal{A} in terms of β to investigate the impact of β as

$$\frac{d\mathcal{A}}{d\beta} = -\frac{Re^{-128\beta R/45\pi}}{91125\pi^3} \left[\left(8R \sqrt{2025\pi^2 - 16384\beta} \right. \right.$$

$$\begin{aligned} &\quad \left. + \frac{737280\pi - 91125\pi^3}{16\sqrt{2025\pi^2 - 16384}} \right)^2 259200\pi^2 \\ &\quad - \left(\frac{737280\pi - 91125\pi^3}{16\sqrt{2025\pi^2 - 16384}} \right)^2 \right], \end{aligned} \quad (15)$$

which satisfies $d\mathcal{A}/d\beta < 0$ for any β and R . Therefore, $\gamma_{\text{dir}} = \mathcal{A}$ is a decreasing function of β . Also, when $\beta \rightarrow 0$, $\mathcal{A} \rightarrow 1$. Consequently, $P_{FC} \rightarrow 1$ as $\beta \rightarrow 0$. On the other hand, as $\beta \rightarrow \infty$, $\mathcal{A} \rightarrow 0$, which results in $P_{FC} \rightarrow 0$.

4. Indirect D2D Communications via mm Wave Base Station

In this section, we investigate indirect D2D communications hopping via the mm Wave BS, where it is assumed that direct D2D links are unavailable. If we have an indirect D2D communication pair, two consecutive LoS links “from one device to the mm Wave BS” and “from the mm Wave BS to the other device” are required to be reliable.

4.1. Fully Connected Network via Indirect D2D Communications. For the indirect D2D communication from devices i to j via the BS, both “device i to BS” and “BS to device j ” links should have blockage-free LoS paths. Therefore, to have a fully connected network with $N \geq 2$ hopping over the BS, all the LoS links between the mm Wave BS and N devices should not have blockage. As in the previous section, suppose a Bernoulli random variable W_i is defined as

$$W_i = \begin{cases} 1, & \text{w.p. } P_{\text{LoS},i} = \exp(-\beta r_i), \\ 0, & \text{w.p. } 1 - P_{\text{LoS},i} = 1 - \exp(-\beta r_i), \end{cases} \quad (16)$$

where if $W_i = 1$, the mm Wave communication between the mm Wave BS and device i is successful.

Also, r_i is the distance between the mm Wave BS and device i , which follows the PDF of $f_{r_i}(x) = 2x/R^2$ for $0 \leq x \leq R$. Therefore, the probability to create a fully connected network is given by

$$\begin{aligned} P_{FC} &= \frac{\sum_{n=2}^{\infty} \Pr [\text{all } W_i \text{'s are one} \mid N = n] \Pr [N = n]}{\Pr [N \geq 2]} \\ &= \frac{\sum_{n=2}^{\infty} \left(\mathbb{E} \{ e^{-\beta r_i} \} \right)^n \Pr [N = n]}{\Pr [N \geq 2]}, \end{aligned} \quad (17)$$

where $1 \leq i \leq n$. If $\mathcal{B} = \mathbb{E} \{ e^{-\beta r_i} \}$, it gives

$$\mathcal{B} = \int_0^R e^{-\beta x} f_{r_i}(x) dx = \frac{2}{\beta R^2} \left[\frac{1}{\beta} - \left(R + \frac{1}{\beta} \right) e^{-\beta R} \right]. \quad (18)$$

Hence, P_{FC} is obtained as

$$\begin{aligned}
 P_{FC} &= \frac{\sum_{n=2}^{\infty} \mathcal{B}^n \Pr[N = n]}{\Pr[N \geq 2]} \\
 &= \frac{\sum_{n=2}^{\infty} \frac{\mathcal{B}^n (\lambda \pi R^2)^n \cdot e^{-\lambda \pi R^2}}{\Pr[N \geq 2] \cdot n!}}{\Pr[N \geq 2]} \\
 &= \frac{e^{\mathcal{B} \lambda \pi R^2} - \mathcal{B} \lambda \pi R^2 - 1}{e^{\lambda \pi R^2} - \lambda \pi R^2 - 1}.
 \end{aligned} \tag{19}$$

4.2. Ratio of Reliable Indirect D2D Connections. If we define a set $T_{\text{ind}} := \{W_i \mid W_i = 1\}$, its cardinality $|T_{\text{ind}}|$ is the number of reliable ‘‘device to the mm Wave BS’’ links. Because any devices connected to the mm Wave BS can indirectly communicate with each other, for $|T_{\text{ind}}| \geq 2$, there are $|T_{\text{ind}}|(|T_{\text{ind}}| - 1)/2$ reliable D2D connections. For a given $N = n \geq 2$, $|T_{\text{ind}}|$ follows a binomial distribution $B(n, p = \mathcal{B})$, where \mathcal{B} is derived in (18). Therefore, the ratio of the reliable indirect D2D connections is given by

$$\begin{aligned}
 \gamma_{\text{ind}} &= \frac{1}{\Pr[N \geq 2]} \\
 &\cdot \sum_{n=2}^{\infty} \frac{\mathbb{E}\{|T_{\text{ind}}|(|T_{\text{ind}}| - 1)/2 \mid N = n\} \cdot \Pr[N = n]}{n(n-1)/2} \\
 &= \frac{1}{\Pr[N \geq 2]} \\
 &\cdot \sum_{n=2}^{\infty} \frac{(\mathbb{E}\{|T_{\text{ind}}|^2 \mid N = n\} - \mathbb{E}\{|T_{\text{ind}}| \mid N = n\})/2}{n(n-1)/2} \\
 &\cdot \Pr[N = n] = \frac{1}{\Pr[N \geq 2]} \sum_{n=2}^{\infty} \frac{n^2 \mathcal{B}^2 - n \mathcal{B}^2}{n(n-1)} \\
 &\cdot \Pr[N = n] = \mathcal{B}^2.
 \end{aligned} \tag{20}$$

As γ_{dir} in (13), γ_{ind} is not a function of the device density λ , either.

4.3. Impacts of System Parameters. As in the previous section about the direct D2D communications, we analyze the impacts of R and β on P_{FC} and γ_{dir} .

4.3.1. Radius R . We first consider how \mathcal{B} changes as R varies by considering two extreme cases. For $R \rightarrow 0$ and ∞ , we have

$$\begin{aligned}
 \lim_{R \rightarrow 0} \mathcal{B} &= \lim_{R \rightarrow 0} \frac{1/\beta - e^{-\beta R} (1/\beta + R)}{\beta R} = \frac{\beta}{\beta} = 1, \\
 \lim_{R \rightarrow \infty} \mathcal{B} &= \lim_{R \rightarrow \infty} \frac{2}{\beta^2 R^2} = 0.
 \end{aligned} \tag{21}$$

Thus, $\gamma_{\text{ind}} = \mathcal{B}^2 \rightarrow 1$ as $R \rightarrow 0$. On the other hand, $\gamma_{\text{ind}} = \mathcal{B}^2 \rightarrow 0$ as $R \rightarrow \infty$. Furthermore, $\lim_{R \rightarrow 0} P_{FC} = \lim_{R \rightarrow 0} \mathcal{B}^2 = 1$. In contrast, $P_{FC} \rightarrow 0$ as $R \rightarrow \infty$.

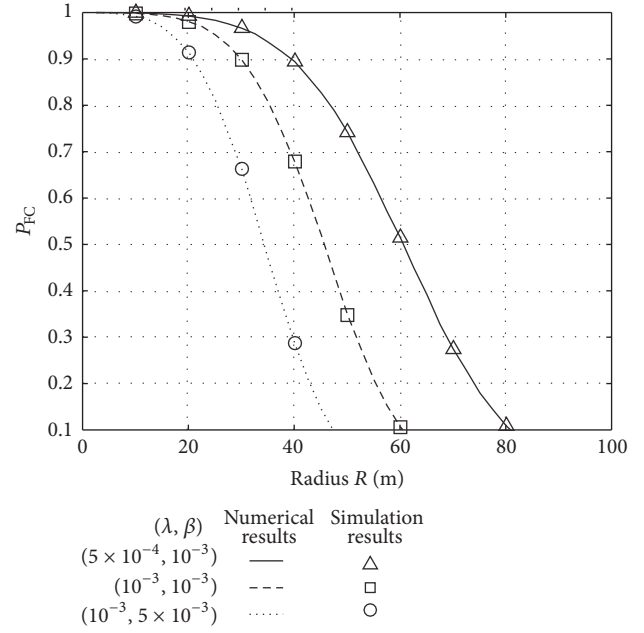


FIGURE 3: Direct D2D: P_{FC} versus R with $\lambda = \{0.001, 0.0005\}$ and $\beta = \{0.001, 0.005\}$.

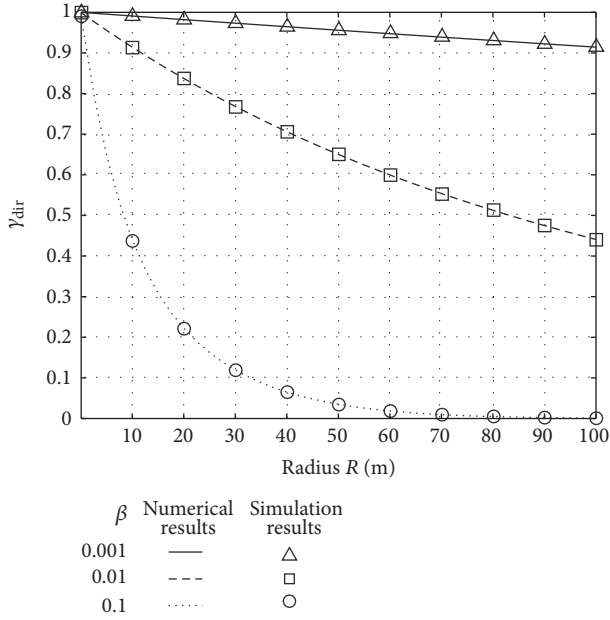
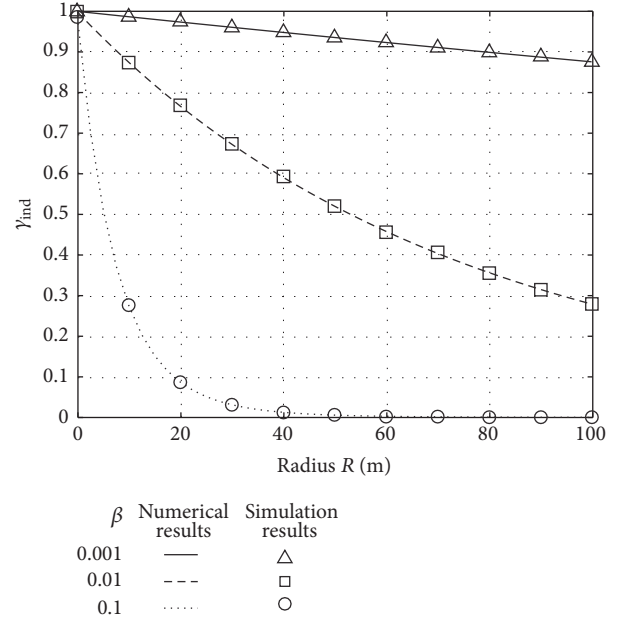
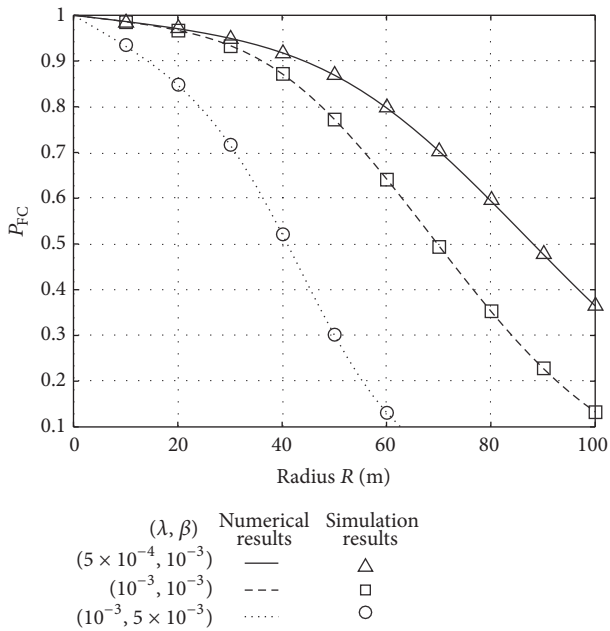
4.3.2. Blockage Parameter β . We can readily find that $\mathcal{B} \rightarrow 1$ and 0, as $\beta \rightarrow 0$ and ∞ , respectively. Therefore, $\gamma_{\text{ind}} = \mathcal{B}^2$ has the same limiting values. Also, it gives $P_{FC} \rightarrow 1$ and 0, as $\beta \rightarrow 0$ and ∞ , respectively.

5. Numerical Results

In this section, we present numerical results of the mm Wave D2D communication systems via both the direct and indirect communications.

5.1. Direct D2D Communications. Figure 3 shows the probability to achieve a fully connected D2D network using the direct D2D communications. The horizontal axis R represents the radius of Area \mathcal{S} in Figure 1(a). The solid, dashed, and dotted lines represent P_{FC} in (12) obtained numerically with different combinations of λ and β . Moreover, the symbols indicate the corresponding Monte Carlo simulation results, which are consistent with the numerical results. All the three graphs decrease, as the radius R increases. Also, comparing the solid and dashed lines ($\lambda = 0.0005$ and 0.001 with the same β), the higher λ gives the lower likelihood of the fully connected network. Similarly, as β increases (the dashed and dotted lines), P_{FC} decreases. In other words, the probability P_{FC} is a decreasing function of both the device density λ and the blockage parameter β .

Figure 4 shows the ratio of the reliable direct D2D connections γ_{dir} in (13). The three curves denoted by the solid, dashed, and dotted lines correspond to $\beta = \{0.001, 0.01, 0.1\}$, respectively. Also, the simulation results indicated by the symbols are in line with the numerical results. As R increases, γ_{dir} decreases. Furthermore, the ratio of the reliable D2D connections decreases, as β increases, because of higher blockage


 FIGURE 4: Direct D2D: $\gamma_{\text{dir}} = \mathcal{A}$ versus R with $\beta = \{0.001, 0.01, 0.1\}$.

 FIGURE 6: Indirect D2D: $\gamma_{\text{ind}} = \mathcal{B}^2$ versus R with $\beta = \{0.001, 0.01, 0.1\}$.

 FIGURE 5: Indirect D2D: P_{FC} versus R with $\lambda = \{0.001, 0.0005\}$ and $\beta = \{0.001, 0.005\}$.

effects. These observations about the system parameters R and β are consistent with our analysis in Section 3.4.

5.2. Indirect D2D Communications. Figure 5 shows the results of P_{FC} for the indirect D2D communications in (19). The three (solid, dashed, and dotted) lines indicate different λ and β combinations, while the symbols represent the corresponding simulation results. As in the direct D2D communication case, the probability P_{FC} decreases, as R

increases. We can observe that P_{FC} is a decreasing function of λ . Also, P_{FC} decreases, as β increases. The same trends can be observed in Figure 6, which is in line with our analysis in Section 4.3.

Compared to the direct communication case, for the same parameters λ , β , and R , P_{FC} is significantly higher with the D2D communication hopping via the mm Wave BS, because the possible distance of the indirect D2D links, that is, $0 \leq r_i \leq R$, is shorter than that of the direct D2D links; that is, $0 \leq d_{i,j} \leq 2R$. Also, for the average separation between two terminals (which are one device and the mm Wave BS for the indirect D2D, but two devices in the direct D2D transmissions), $\mathbb{E}\{d_{i,j}\} \approx 0.91R > \mathbb{E}\{r_i\} \approx 0.67R$, which implies a higher probability of blockage in the direct D2D compared to the indirect D2D communications.

In contrast, when it comes to the average ratios of the reliable D2D connections, γ_{ind} is smaller than γ_{dir} . This can be explained by comparing the exponential terms, which dominate the polynomial terms for large enough β and R , of the two ratios as

$$\gamma_{\text{dir}} = \mathcal{A} \propto \exp\left(-\frac{128}{45\pi}\beta R\right) \approx \exp(-0.9\beta R), \quad (22)$$

$$\gamma_{\text{ind}} = \mathcal{B}^2 \propto [\exp(-\beta R)]^2 \approx \exp(-2\beta R).$$

Therefore, for large enough β and R , $\gamma_{\text{dir}} > \gamma_{\text{ind}}$.

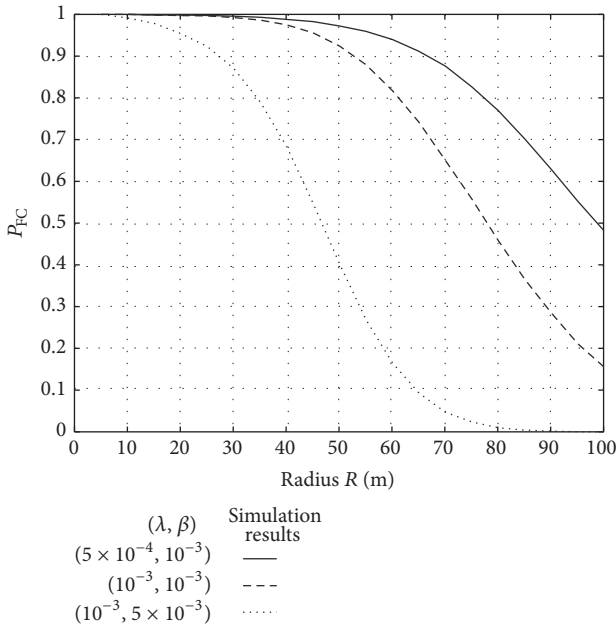
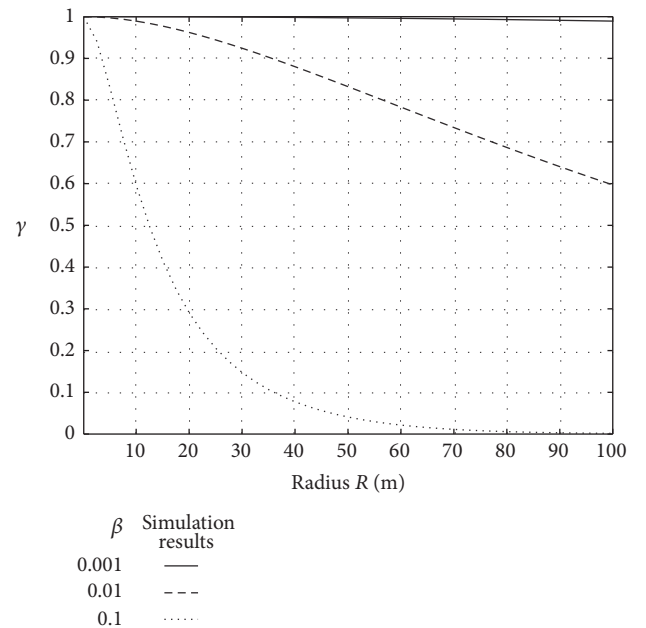
5.3. Hybrid D2D Communications. In this section, we present the D2D connectivity with both the direct and indirect communications jointly exploited. In other words, we consider a hybrid scheme, where all the devices are permitted to use both direct and indirect links to communicate with each other. Therefore, for a D2D pair, we assume their D2D link

TABLE 1: P_{FC} for direct, indirect, and hybrid (direct + indirect) D2D communications.

Parameters (λ, β)	R	P_{FC}			Change (%)
		Direct	Indirect	Hybrid	
(0.0005, 0.001)	10	0.9992	0.9863	1.0000	0.08
	50	0.7417	0.8687	0.9722	11.9
	100	0.0063	0.3646	0.4828	32.4
(0.001, 0.001)	10	0.9983	0.9859	1.0000	0.17
	50	0.3479	0.7715	0.9241	19.8
	100	0.0000	0.1329	0.1563	17.6
(0.001, 0.005)	10	0.9913	0.9315	0.9918	0.05
	50	0.0595	0.2990	0.4026	34.6
	100	0.0000	0.0002	0.0002	—

TABLE 2: γ for direct, indirect, and hybrid (direct + indirect) D2D communications.

Parameters β	R	γ			Change (%)
		Direct	Indirect	Hybrid	
0.001	10	0.9909	0.9866	0.9999	0.09
	50	0.9559	0.9355	0.9972	4.3
	100	0.9143	0.8757	0.9893	8.2
0.01	10	0.9134	0.8745	0.9891	8.3
	50	0.6497	0.5201	0.8319	28.0
	100	0.4408	0.2793	0.5970	35.4
0.1	10	0.4376	0.2759	0.5928	35.5
	50	0.0349	0.0059	0.0406	16.3
	100	0.0012	0.0004	0.0016	33.3

FIGURE 7: Hybrid D2D: P_{FC} versus R with $\lambda = \{0.001, 0.0005\}$ and $\beta = \{0.001, 0.005\}$.FIGURE 8: Hybrid D2D: γ versus R with $\beta = \{0.001, 0.01, 0.1\}$.

is reliable as long as one of the two (direct or indirect links) is reliable.

Table 1 and Figure 7 show P_{FC} with the hybrid (direct + indirect) D2D communications. Also, Table 2 and Figure 8 present the ratio of the reliable D2D connections using the hybrid scheme. In the two tables, the last column indicates the performance improvements in percentage by using the hybrid scheme compared to the nonhybrid case assuming that we pick the one with the better performance between the direct and indirect connections. As shown in the tables and figures, when the two communication links are jointly used, both P_{FC} and γ could be improved significantly. For example, in Table 1, P_{FC} becomes almost one with the small R for the given λ and β . Also, Table 2 shows the increase in γ up to 35.5%.

6. Conclusion

In this paper, we consider D2D communications in mm Wave, where a device can communicate with another device directly or via the mm Wave BS. Assuming uniform distribution of devices according to PPP and the blockage model, we derive the probability of the fully connected network for both direct and indirect communications. Moreover, we analyze the ratio of the reliable D2D connections with the two types of communications. Through analysis and numerical results, we observe that both connectivity performance metrics decrease, as the network size and the blockage parameter increase. Also, the simulation results show that if the hybrid direct and indirect schemes are used, both connectivity performances can be enhanced up to about 35% compared to the nonhybrid case.

Competing Interests

The authors declare that they have no competing interests.

Acknowledgments

This work was supported by the Incheon National University Research Grant in 2016.

References

- [1] C.-X. Wang, F. Haider, X. Gao et al., "Cellular architecture and key technologies for 5G wireless communication networks," *IEEE Communications Magazine*, vol. 52, no. 2, pp. 122–130, 2014.
- [2] T. S. Rappaport, S. Sun, R. Mayzus et al., "Millimeter wave mobile communications for 5G cellular: it will work!," *IEEE Access*, vol. 1, pp. 335–349, 2013.
- [3] F. Boccardi, R. W. Heath, A. Lozano, T. L. Marzetta, and P. Popovski, "Five disruptive technology directions for 5G," *IEEE Communications Magazine*, vol. 52, no. 2, pp. 74–80, 2014.
- [4] 3rd Generation Partnership Project (3GPP), "Technical specification group SA; Feasibility study for proximity services (ProSe) (Release 12)," Tech. Rep. TR 22.803 V1.0.0, 2012.
- [5] IEEE 802.15.8, "Peer-Aware Communications (PAC)," <http://www.ieee802.org/15/pub/TG8.html>.
- [6] K. Doppler, M. Rinne, C. Wijting, C. B. Ribeiro, and K. Hug, "Device-to-device communication as an underlay to LTE-advanced networks," *IEEE Communications Magazine*, vol. 47, no. 12, pp. 42–49, 2009.
- [7] X. Lin, J. G. Andrews, A. Ghosh, and R. Ratasuk, "An overview of 3GPP device-to-device proximity services," *IEEE Communications Magazine*, vol. 52, no. 4, pp. 40–48, 2014.
- [8] J. Qiao, X. S. Shen, J. W. Mark, Q. Shen, Y. He, and L. Lei, "Enabling device-to-device communications in millimeter-wave 5G cellular networks," *IEEE Communications Magazine*, vol. 53, no. 1, pp. 209–215, 2015.
- [9] T. S. Rappaport, F. Gutierrez, E. Ben-Dor, J. N. Murdock, Y. Qiao, and J. I. Tamir, "Broadband millimeter-wave propagation measurements and models using adaptive-beam antennas for outdoor urban cellular communications," *IEEE Transactions on Antennas and Propagation*, vol. 61, no. 4, pp. 1850–1859, 2013.
- [10] S. Rajagopal, S. Abu-Surra, and M. Malmirchegini, "Channel feasibility for outdoor non-line-of-sight mmwave mobile communication," in *Proceedings of the 76th IEEE Vehicular Technology Conference (VTC '12)*, pp. 1–6, September 2012.
- [11] J. G. Andrews, S. Buzzi, W. Choi et al., "What will 5G be?" *IEEE Journal on Selected Areas in Communications*, vol. 32, no. 6, pp. 1065–1082, 2014.
- [12] T. Bai, R. Vaze, and R. W. Heath, "Analysis of blockage effects on urban cellular networks," *IEEE Transactions on Wireless Communications*, vol. 13, no. 9, pp. 5070–5083, 2014.
- [13] D. Stoyan, W. Kendall, and J. Mecke, *Geometry and Its Applications*, John Wiley & Sons, New York, NY, USA, 2nd edition, 1995.
- [14] J. Choi, "On the macro diversity with multiple BSs to mitigate blockage in millimeter-wave communications," *IEEE Communications Letters*, vol. 18, no. 9, pp. 1623–1656, 2014.
- [15] T. Bai and R. W. Heath, "Coverage and rate analysis for millimeter-wave cellular networks," *IEEE Transactions on Wireless Communications*, vol. 14, no. 2, pp. 1100–1114, 2015.
- [16] H. Jung and I.-H. Lee, "Outage analysis of millimeter-wave wireless backhaul in the presence of blockage," *IEEE Communications Letters*, vol. 20, no. 11, pp. 2268–2271, 2016.
- [17] J. G. Andrews, F. Baccelli, and R. K. Ganti, "A tractable approach to coverage and rate in cellular networks," *IEEE Transactions on Communications*, vol. 59, no. 11, pp. 3122–3134, 2011.
- [18] S. Andreev, O. Galinina, A. Pyattaev, K. Johnsson, and Y. Koucheryavy, "Analyzing assisted offloading of cellular user sessions onto D2D links in unlicensed bands," *IEEE Journal on Selected Areas in Communications*, vol. 33, no. 1, pp. 67–80, 2015.
- [19] J. E. Wieselthier, G. D. Nguyen, and A. Ephremides, "On the construction of energy-efficient broadcast and multicast trees in wireless networks," in *Proceedings of the 19th Annual Joint Conference of the IEEE Computer and Communications Societies (IEEE INFOCOM '00)*, vol. 2, pp. 585–594, Tel Aviv, Israel, March 2000.
- [20] P. Billingsley, *Probability and Measure*, John Wiley & Sons, 2012.
- [21] M. Crofton, "Probability," in *Encyclopedia Britannica*, Britannica, 9th edition, 1885.
- [22] D. E. Barton, F. N. David, and E. Fix, "Random points in a circle and the analysis of chromosome patterns," *Biometrika*, vol. 50, no. 1-2, pp. 23–29, 1963.
- [23] Y. Wang, Z. Wang, and L. Zhang, "Internet traffic engineering without full mesh overlaying," in *Proceedings of the 20th Annual Joint Conference on the IEEE Computer and Communications Societies (IEEE INFOCOM '01)*, vol. 1, pp. 565–571, Anchorage, Alaska, USA, April 2001.

Research Article

Joint User Scheduling and MU-MIMO Hybrid Beamforming Algorithm for mmWave FDMA Massive MIMO System

Jing Jiang and Deting Kong

College of Communication and Information Engineering, Xi'an University of Posts and Telecommunications, Xi'an, Shaanxi, China

Correspondence should be addressed to Deting Kong; echo_6480@163.com

Received 2 August 2016; Accepted 9 October 2016

Academic Editor: Hassan T. Chattha

Copyright © 2016 J. Jiang and D. Kong. This is an open access article distributed under the Creative Commons Attribution License, which permits unrestricted use, distribution, and reproduction in any medium, provided the original work is properly cited.

The large bandwidth and multipath in millimeter wave (mmWave) cellular system assure the existence of frequency selective channels; it is necessary that mmWave system remains with frequency division multiple access (FDMA) and user scheduling. But for the hybrid beamforming system, the analog beamforming is implemented by the same phase shifts in the entire frequency band, and the wideband phase shifts may not be harmonious with all users scheduled in frequency resources. This paper proposes a joint user scheduling and multiuser hybrid beamforming algorithm for downlink massive multiple input multiple output (MIMO) orthogonal frequency division multiple access (OFDMA) systems. In the first step of user scheduling, the users with identical optimal beams form an OFDMA user group and multiplex the entire frequency resource. Then base station (BS) allocates the frequency resources for each member of OFDMA user group. An OFDMA user group can be regarded as a virtual user; thus it can support arbitrary MU-MIMO user selection and beamforming algorithms. Further, the analog beamforming vectors employ the best beam of each selected MU-MIMO user and the digital beamforming algorithm is solved by weight MMSE to acquire the best performance gain and mitigate the interuser interference. Simulation results show that hybrid beamforming together with user scheduling can greatly improve the performance of mmWave OFDMA massive MU-MIMO system.

1. Introduction

Millimeter wave (mmWave) communication will unleash the 30–300 GHz new spectrum and enabled gigabit-per-second data rates for the next generation mobile cellular systems [1–3]. Massive MIMO is an essential part of mmWave communication to combat the stringent constraints imposed by the high propagation loss. A beneficial feature of millimeter wave is that large-scale antenna arrays can be packed into small dimensions thanks to the very small wavelength [4, 5]. However, the digital processing in traditional MIMO system requires dedicated baseband and RF hardware for every antenna element. With the large-scale antenna, the high cost and power consumption of mmWave RF hardware preclude such a transceiver architecture at present. In mmWave massive MIMO system, the trade-off between performance and simplicity drives the need to deploy beamforming at both the digital and analog domains, that is, hybrid beamforming.

Most current hybrid beamforming algorithms [6–8] assume user scheduling based on STDMA that a single user

or multiple spatial multiplexing users are scheduled in the entire frequency band at a given time slot. Actually, the large bandwidth and multipath nature of mmWave channels in a cellular system assure the existence of frequency selective channels; it is necessary that mmWave communication remains with frequency division multiple access (FDMA) and user scheduling. OFDMA provides a natural multiple access method by assigning different users with orthogonal subcarriers, and multiuser diversity gain in frequency domain can be exploited by multiuser subcarrier scheduling [9, 10]. But for the hybrid beamforming system, the analog beamforming is implemented by the phase shifts which are constant in the entire frequency band. There are multiple frequency multiplexing users in the entire frequency band; they will experience the same analog beamforming processing. Thus it needs a joint optimization of user scheduling and the wideband processing of the analog beamforming. On the other hand, mmWave links are inherently directional, and the antenna array steers its beam towards any direction electronically and to achieve a high gain at this direction,

while offering a very low gain in all other directions. It is beneficial for MU-MIMO because the RF beams have sufficient degrees of freedom to be optimized for MU-MIMO. In this paper, we will design the joint user scheduling and MU-MIMO hybrid beamforming scheme for mmWave massive MIMO-OFDMA system.

References [11, 12] have meaningful researches on OFDMA scheduling for the hybrid beamforming system. Reference [11] computes the analog beamforming matrix as the first N_a eigenvectors of the left singular value decomposition (SVD) of the combined digital precoding matrices of subcarriers having the highest sum rate (N_a is the amount of RF chains). Then, for fixed \mathbf{A} , the digital beamforming matrix is computed and its corresponding users are scheduled such that the total sum rate is maximized for each subcarrier. Reference [12] enables users with high cochannel interference to be scheduled in different frequency channels in the same time slot while sharing the same RF chain and analog beam.

For MU-MIMO hybrid beamforming algorithms, [13] considers the zero forcing (ZF) hybrid beamforming which essentially applies phase-only control at the RF domain and then performs a low-dimensional baseband ZF precoding based on the effective channel seen from baseband. Reference [14] designs the hybrid beamforming by considering a weighed sum mean-square error (WSMSE) minimization problem incorporating the solution of the detected signals which is obtained from the block diagonalization technique. The resulting WSMSE problem is solved by applying the orthogonal matching pursuit algorithm. Reference [15] analyzes a low complexity hybrid precoding algorithm for downlink multiuser mmWave system, which configures the hybrid precoder at the transmitter and analog combiners at multiple receivers with a small training and feedback overhead. For this algorithm, a lower bound on the achievable rate for the case of single-path channels is derived. Reference [16] designs a hybrid block diagonalization scheme to approach the capacity performance of the traditional BD processing method, aiming to harvest the large array gain through the phase-only RF precoding and combining.

In [11], the analog beamforming matrix is acquired from SVD or QR decomposition, so it is hard to implement with the phase shift of the traditional analog beamforming. Reference [12] considers that the base station applies only one RF chain to transmit signals to users scheduled in different frequency channels. Actually there will be several RF chains in mmWave communication; the scheduled user in multiple subbands could transmit signals from different RF chains. Considering the contradiction between the optimization of the wideband analog beamforming and multiple users scheduled in different frequency subbands, we propose a joint user scheduling and MU-MIMO hybrid beamforming scheme for mmWave OFDMA system. The contribution of this paper can be summarized as follows:

- (i) User scheduling algorithm achieves frequency resource allocation and MU-MIMO user selection. Firstly the users with identical optimal beams are defined as an OFDMA user group. For an OFDMA

user group, all members multiplex the entire frequency band and the one with the best channel gain is assigned in the corresponding frequency resources. Then the frequency domain channel of each OFDMA user group is defined as an integrated channel, which is regarded as a virtual user in MU-MIMO user selection and analog beamforming design. Finally MU-MIMO users are selected to maximize the mmWave system throughput.

- (ii) An OFDMA user group can be regarded as a virtual user that the RF beam of every member is the same; thus the hybrid beamforming could not only coordinate the contradiction of the wideband analog beamforming and multiple users scheduled in frequency resource, but also support arbitrary RF number and MU-MIMO algorithms.
- (iii) For the proposed hybrid beamforming, the analog beamforming vectors adopt the optimal beam of each scheduled user, since the performance of each user is sensitive to beam direction. The digital beamforming algorithm is solved by weight MMSE, which not only achieves the optimal performance for the single user, but also mitigates the residual interuser interference.
- (iv) Evaluate the sum rate of the existing and the proposed MU-MIMO hybrid beamforming under different number of BS antenna and scheduling users. In the simulation, the proposed user scheduling algorithm in this paper is based on FDMA, whereas other reference algorithms are based on TDMA. Simulation results show that hybrid beamforming together with user scheduling can greatly improve the performance of mmWave OFDMA massive MU-MIMO system.

The rest of this paper is organized as follows. Sections 2 and 3 introduce the system model and channel model. In Section 4, the proposed user scheduling algorithm is provided. In Section 5, the proposed hybrid beamforming algorithm is presented, and computer simulation results are shown in Section 6. Finally, conclusions are drawn in Section 7.

Notations. In this paper, upper-case/lower-case boldface letters denote matrices/column vectors. \mathbf{X}^T , \mathbf{X}^H , \mathbf{X}^{-1} , and $\mathbf{X}(i, j)$ denote transpose, conjugate transpose, inversion, and the (i, j) th element of \mathbf{X} , respectively. $[\mathbf{X}]_{mm}$ denotes the m th diagonal element of \mathbf{X} . $\mathbb{E}(\mathbf{X})$ denotes the expected value of \mathbf{X} . $\text{tr}(\mathbf{X})$ denotes the trace of \mathbf{X} . We define $\|\mathbf{X}\|_F^2$ as $\text{tr}(\mathbf{X}^H\mathbf{X})$ and $\|\mathbf{X}\|_2$ as the square root of the maximum eigenvalue of $\mathbf{X}^H\mathbf{X}$. \mathbf{I} is an identity matrix with appropriate size; $\mathbb{C}^{M \times M}$ represent spaces of $M \times M$ matrices with complex entries. The acronyms s.t and i.i.d denote “subject to” and “independent and identically distributed,” respectively.

2. System Model

In this paper, we will consider downlink OFDMA MU-MIMO mmWave system as shown in Figure 1. The BS with N_t transmit antennas communicates N_s data streams to K

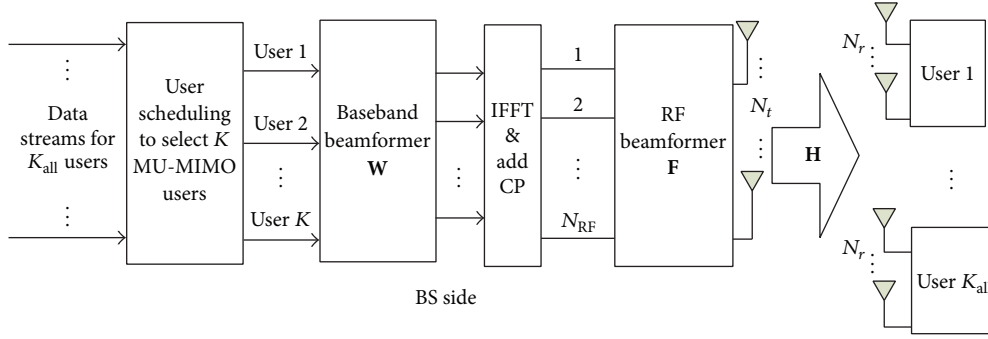


FIGURE 1: Block diagram of mmWave MU-MIMO system based on frequency domain user scheduling.

MU-MIMO spatial multiplexing users, which are selected out from all K_{all} users; every user has N_r antennas. To enable multistream communication, the transmitter is equipped with N_{RF} transmit chains such that $N_s \leq N_{\text{RF}} \leq N_t$. We employ resource block based OFDMA transmission where each block occupies N_f adjacent subcarriers and N_o consecutive OFDM symbols. At each time slot of duration T , the transmitter broadcasts N_b blocks and N_b is the amount of resource blocks [17, 18].

The transmitted data streams at the BS are assumed to be processed by a digital beamformer \mathbf{W} in the baseband, followed by an analog beamformer \mathbf{F} before transmission. Notably, \mathbf{F} can realize only phase changes (phase-only control), since it is implemented using analog phase shifters; each entry of \mathbf{F} is constrained to satisfying $\|\mathbf{F}_{i,j}\| = 1/\sqrt{N_t}$. Furthermore, the total power constraint is enforced by letting $\|\mathbf{F}\mathbf{W}\|_F^2 = N_s$. For simplicity, we will describe the system model in frequency domain. Analog beamforming vector \mathbf{f} in time domain will be transformed to \mathbf{F} in frequency domain just by employing fast Fourier transform (FFT) operation. At the MS, a digital combiner \mathbf{B} is used to process the received signal.

Assume the transmitted signals of different users are independent from each other and from noises, the received signal $\mathbf{Y}_{n,k} \in \mathbb{C}^{N_r \times 1}$ of the k th user scheduled in the n th block can be written as

$$\mathbf{Y}_{n,k} = \mathbf{B}_{n,k}^H \mathbf{H}_{n,k} \mathbf{F} \mathbf{W}_{n,k} \mathbf{s}_{n,k} + \sum_{j=1, j \neq k}^K \mathbf{B}_{n,k}^H \mathbf{H}_{n,k} \mathbf{F} \mathbf{W}_{n,j} \mathbf{s}_{n,j} + \mathbf{B}_{n,k}^H \mathbf{n}_{n,k}, \quad (1)$$

where $\mathbf{s}_{n,k} \in \mathbb{C}^{N_s^{n,k} \times 1}$ denotes the transmitted signal vector for k th user in the n th block, satisfying $\mathbb{E}[\mathbf{s}_{n,k}^H \mathbf{s}_{n,k}] = \mathbf{I}$, $\mathbb{E}[\mathbf{s}_{n,k}^H \mathbf{s}_{n,j}] = 0$, ($k \neq j$), $\mathbb{E}[\mathbf{s}_{n,k}^H \mathbf{n}_{n,k}] = 0$, and $N_s^{n,k}$ represents the number of the k th user's data streams scheduled in the n th block. $\mathbf{W}_{n,k} \in \mathbb{C}^{N_{\text{RF}} \times N_s^{n,k}}$ denotes the transmitting digital beamformer for the k th user in the n th block, and $\mathbf{F} \in \mathbb{C}^{N_t \times N_{\text{RF}}}$ denotes the transmitting analog beamformer in the frequency domain which is FFT transformed by time domain \mathbf{f} , $\mathbf{f} = [\mathbf{f}_1, \mathbf{f}_2, \dots, \mathbf{f}_{N_{\text{RF}}}]$. $\mathbf{B}_{n,k} \in \mathbb{C}^{N_r \times N_s^{n,k}}$ denotes linear receive beamforming vectors to detect the transmit signals. $\mathbf{H}_{n,k} \in \mathbb{C}^{N_r \times N_t}$ denotes the MIMO channel of the k th user. $\mathbf{n}_{n,k}$ is

the vector of i.i.d additive complex Gaussian noise with zero-mean and variance σ^2 .

3. Channel Model

Since mmWave channels are expected to have limited scattering, we adopt a geometric channel model with L_k rays for the channel of user k in block n . Under this model, the channel $\mathbf{H}_{n,k}$ can be expressed as [12, 13]

$$\mathbf{H}_{n,k} = \sqrt{\frac{N_r N_t}{L_s \rho_k}} \sum_{l=1}^{L_s} \mathbf{a}_R(\varphi_l^R, \theta_l^R) \beta_l \mathbf{a}_T^T(\varphi_l^T, \theta_l^T), \quad (2)$$

where β_l is the channel impulse response of the l th path with $\mathbb{E}[|\beta_l|^2] = 1$ and ρ_k is the path loss between BS and users. Considering the azimuth and elevation angles, the vectors $\mathbf{a}_T(\varphi_l^T, \theta_l^T)$ and $\mathbf{a}_R(\varphi_l^R, \theta_l^R)$ represent the normalized transmit and receive array response vectors at an azimuth (elevation) angle of departure φ_l^T (θ_l^T) and that of arrival φ_l^R (θ_l^R), respectively.

For a uniform planar array (UPA) in the xy -plane with N_{row} and N_{col} elements on the x - and y -axes, respectively, the array response vector at the BS is given by [19]

$$\begin{aligned} \mathbf{a}_T(\varphi_l^T, \theta_l^T) &= \text{vec}(\mathbf{a}_{N_{\text{row}}}(\mu) \mathbf{a}_{N_{\text{col}}}^T(\nu)) \\ &= \frac{1}{\sqrt{N_{\text{row}} N_{\text{col}}}} \left[1, e^{j\nu}, \dots, e^{j(N_{\text{col}}-1)\nu}, e^{j(\mu+\nu)}, \dots, \right. \\ &\quad \left. e^{j(\mu+(N_{\text{col}}-1)\nu)}, \dots, e^{j(N_{\text{row}}-1)\mu}, \dots, e^{j(N_{\text{row}}-1)\mu+(N_{\text{col}}-1)\nu} \right]^T, \end{aligned} \quad (3)$$

$\mu = 2\pi d_x \cos \varphi \sin \theta / \lambda$, $\nu = 2\pi d_y \sin \varphi \sin \theta / \lambda$, where λ is the wavelength and d_x and d_y are the distances between two adjacent antenna elements in the x - and y -axes, respectively. $\text{vec}(\cdot)$ denotes the matrix of dimension $N_{\text{row}} \times N_{\text{col}}$ stretches to the column vector of dimension $N_t \times 1$. The antenna array at the user side utilizes a uniform linear array (ULA); thus array response vectors at the user side are given by

$$\begin{aligned} \mathbf{a}_R(\theta_l^R) \\ &= \frac{1}{\sqrt{N_r}} \left[1, e^{j(2\pi/\lambda)d \sin(\theta)}, \dots, e^{j(N_r-1)(2\pi/\lambda)d \sin(\theta)} \right]^T, \end{aligned} \quad (4)$$

where $\mathbf{a}_R(\theta_l^R)$ is the column vector of dimension $N_r \times 1$.

4. User Scheduling Scheme

This section discusses the proposed user scheduling algorithm and MU-MIMO user selection to maximize the total sum rate of all subcarriers, which can be treated as a stage prior to the hybrid beamforming design. This section is divided into three subsections. In the first subsection, we define OFDMA user groups that the users in a same group have identical RF beam and multiplex the whole frequency resource. In the second subsection, we allocate the frequency resource for each member and define each OFDMA group as a virtual user. In the last subsection, we select several MU-MIMO users which can maximize the mmWave system throughput.

4.1. OFDMA Group Selection. Firstly, users transmit uplink sounding signals, and BS uses the sounding results to select the strongest beam for every downlink user. According to the indices of the selected beams, the users which have identical selected beam form an OFDMA user group. OFDMA group selection problem is mathematically formulated as follows:

$$\begin{aligned} & \text{User}_i, \text{User}_j \in \Omega_{\text{OFDMA}}^l \\ \text{s.t. } & f_{\text{User}_i}^{\text{opt}} = f_{\text{User}_j}^{\text{opt}}, \end{aligned} \quad (5)$$

where Ω_{OFDMA}^l denotes the l th OFDMA user group and $f_{\text{User}_i}^{\text{opt}}$ denotes the strongest beam index of user i . OFDMA group set contains L OFDMA user groups defined as $\Omega_{\text{OFDMA}} = \{\Omega_{\text{OFDMA}}^1, \dots, \Omega_{\text{OFDMA}}^L\}$.

4.2. Frequency Resources Allocation. The users in the same group will multiplex the entire frequency band. BS allocates the frequency resources for every member of OFDMA user group. To maximize the throughput of OFDMA system, the subcarrier or resource block is allocated to the user with the best channel gain. The scheduling process of the n th user in OFDMA user group Ω_{OFDMA}^l is defined as

$$\begin{aligned} \text{User}_i^n &= \max_{\text{User}_i \in \Omega_{\text{OFDMA}}^l} (\text{SNR}_{n,i}) \\ &= \max_{\text{User}_i \in \Omega_{\text{OFDMA}}^l} \left(\frac{\|\mathbf{H}_{n,i}\|^2}{\sigma^2} \right), \end{aligned} \quad (6)$$

where $\text{SNR}_{n,i}$ is the signal noise ratio for user i in the n th block.

After the frequency resource scheduling, the users in this group are sorted as follows:

$$\Omega_{\text{OFDMA}}^l = \{\text{User}_i^1, \dots, \text{User}_i^{N_b}\}. \quad (7)$$

For the l th OFDMA user group Ω_{OFDMA}^l , the frequency channels of all members are merged into an integrated channel which represents the spatial characters of the users multiplexed in different frequency resources. The integrated channel of OFDMA user group Ω_{OFDMA}^l is defined as

$$\bar{\mathbf{H}}_l = [\mathbf{H}_l^1 | \mathbf{H}_l^2 | \dots | \mathbf{H}_l^{N_b}]_{N_s \times N_t}, \quad (8)$$

where \mathbf{H}_l^n represents the channel of the user scheduled in the n th resource block for the l th OFDMA user group and so on.

4.3. MU-MIMO User Selection. Every integrated channel associated with an OFDMA user group is regarded as a virtual user. The virtual users and other users to be scheduled constitute the candidate user set Ω_C . Specially, MU-MIMO channels of all spatial multiplexing users are defined as $\bar{\mathbf{H}}_1, \dots, \bar{\mathbf{H}}_K$. For OFDMA user group, $\bar{\mathbf{H}}_i$ is the integrated channel associated with this OFDMA user group. For other users which independently occupy the entire frequency resource, $\bar{\mathbf{H}}_j$ is the channel of the j th MU-MIMO user.

This section discusses the proposed MU-MIMO user selection to maximize the total sum rate. The detailed solution can be given by two steps.

Firstly, to decrease the complexity of searching MU-MIMO user, the user with best channel gain is given a high priority in MU-MIMO user selection. Thus, the user with the maximum SNR is selected as the leader of MU-MIMO user selection. The leader is formulated as

$$\text{Leader} = \max_{\text{User}_i \in \Omega_C} (\text{SNR}_i) = \max_{\text{User}_i \in \Omega_C} \left(\frac{\|\bar{\mathbf{H}}_i\|^2}{\sigma^2} \right), \quad (9)$$

where $\bar{\mathbf{H}}_i$ is the equivalent channel considering beamforming gains. As is known, an upper bound on the performance of hybrid beamforming approximates to that of full digital beamforming for any design criteria [14], and SVD is a typical beamforming method in numerous beamforming algorithms. Thus we utilize SVD as full digital beamforming weighting vectors when calculating SNR of the target user [20, 21]. The MIMO channel of the i th user $\bar{\mathbf{H}}_i$ can be decomposed by SVD as $\bar{\mathbf{H}}_i = \mathbf{U}_i \Lambda_i \mathbf{V}_i^H$ and the equivalent channel $\tilde{\mathbf{H}}_i$ is defined as $\tilde{\mathbf{H}}_i = \mathbf{U}_i^H \bar{\mathbf{H}}_i \mathbf{V}_i$.

At the second step, the objective function of the other MU-MIMO user selection is defined as follows:

$$\max_{\text{User}_k \in \Omega_S} R_{\text{sum}}^k, \quad (10)$$

where R_{sum}^k is the sum rate when user k is scheduled as expressed in (11).

$$\begin{aligned} R_{\text{sum}}^k &= \log_2 \left(1 + \frac{\|\mathbf{U}_k^H \bar{\mathbf{H}}_k \mathbf{V}_k\|^2}{\sum_{j \in \Omega_S, k \in \Omega_C} \|\mathbf{U}_j^H \bar{\mathbf{H}}_j \mathbf{V}_j\|^2 + \sigma^2} \right. \\ &\quad \left. + \sum_{j \in \Omega_S} \frac{\|\mathbf{U}_j^H \bar{\mathbf{H}}_j \mathbf{V}_j\|^2}{\sum_{i \in \Omega_S, i \neq j} \|\mathbf{U}_i^H \bar{\mathbf{H}}_i \mathbf{V}_i\|^2 + \|\mathbf{U}_k^H \bar{\mathbf{H}}_k \mathbf{V}_k\|^2 + \sigma^2} \right). \end{aligned} \quad (11)$$

The MU-MIMO user selection process continues until iterating $K - 1$ times with employing exhaustive search and composes the selected user set Ω_S , $\Omega_S = \{\Omega_S^1, \dots, \Omega_S^K\}$, $K \leq N_{\text{RF}}$. Note that the maximum number of multiplexed multiusers is equal to the number of RF links.

Outline of user scheduling algorithm is described as shown in Algorithm 1.

Initialization: OFDMA group set $\Omega_{\text{OFDMA}} = \Phi$, the candidate user set $\Omega_C = \Phi$, the selected user set $\Omega_S = \Phi$

Step 1. Select the users with same optimal beams to form OFDMA group set Ω_{OFDMA} .

$$\begin{aligned} & \text{User}_i, \text{User}_j \in \Omega_{\text{OFDMA}}^l \\ \text{s.t. } & f_{\text{User}_i}^{\text{opt}} = f_{\text{User}_j}^{\text{opt}} \\ & l = 1, \dots, L \end{aligned}$$

$$\Omega_{\text{OFDMA}} = \Omega_{\text{OFDMA}}^1, \dots, \Omega_{\text{OFDMA}}^L$$

Step 2. BS allocates the corresponding frequency resource to the user with the best channel gain for each OFDMA user group.

Then the frequency channels of all members of OFDMA user group Ω_{OFDMA}^l are merged into the integrated channel $\bar{\mathbf{H}}_l$

Loop 1: $l = 1, \dots, L$

Loop 2: $n = 1, \dots, N_b$

$$\text{User}_l^n = \max_{\text{User}_i \in \Omega_{\text{OFDMA}}^l} (\text{SNR}_{n,i}) = \max_{\text{User}_i \in \Omega_{\text{OFDMA}}^l} \left(\frac{\|\mathbf{H}_{n,i}\|^2}{\sigma^2} \right)$$

End Loop 2

$$\bar{\mathbf{H}}_l = [\mathbf{H}_l^1 | \mathbf{H}_l^2 | \dots | \mathbf{H}_l^{N_b}]$$

End Loop 1

Step 3. The candidate user set Ω_C consists of virtual users and other users to be scheduled. Select the user with the maximum SNR as the leader from Ω_C .

$$\text{Leader} = \max_{\text{User}_i \in \Omega_C} (\text{SNR}_i) = \max_{\text{User}_i \in \Omega_C} \left(\frac{\|\bar{\mathbf{H}}_i\|^2}{\sigma^2} \right)$$

Step 4. Select the other MU-MIMO spatial multiplexing users with employing exhaustive search that can achieve the maximal sum rate of the system.

$$\max_{\text{User}_k \in \Omega_S} R_{\text{sum}}^k$$

Repeat Step 4 until selecting $K - 1$ spatial multiplexing users.

Finally obtain the selected user set Ω_S , $\Omega_S = \{\Omega_S^1, \dots, \Omega_S^K\}$.

ALGORITHM 1: User scheduling scheme.

5. Hybrid Beamforming Designs in Massive MIMO Systems

In this section, we design a hybrid beamforming algorithm for mmWave OFDMA massive MIMO system as illustrated in Figure 1. For the hybrid beamforming system, the analog beamforming is implemented by the phase shifts which are constant in the entire frequency domain. Considering the contradiction between the optimization of wideband analog beamforming and multiple users scheduled in OFDMA system, an effective solution is that every user or virtual user of MU-MIMO selected user set maps its own transmitting signals to a unique RF chain. That is, the analog beamforming vector for a RF chain will be optimized based on the channel character of only one user or the virtual user with same optimal beam. Because the integrated channel can be treated as a virtual user with similar optimal beam in the entire frequency band, the hybrid beamforming could not only reconcile the contradiction of the wideband analog beamforming and multiple users scheduled in frequency resource, but also support arbitrary user scheduling band and MU-MIMO algorithms.

In what follows, we split the proposed hybrid beamforming design into two steps: Firstly, for analog beamforming design, we adopt the optimal beam of each scheduled user. Then, we focus on digital beamforming design. The digital beamforming algorithm not only achieves the optimal

beamforming gains for every user allocated in its own block, but also mitigates the interuser interference in the same block. Further, the digital beamforming is formulated by the weighted MMSE.

5.1. Analog Beamformer Design. Firstly, MU-MIMO channel matrix $\bar{\mathbf{H}}$ in frequency domain is transformed to time domain $\bar{\mathbf{h}}$ just by employing inverse fast Fourier transform (IFFT); that is $\bar{\mathbf{h}}_1, \dots, \bar{\mathbf{h}}_K = \text{ifft}[\bar{\mathbf{H}}_1, \dots, \bar{\mathbf{H}}_K]$.

Consider the analog beamformer design, the achievable rate is $R_{\text{sum}} = \log_2(1 + \|\bar{\mathbf{h}}_l \mathbf{f}_l\|^2 / \sigma^2)$ for l th MU-MIMO user and we seek to design the analog beamformer \mathbf{f}_l to maximize sum rate by scanning a codebook \mathcal{F}_t [22], which can be expressed as

$$\max_{\mathbf{f}_l \in \mathcal{F}_t} R_{\text{sum}} = \max_{\mathbf{f}_l \in \mathcal{F}_t} \log_2 \left(1 + \frac{\|\bar{\mathbf{h}}_l \mathbf{f}_l\|^2}{\sigma^2} \right). \quad (12)$$

Since every RF chain corresponds to one MU-MIMO user, then $\mathbf{f} = [\mathbf{f}_1, \mathbf{f}_2, \dots, \mathbf{f}_{N_{\text{RF}}}]$ is the selected time domain beam vectors from the predefined RF beamforming codebook \mathcal{F}_t . \mathcal{F}_t is specified in a quantized matrix $\mathbf{a}_T(2\pi i_\varphi / M_\varphi, 2\pi j_\theta / M_\theta)$, where each column is a weight vector corresponding to one beam pattern, for the variable i_φ taking the values $0, 1, 2, \dots, M_\varphi - 1$ and j_θ taking the values $0, 1, 2, \dots, M_\theta - 1$,

and M_φ and M_θ denote the quantized precision of azimuth and elevation angles, respectively.

Note that the objective function of MU-MIMO user selection is similar to that of analog beamforming. The difference is that only MU-MIMO user selection considers the interuser interference. An enormous amount of simulation results indicates that the analog beamforming performance obviously decreases while the optimal beam direction of the target user is slightly changed. Thus for the analog beamforming, we still apply the optimal beam for each selected user. The interuser interference can be further mitigated by the digital beamforming.

5.2. Digital Beamformer Design. In this stage, we design the digital beamformer by the weighted MMSE approach [23, 24] to mitigate multiuser mutual interference. Assume $\mathbf{g}_{n,k} \geq 0$ be a weight matrix for user k , and the weighted sum-MSE minimization used to deal with the problem is formulated as

$$\begin{aligned} \min_{\mathbf{g}, \mathbf{W}, \mathbf{B}} \quad & \sum_{n=1}^{N_b} \sum_{k=1}^K \text{tr}(\mathbf{g}_{n,k} \xi_{n,k}) - \log \det(\mathbf{g}_{n,k}) \\ \text{s.t.} \quad & \sum_{n=1}^{N_b} \sum_{k=1}^K \text{tr}(\mathbf{F} \mathbf{W}_{n,k} \mathbf{W}_{n,k}^H \mathbf{F}^H) = P, \end{aligned} \quad (13)$$

where P denotes the power budget, and the mean-square estimation error matrix $\xi_{n,k}$ can be written as

$$\begin{aligned} \xi_{n,k} &= \mathbb{E} \left[(\mathbf{Y}_{n,k} - \mathbf{s}_{n,k})(\mathbf{Y}_{n,k} - \mathbf{s}_{n,k})^H \right] \\ &= \mathbb{E} \left[\left(\mathbf{B}_{n,k}^H \mathbf{H}_{n,k} \mathbf{F} \mathbf{W}_{n,k} \mathbf{s}_{n,k} \right. \right. \\ &\quad \left. \left. + \sum_{j=1, j \neq k}^K \mathbf{B}_{n,k}^H \mathbf{H}_{n,k} \mathbf{F} \mathbf{W}_{n,j} \mathbf{s}_{n,j} + \mathbf{B}_{n,k}^H \mathbf{n}_{n,k} - \mathbf{s}_{n,k} \right) \right. \\ &\quad \left. \times \left(\mathbf{B}_{n,k}^H \mathbf{H}_{n,k} \mathbf{F} \mathbf{W}_{n,k} \mathbf{s}_{n,k} + \sum_{j=1, j \neq k}^K \mathbf{B}_{n,k}^H \mathbf{H}_{n,k} \mathbf{F} \mathbf{W}_{n,j} \mathbf{s}_{n,j} \right. \right. \\ &\quad \left. \left. + \mathbf{B}_{n,k}^H \mathbf{n}_{n,k} - \mathbf{s}_{n,k} \right)^H \right] = (\mathbf{I} - \mathbf{B}_{n,k}^H \mathbf{H}_{n,k} \mathbf{F} \mathbf{W}_{n,k}) (\mathbf{I} \\ &\quad - \mathbf{B}_{n,k}^H \mathbf{H}_{n,k} \mathbf{F} \mathbf{W}_{n,k})^H \\ &\quad + \sum_{j=1, j \neq k}^K \mathbf{B}_{n,k}^H \mathbf{H}_{n,k} \mathbf{F} \mathbf{W}_{n,j} \mathbf{W}_{n,j}^H \mathbf{F}^H \mathbf{H}_{n,k}^H \mathbf{B}_{n,k} \\ &\quad + \sigma^2 \mathbf{B}_{n,k}^H \mathbf{B}_{n,k}. \end{aligned} \quad (14)$$

It follows

$$\begin{aligned} \bar{\xi}_{n,k} &= \text{tr} \{ \xi_{n,k} \} \\ &= \sum_{j=1}^K \mathbf{H}_{n,k} \mathbf{F} \mathbf{W}_{n,j} \mathbf{W}_{n,j}^H \mathbf{F}^H \mathbf{H}_{n,k}^H \text{tr}(\mathbf{B}_{n,k}^H \mathbf{B}_{n,k}) \\ &\quad - \text{tr}(\mathbf{B}_{n,k}^H) \mathbf{H}_{n,k} \mathbf{F} \mathbf{W}_{n,k} - \mathbf{W}_{n,k}^H \mathbf{F}^H \mathbf{H}_{n,k}^H \text{tr}(\mathbf{B}_{n,k}) \\ &\quad + \sigma^2 \text{tr}(\mathbf{B}_{n,k}^H \mathbf{B}_{n,k}). \end{aligned} \quad (15)$$

For fixed all $\mathbf{W}_{n,k}$, MMSE receive beamforming $\mathbf{B}_{n,k}$ at user k is given as

$$\begin{aligned} \mathbf{B}_{n,k}^{\text{mmse}} &= \frac{\mathbf{H}_{n,k} \mathbf{F} \mathbf{W}_{n,k}}{\sum_{n=1}^{N_b} \sum_{j=1}^K \mathbf{H}_{n,k} \mathbf{F} \mathbf{W}_{n,j} \mathbf{W}_{n,j}^H \mathbf{F}^H \mathbf{H}_{n,k}^H + \sigma^2 \mathbf{I}} \\ &= \mathbf{J}_{n,k}^{-1} \mathbf{H}_{n,k} \mathbf{F} \mathbf{W}_{n,k}. \end{aligned} \quad (16)$$

Let $\mathbf{J}_{n,k}^{-1} = \sum_{n=1}^{N_b} \sum_{j=1}^K \mathbf{H}_{n,k} \mathbf{F} \mathbf{W}_{n,j} \mathbf{W}_{n,j}^H \mathbf{F}^H \mathbf{H}_{n,k}^H + \sigma^2 \mathbf{I}$. Then, the corresponding MSE error matrix for user k applying the receive beamforming $\mathbf{B}_{n,k}^{\text{mmse}}$ can be written as

$$\xi_{n,k}^{\text{mmse}} = \mathbf{I} - \mathbf{W}_{n,k}^H \mathbf{F}^H \mathbf{H}_{n,k}^H \mathbf{J}_{n,k}^{-1} \mathbf{H}_{n,k} \mathbf{F} \mathbf{W}_{n,k}. \quad (17)$$

Because the object function of (13) is convex in each of the optimization variables $\mathbf{g}, \mathbf{W}, \mathbf{B}$, the block coordinate descent method is adopted to solve (13). Specifically, the weighted sum-MSE object function is minimized by sequentially fixing two of the three variables $\mathbf{g}, \mathbf{W}, \mathbf{B}$ and updating the third variable. While the update of receiver beamforming $\mathbf{B}_{n,k}$ is expressed by (16), the update of the weight variable $\mathbf{g}_{n,k}$ is in closed form that can be written as

$$\mathbf{g}_{n,k}^{\text{opt}} = \xi_{n,k}^{-1}. \quad (18)$$

The update of transmit digital beamforming $\mathbf{W}_{n,k}$ can also be decoupled through transmitters, causing the following optimization problem:

$$\begin{aligned} \min \quad & \sum_{k=1}^K \text{tr}(\mathbf{g}_{n,k} (\mathbf{I} - \mathbf{B}_{n,k}^H \mathbf{H}_{n,k} \mathbf{F} \mathbf{W}_{n,k}) (\mathbf{I} - \mathbf{B}_{n,k}^H \mathbf{H}_{n,k} \mathbf{F} \mathbf{W}_{n,k})^H) \\ & + \sum_{k=1}^K \text{tr} \left(\sum_{j \neq k} \mathbf{g}_{n,k} \mathbf{B}_{n,k}^H \mathbf{H}_{n,k} \mathbf{F} \mathbf{W}_{n,j} \mathbf{W}_{n,j}^H \mathbf{F}^H \mathbf{H}_{n,k}^H \mathbf{B}_{n,k} \right) \\ \text{s.t.} \quad & \sum_{k=1}^K \text{tr}(\mathbf{F} \mathbf{W}_{n,k} \mathbf{W}_{n,k}^H \mathbf{F}^H) \leq P. \end{aligned} \quad (19)$$

We can exploit standard convex optimization approaches to solve this convex quadratic optimization problem. Meanwhile, we can also apply the Lagrange multipliers method to get a closed form solution. In particular, assuming a

Input: Multi-user frequency channels $\mathbf{H}_1, \mathbf{H}_2, \dots, \mathbf{H}_K$, analog beamforming \mathbf{F} , and power constraint $P > 0$
Initialization: $\mathbf{W}_{n,k}$ such that $\text{tr}(\mathbf{F}\mathbf{W}_{n,k}\mathbf{W}_{n,k}^H\mathbf{F}^H) = P/K$
For $n = 1, 2, \dots, N_b$
 While $|\sum_{k=1}^K \log \det \bar{\mathbf{g}}_{n,k} - \sum_{k=1}^K \log \det \mathbf{g}_{n,k}| \geq \zeta$
 $\bar{\mathbf{g}}_{n,k} = \mathbf{g}_{n,k}$
 Update $\mathbf{B}_{n,k} = \mathbf{H}_{n,k}\mathbf{F}\mathbf{W}_{n,k}/(\sum_{n=1}^{N_b} \sum_{j=1}^K \mathbf{H}_{n,k}\mathbf{F}\mathbf{W}_{n,j}\mathbf{W}_{n,j}^H\mathbf{F}^H\mathbf{H}_{n,k}^H + \sigma^2\mathbf{I})$,
 $k \in K$
 $\mathbf{g}_{n,k} = (\mathbf{I} - \mathbf{B}_{n,k}^H\mathbf{H}_{n,k}\mathbf{F}\mathbf{W}_{n,k})^{-1}$.
 $\mathbf{W}_{n,k} = \left(\sum_{j=1}^K \mathbf{F}^H\mathbf{H}_{n,k}^H\mathbf{B}_{n,j}\mathbf{g}_{n,j}\mathbf{B}_{n,j}^H\mathbf{H}_{n,k}\mathbf{F} + \lambda_k\mathbf{F}^H\mathbf{F} \right)^{-1} \mathbf{F}^H\mathbf{H}_{n,k}^H\mathbf{B}_{n,k}\mathbf{g}_{n,k}$
 End While
End For

ALGORITHM 2: Weighted MMSE approach.

Lagrange multiplier $\lambda_k \geq 0$ to the power budget constraint of transmitter, the Lagrange function is given by

$$f(\{\mathbf{W}_{n,k}\}_{k=1}^K, \lambda_k) = \sum_{k=1}^K \text{tr} \left(\mathbf{g}_{n,k} (\mathbf{I} - \mathbf{B}_{n,k}^H\mathbf{H}_{n,k}\mathbf{F}\mathbf{W}_{n,k}) \cdot (\mathbf{I} - \mathbf{B}_{n,k}^H\mathbf{H}_{n,k}\mathbf{F}\mathbf{W}_{n,k})^H \right) + \sum_{k=1}^K \text{tr} \left(\sum_{j \neq k} \mathbf{g}_{n,k}\mathbf{B}_{n,k}^H\mathbf{H}_{n,k}\mathbf{F}\mathbf{W}_{n,j}\mathbf{W}_{n,j}^H\mathbf{F}^H\mathbf{H}_{n,k}^H\mathbf{B}_{n,k} \right) + \lambda_k \left(\sum_{k=1}^K \text{tr}(\mathbf{F}\mathbf{W}_{n,k}\mathbf{W}_{n,k}^H\mathbf{F}^H) - P \right). \quad (20)$$

$\partial f(\{\mathbf{W}_{n,k}\}_{k=1}^K, \lambda_k)/\partial \mathbf{W}_{n,k} = 0$ and then the first-order optimality condition of $f(\{\mathbf{W}_{n,k}\}_{k=1}^K, \lambda_k)$ in regard to each $\mathbf{W}_{n,k}$ yields

$$\mathbf{W}_{n,k}^{\text{opt}} = \left(\sum_{j=1}^K \mathbf{F}^H\mathbf{H}_{n,k}^H\mathbf{B}_{n,j}\mathbf{g}_{n,j}\mathbf{B}_{n,j}^H\mathbf{H}_{n,k}\mathbf{F} + \lambda_k\mathbf{F}^H\mathbf{F} \right)^{-1} \cdot \mathbf{F}^H\mathbf{H}_{n,k}^H\mathbf{B}_{n,k}\mathbf{g}_{n,k}. \quad (21)$$

Let $\mathbf{W}_{n,k}(\lambda_k)$ be the right-hand side of (21). When the matrix $\sum_{j=1}^K \mathbf{F}^H\mathbf{H}_{n,k}^H\mathbf{B}_{n,j}\mathbf{g}_{n,j}\mathbf{B}_{n,j}^H\mathbf{H}_{n,k}\mathbf{F} + \lambda_k\mathbf{F}^H\mathbf{F}$ is invertible and $\sum_{k=1}^K \text{tr}(\mathbf{F}\mathbf{W}_{n,k}(0)\mathbf{W}_{n,k}^H(0)\mathbf{F}^H) \leq P$, then $\mathbf{W}_{n,k}^{\text{opt}} = \mathbf{W}_{n,k}(0)$; otherwise we must have

$$\sum_{k=1}^K \text{tr}(\mathbf{F}\mathbf{W}_{n,k}(\lambda_k)\mathbf{W}_{n,k}^H(\lambda_k)\mathbf{F}^H) = P, \quad (22)$$

which is equivalent to

$$\text{tr}((\Sigma + \lambda_k\Gamma)^{-2}\Theta) = P, \quad (23)$$

where $\mathbf{Q}\Sigma\mathbf{Q}^H$ is the eigendecomposition of $\sum_{j=1}^K \mathbf{F}^H\mathbf{H}_{n,k}^H\mathbf{B}_{n,j}\mathbf{g}_{n,j}\mathbf{B}_{n,j}^H\mathbf{H}_{n,k}\mathbf{F}$ and $\Gamma = \mathbf{Q}^H\mathbf{F}^H\mathbf{F}\mathbf{Q}$, $\Theta =$

$\mathbf{Q}^H(\sum_{k=1}^K \mathbf{F}^H\mathbf{H}_{n,k}^H\mathbf{B}_{n,k}\mathbf{g}_{n,k}^2\mathbf{B}_{n,k}^H\mathbf{H}_{n,k}\mathbf{F})\mathbf{Q}$; then (23) can be simplified as

$$\sum_{m=1}^{N_{\text{RF}}} \frac{[\Theta]_{mm}}{([\Sigma]_{mm} + \lambda_k[\Gamma]_{mm})^2} = P. \quad (24)$$

Notably the optimum λ_k (denoted by λ_k^*) must be positive in this case and the left-hand side of (24) is a decreasing function in λ_k for $\lambda_k > 0$. Therefore (24) can be easily worked out by employing one-dimensional search techniques. Eventually, by plugging λ_k^* in (24), we can achieve the solution for $\mathbf{W}_{n,k}(\lambda_k^*)$, $k = 1, 2, \dots, K$, $n = 1, 2, \dots, N_b$.

The digital beamforming algorithm for the mmWave massive MIMO is summarized in Algorithm 2.

The optimization problem (13) has a differentiable objective function and a constraint set that is separable in the variables \mathbf{g} , \mathbf{W} , \mathbf{B} . The WMMSE algorithm is the block coordinate descent method applied to (13) and converges to a stationary point of (13), which is any limit point \mathbf{g}^* , \mathbf{W}^* , \mathbf{B}^* of the iterates generated by the WMMSE algorithm.

6. Simulation Results

In this section we present simulation results to characterize the performance of the proposed algorithm presented in Sections 4 and 5. The simulated channel is mmWave MIMO multiantennas channel model [25] extended from IEEE 802.11ad channel model [26]. We consider a single-cell MIMO-OFDMA system consisting of BS and K_{all} users, and the cell radius at the BS is the typical value for a microcellular system. The propagation environment is modeled as a $L_k = 8$ ray channel with uniformly random azimuth and elevation AoAs/AoDs distributed in $[0, 2\pi]$ and $[0, \pi]$. We assume that the Channel State Information (CSI) is updated once per frame and group 5 OFDM symbols into a frame. One OFDM symbol has 512 subcarriers including 352 data subcarriers. The transmitter is assumed to employ a UPA antenna and the UE is assumed to have $N_r = 2$ antennas. The interelement spacing in both BS and UE antenna arrays is set to half a wavelength. The other simulation parameters are shown in Table 1.

TABLE 1: Simulation parameter.

Parameter	Value
System bandwidth B	2560 MHz
Subcarrier frequency spacing	5 MHz
Number of subcarriers N_f	512
Resource block size	128 subcarriers \times 5 OFDM symbols
Channel coding method	Turbo coding with 1/2 code-rate
Modulation/demodulation mode	64QAM
Number of transmit antennas N_t	128, 256, 512 UPA
Number of resource blocks N_b	4
Number of simulation frames	5000
Total users K_{all}	16
Number of spatial multiplexing users K	2, 4

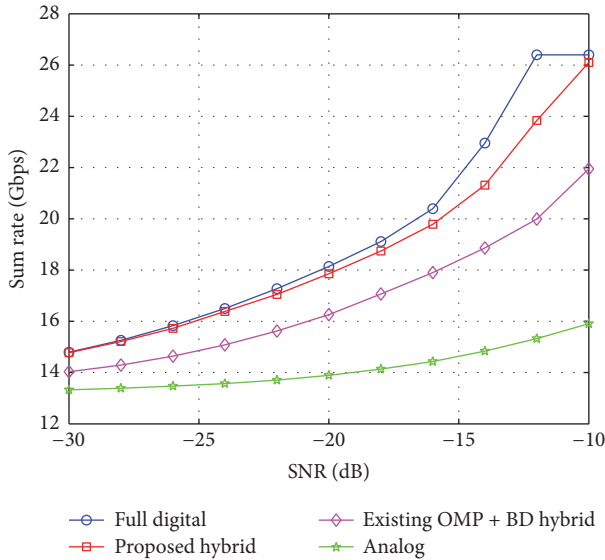


FIGURE 2: Sum rates versus SNR using the proposed hybrid beamforming, full digital beamforming, analog beamforming, and existing OMP + BD hybrid beamforming algorithms when $K = 2$ and $N_t = 512$.

First, we compare the sum rates of different algorithms when $K = 2$ and $N_t = 512$ in Figure 2, where we consider the system model in Section 2. The rate achieved by the proposed hybrid beamforming algorithm is compared with the full digital beamforming, analog beamforming, and existing OMP + BD hybrid beamforming algorithm [14, 27]. To evaluate the proposed hybrid beamforming algorithm, we assume azimuth and elevation angles of the phase shifters at the BS to be quantized with $M_\varphi = 20$ and $M_\theta = 20$. As can be seen from Figure 2, as expected the rate achieved by the proposed hybrid beamforming is higher than that of the analog beamforming, and superior performance is achieved by the digital beamforming approach. Meanwhile,

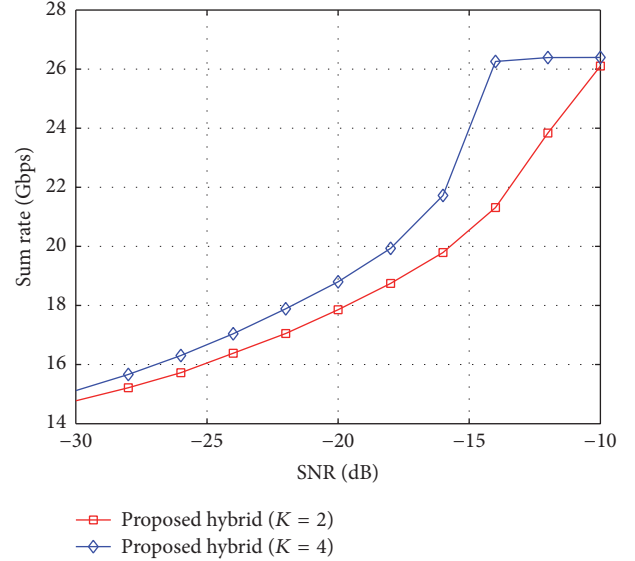


FIGURE 3: Sum rate versus SNR using the proposed hybrid beamforming when $K = 2, 4$ and $N_t = 512$.

the performance of hybrid beamforming is very close to the digital beamforming from the low to moderate SNR regions, and small performance gap is observed at SNR regions within $-22 \sim -10$ dB. When SNR increases to more than -10 dB, the proposed hybrid beamforming algorithm will achieve the same saturation value as digital beamforming. And the proposed hybrid beamforming yields a large improvement over the existing OMP + BD hybrid beamforming.

Secondly, we examine and compare the performance of the proposed hybrid beamforming with different number of scheduled users per block. We set the same number of transmit antennas in Figure 2 as $N_t = 512$ and vary maximum number of scheduled users in different blocks as $K = 2, 4$. As can be seen from Figure 3, increasing the number of MU-MIMO users multiplexing in each block can improve the sum rate (for SNR values) due to canceling the residual multiuser interference. The sum rate with $K = 4$ has risen sharply at SNR = $-30 \sim -14$ dB. When the value of SNR approaches to -12 dB, it approximately tends to be maximum value and then starts to level off as SNR exceeds -12 dB, while the sum rate with $K = 2$ will also achieve the same maximum value as the value of SNR exceeds -10 dB.

Finally, we discuss the performance of hybrid beamforming with different number of transmit antennas. The sum rate is achieved by the hybrid beamforming with $N_t = 128, 256, 512$ antennas with $K = 4$. The SNR ranges from -30 dB to -10 dB. It can be found in Figure 4 that as the number of transmit antennas increases, the performance of system enhances significantly from the low to moderate SNR regions. When the SNR approaches to -12 dB, the sum rate with $N_t = 512$ approximately tends to be stable. And it saturates after a certain SNR which is around -12 dB. As the value of SNR continues to increase, the sum rate of other cases will also achieve the same maximum value.

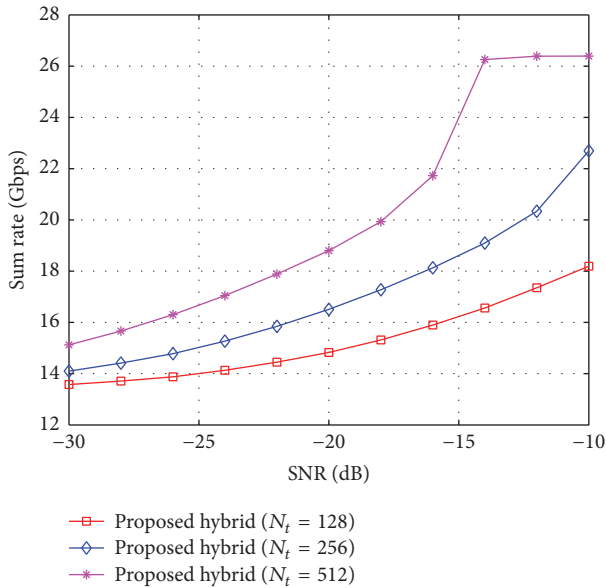


FIGURE 4: Sum rates versus SNR using the proposed hybrid beamforming algorithms when $K = 4$ and $N_t = 128, 256, 512$.

7. Conclusions

In this paper, we propose a joint user scheduling and MU-MIMO hybrid beamforming algorithm for mmWave FDMA massive MU-MIMO system. The users with the same strongest beams direction form an OFDMA user group. For the same OFDMA user group, BS allocates the corresponding frequency resources to the member with the best channel gain. Then, to maximize the mmWave system throughput, MU-MIMO users are selected from OFDMA user groups and other users to be scheduled. For the proposed hybrid beamforming, the analog beamforming vectors apply the optimal beam of each MU-MIMO user. The digital beamforming algorithm is solved by weight MMSE, which not only achieves the optimal performance for each user, but also mitigates the residual interuser interference.

Simulation results show that the performance of hybrid beamforming is very close to the full digital beamforming. Thus hybrid beamforming jointly designing with user scheduling can greatly improve the performance of mmWave OFDMA massive MU-MIMO system. Our further work will focus on reducing the complexity of the proposed hybrid beamforming algorithm and increasing the function of adaptive power allocation.

Competing Interests

The authors declare that there is no conflict of interests regarding the publication of this paper.

Acknowledgments

This paper is sponsored by National 863 Project (2014AA01A705).

References

- [1] W. Roh, J.-Y. Seol, J. Park et al., "Millimeter-wave beamforming as an enabling technology for 5G cellular communications: theoretical feasibility and prototype results," *IEEE Communications Magazine*, vol. 52, no. 2, pp. 106–113, 2014.
- [2] Y. Niu, Y. Li, D. Jin, L. Su, and A. V. Vasilakos, "A survey of millimeter wave communications (mmWave) for 5G: opportunities and challenges," *Wireless Networks*, vol. 21, no. 8, pp. 2657–2676, 2015.
- [3] ITU, "Assessment of the global mobile broadband deployments and forecasts for international mobile telecommunications," Tech. Rep. ITU-R M. 2243-0, 2011.
- [4] T. E. Bogale and L. B. Le, "Massive MIMO and mmWave for 5G wireless HetNet: potential benefits and challenges," *IEEE Vehicular Technology Magazine*, vol. 11, no. 1, pp. 64–75, 2016.
- [5] T. S. Rappaport, S. Sun, R. Mayzus et al., "Millimeter wave mobile communications for 5G cellular: it will work!," *IEEE Access*, vol. 1, no. 1, pp. 335–349, 2013.
- [6] P. Phunchongharn, E. Hossain, L. B. Le, and S. Camorlinga, "Robust scheduling and power control for vertical spectrum sharing in STDMA wireless networks," *IEEE Transactions on Wireless Communications*, vol. 11, no. 5, pp. 1850–1860, 2012.
- [7] O. Somarriba and J. Zander, "Robust STDMA scheduling in Multi-hop Wireless Networks for single-node position perturbations," in *Proceedings of the IEEE 20th International Symposium on Personal, Indoor and Mobile Radio Communications*, pp. 566–571, Tokyo, Japan, September 2009.
- [8] C. Li, R. Cai, and D. Liu, "A suboptimal STDMA scheduling for concurrent transmissions in mmWave wireless networks," in *Proceedings of the IEEE International Conference on Signal Processing, Communications and Computing (ICSPCC '14)*, pp. 137–141, Guilin, China, August 2014.
- [9] G. Li and H. Liu, "Resource allocation for OFDMA relay networks with fairness constraints," *IEEE Journal on Selected Areas in Communications*, vol. 24, no. 11, pp. 2061–2068, 2006.
- [10] M. Ergen, S. Coleri, and P. Varaiya, "Qos aware adaptive resource allocation techniques for fair scheduling in OFDMA based broadband wireless access systems," *IEEE Transactions on Broadcasting*, vol. 49, no. 4, pp. 362–370, 2003.
- [11] T. E. Bogale, L. B. Le, and A. Haghghat, "User scheduling for massive MIMO OFDMA systems with hybrid analog-digital beamforming," in *Proceedings of the IEEE International Conference on Communications (ICC '15)*, pp. 1757–1762, London, UK, June 2015.
- [12] D. E. Berraki, S. M. D. Armour, and A. R. Nix, "Codebook based beamforming and multiuser scheduling scheme for mmWave outdoor cellular systems in the 28, 38 and 60GHz bands," in *Proceedings of the IEEE Globecom Workshops (GC Wkshps '14)*, pp. 382–387, Austin, Tex, USA, December 2014.
- [13] L. Liang, W. Xu, and X. Dong, "Low-complexity hybrid precoding in massive multiuser MIMO systems," *IEEE Wireless Communications Letters*, vol. 3, no. 6, pp. 653–656, 2014.
- [14] T. E. Bogale and L. B. Le, "Beamforming for multiuser massive MIMO systems: digital versus hybrid analog-digital," in *Proceedings of the IEEE Global Communications Conference (GLOBECOM '14)*, pp. 4066–4071, Austin, Tex, USA, December 2014.
- [15] A. Alkhateeb, R. W. Heath, and G. Leus, "Achievable rates of multi-user millimeter wave systems with hybrid precoding," in

- Proceedings of the IEEE International Conference on Communication Workshop (ICCW '15)*, pp. 1232–1237, IEEE, London, UK, June 2015.
- [16] W. Ni and X. Dong, “Hybrid block diagonalization for massive multiuser MIMO systems,” *IEEE Transactions on Communications*, vol. 64, no. 1, pp. 201–211, 2016.
- [17] E. Jorswieck, B. Ottersten, A. Sezgin, and A. Paulraj, “Feedback reduction in uplink MIMO OFDM systems by chunk optimization,” in *Proceedings of the IEEE International Conference on Communications (ICC '08)*, pp. 4348–4352, Beijing, China, May 2008.
- [18] M. A. Ali, S. Al-Ghadhban, and A. S. H. Mahmoud, “Resource allocation scheme for MIMO-OFDMA systems with proportional fairness constraints,” in *Proceedings of the IEEE 8th International Conference on Wireless and Mobile Computing, Networking and Communications (WiMob '12)*, pp. 512–516, Barcelona, Spain, October 2012.
- [19] O. E. Ayach, R. W. Heath, S. Abu-Surra, S. Rajagopal, and Z. Pi, “Low complexity precoding for large millimeter wave MIMO systems,” in *Proceedings of the IEEE International Conference on Communications (ICC '12)*, pp. 3724–3729, Ottawa, Canada, June 2012.
- [20] T. E. Bogale, L. B. Le, A. Haghghat, and L. Vandendorpe, “On the number of RF chains and phase shifters, and scheduling design with hybrid analog-digital beamforming,” *IEEE Transactions on Wireless Communications*, vol. 15, no. 5, pp. 3311–3326, 2016.
- [21] Z. Li, P. Li, and K. G. Shin, “MU-MIMO downlink scheduling based on users’ correlation and fairness,” in *Proceedings of the 25th IEEE Annual International Symposium on Personal, Indoor, and Mobile Radio Communication (PIMRC '14)*, pp. 407–412, Washington, DC, USA, September 2014.
- [22] M. Stojnic, H. Vikalo, and B. Hassibi, “Rate maximization in multi-antenna broadcast channels with linear preprocessing,” *IEEE Transactions on Wireless Communications*, vol. 5, no. 9, pp. 2338–2342, 2006.
- [23] T. E. Bogale and L. B. Le, “Pilot optimization and channel estimation for multiuser massive MIMO systems,” in *Proceedings of the 48th Annual Conference on Information Sciences and Systems (CISS '14)*, Princeton, NJ, USA, March 2014.
- [24] Q. Shi, M. Razaviyayn, Z.-Q. Luo, and C. He, “An iteratively weighted MMSE approach to distributed sum-utility maximization for a MIMO interfering broadcast channel,” *IEEE Transactions on Signal Processing*, vol. 59, no. 9, pp. 4331–4340, 2011.
- [25] L. C. Pansana, *Transmit-Receive Beamforming for 60 GHz Indoor Wireless Communications*, Aalto University School of Science and Technology, Espoo, Finland, 2010.
- [26] A. Maltsev, V. Erceg, E. Perahia et al., Channel models for 60 GHz WLAN systems, IEEE Document 802.11-09/0334r8, May 2010, <https://mentor.ieee.org/802.11/dcn/09/11-09-0334-08-00ad-channelmodels-for-60-ghz-wlan-systems.doc>.
- [27] O. E. Ayach, S. Rajagopal, S. Abu-Surra, Z. Pi, and R. W. Heath, “Spatially sparse precoding in millimeter wave MIMO systems,” *IEEE Transactions on Wireless Communications*, vol. 13, no. 3, pp. 1499–1513, 2014.

Research Article

A Novel Simulator of Nonstationary Random MIMO Channels in Rayleigh Fading Scenarios

Qiuming Zhu,¹ Xinglin Liu,¹ Xuefeng Yin,² Xiaomin Chen,¹ and Cuiwei Xue¹

¹College of Electronic and Information Engineering, Nanjing University of Aeronautics and Astronautics, Jiangjun Road, Nanjing, China

²College of Electronics and Information Engineering, Tongji University, Caoan Road, Shanghai, China

Correspondence should be addressed to Qiuming Zhu; zhuqiuming@nuaa.edu.cn

Received 13 July 2016; Accepted 28 August 2016

Academic Editor: Qammer H. Abbasi

Copyright © 2016 Qiuming Zhu et al. This is an open access article distributed under the Creative Commons Attribution License, which permits unrestricted use, distribution, and reproduction in any medium, provided the original work is properly cited.

For simulations of nonstationary multiple-input multiple-output (MIMO) Rayleigh fading channels in time-variant scattering environments, a novel channel simulator is proposed based on the superposition of chirp signals. This new method has the advantages of low complexity and implementation simplicity as the sum of sinusoids (SOS) method. In order to reproduce realistic time varying statistics for dynamic channels, an efficient parameter computation method is also proposed for updating the frequency parameters of employed chirp signals. Simulation results indicate that the proposed simulator is effective in generating nonstationary MIMO channels with close approximation of the time-variant statistical characteristics in accordance with the expected theoretical counterparts.

1. Introduction

Multiple-input multiple-output (MIMO) technologies are widely used to improve the channel capacity and frequency utilization ratio without increasing system bandwidth or transmitting power. The traditional MIMO channels are usually modeled as wide-sense stationary (WSS) Rayleigh fading processes [1, 2]. However, the WSS assumption is not always satisfied, because the time-variant scattering environments, such as vehicle-to-vehicle (V2V) channel [3] and high-speed train channel [4], will change the statistical properties of MIMO channel over time. This kind of non-WSS channel, also called non-stationary channel, plays an important role in designing, validating, and optimizing the performance of real world wireless communication systems [3–6].

Based on the modeling methodologies adopted, channel models can be classified into geometrically based stochastic models (GBSMs) and correlation-based stochastic models (CBSMs) [7]. The nonstationary MIMO channels based on GBSMs have been investigated in [8–10]. Xiao et al. [8] were concerned with the time-variant parameters such as angles-of-arrival (AoA) and angles-of-departure (AoD) irrespective

of the scattering environment or clusters, while Wu et al. [9] focused on modeling the appearance and disappearance of clusters by Markov process or birth-death process. Moreover, Borhani and Pätzold [10] introduced a spatial Brownian path model to generate realistic moving trajectories of transceivers and employed it to model the time-variant channel by deriving the analytical expressions of AoA and angles-of-motion (AOM). Researches have showed that GBSMs are suitable for modeling nonstationary MIMO channels; however, the complexity increases significantly when the number of clusters increases dramatically.

On the other hand, CBSMs are usually used to evaluate the performance of MIMO systems due to their low complexity and have been applied in MIMO channel models [11], as well as standard channel models such as IEEE 802.11 TGN channel [12] and LTE-A channel [13]. When adopting the conventional CBSMs in nonstationary cases, it is a prerequisite to know the variation of the statistical properties of channel with respect to the time and frequency [14, 15], in order to construct a channel simulator generating nonstationary fading channel realizations. The simulation of CBSMs always requires generating multiple independent and

identically distributed (i.i.d.) Rayleigh fading processes. In the past three decades, a large number of researches have showed that this simulation can be efficiently performed by a finite sum of sinusoids (SOS) or cisoids (SOC) [16–25]. The mathematical reference model for this SOS method was initially proposed in [16] as Clarke’s model, and the famous simulator, namely, Jakes’ model, was developed in [17]. Pop and Beaulieu [18] suggested an improved Jakes’ model by applying random phase shifts to optimize the WSS property. Xiao and Zheng [19, 20], as well as Zajić and Stüber [21], introduced some random simulation parameters to enhance the performance.

The aforementioned simulation models are all nonergodic models, which need the arithmetic average over a large amount of simulation trails (snapshots) in order to approximate the desired properties [22]. To overcome this shortcoming, Pätzold and Wang [22–25] developed deterministic SOS simulators with low complexity. At the same time, the sum-of-cisoids (SOC) simulators are found to be more flexible and suitable for channel simulation in the nonisotropic scattering environments [26–29]. The accuracy of statistical channel properties obtained with both SOS and SOC simulators greatly depends on the simulation parameters computation method. The L_p -norm method [23, 26] owns high accuracy of statistical properties but requires a time-consuming progress of parameter optimization. The method of equal area (MEA) and its derivatives [24, 27, 28] can reduce the computation complexity but demand plenty of cisoids to emulate the correlation properties precisely. Recently, the Riemann sum method (RSM) was proposed by Gutiérrez et al. in [29] to generate channels with accurate autocorrelation. However, this method fails to generate channels with desirable envelope distribution when the number of cisoids is small.

It should be noted that all above existing SOS or SOC simulators are only designed for stationary channels with constant statistical characteristics. For simulating nonstationary channels, the conventional Kronecker model is extended in this paper for reconstructing correlated nonstationary MIMO Rayleigh fading channel observed in time-variant scattering environments. In addition, we propose a new SOC simulator based on the sum of chirp signals to generate multiple independent identically distributed (i.i.d.) Rayleigh fading channels of time-variant statistical characteristics. By utilizing the linearly changing Doppler frequencies, the new method is applicable to reproducing the desirable time-variant Doppler power spectral density (DPSD), envelope probability distribution function (PDF), autocorrelation function (ACF), and cross-correlation function (CCF).

The remainder of this paper is organized as follows: in Section 2, we give a nonstationary MIMO channel model originating from CBSMs. The existing stationary Rayleigh fading channel models including the reference model and simulation model are reviewed in Section 3. The proposed nonstationary MIMO channel simulator with a new parameters computation method is presented in Section 4. Section 5 gives the performance evaluation results and analysis of the new simulator. Finally, conclusive remarks are made in Section 6.

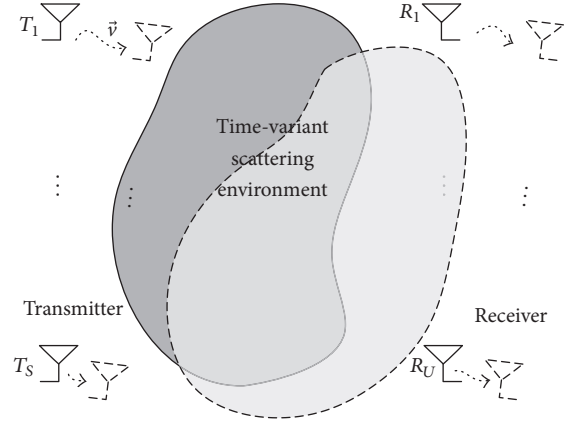


FIGURE 1: MIMO communication system with S transmitting antennas and U receiving antennas under mobile to mobile (M2M) scenario. The solid line and dash line indicate the positions of transceiver antenna arrays at two different time instances.

2. Nonstationary MIMO Channel Model

A MIMO mobile to mobile (M2M) communication system is illustrated in Figure 1, where the solid line and dash line indicate the positions of transceiver antenna arrays at two different time instances. The different scattering environments make the MIMO channel’s characters change over time.

Assuming a frequency nonselective MIMO channel system with S transmitting antennas and U receiving antennas, the MIMO channel matrix can be expressed as

$$\mathbf{H}(t) = [h_{u,s}(t)]_{U \times S}, \quad (1)$$

where $h_{u,s}(t)$ denotes the impulse response of the subchannel between the u th ($u = 1, 2, \dots, U$) receiving antenna and the s th ($s = 1, 2, \dots, S$) transmitting antenna. Considering a Rayleigh fading channel, the envelope and phase distribution of $h_{u,s}(t)$ obey, respectively, the Rayleigh and uniform distributions over $(0, 2\pi]$, while the statistical parameters such as variance may vary over time. The time-variant channel correlation matrix is defined as

$$\mathbf{R}_{\mathbf{H}}(t) = \boldsymbol{\rho} \{ \text{vec}(\mathbf{H}) \text{vec}(\mathbf{H})^H \}, \quad (2)$$

where $\text{vec}(\cdot)$ is the vector operator (stacking all elements of a matrix column-wise into a single vector), $(\cdot)^H$ denotes the Hermitian transposition, and $\boldsymbol{\rho}\{\cdot\}$ represents the correlation coefficient. $\mathbf{R}_{\mathbf{H}}(t)$ is a $US \times US$ matrix, and we can use it to remodel the nonstationary correlated MIMO channel as

$$\text{vec}(\mathbf{H}) = \mathbf{R}_{\mathbf{H}}^{1/2} \text{vec}(\mathbf{G}), \quad (3)$$

where $(\cdot)^{1/2}$ denotes any matrix square root fulfilling $\mathbf{R}_{\mathbf{H}}^{1/2} (\mathbf{R}_{\mathbf{H}}^{1/2})^H = \mathbf{R}_{\mathbf{H}}$ and \mathbf{G} is an $U \times S$ random matrix with zero mean i.i.d. complex Gaussian process entries. Assuming the scattering environments around the receiver and the transmitter are mutually independent, the channel correlation matrix can be expressed by the Kronecker product of

the transmitter correlation matrix $\mathbf{R}_{\mathbf{T}_x}(t)$ and the receiver correlation matrix $\mathbf{R}_{\mathbf{R}_x}(t)$,

$$\mathbf{R}_{\mathbf{H}}(t) = \mathbf{R}_{\mathbf{T}_x}(t) \otimes \mathbf{R}_{\mathbf{R}_x}(t), \quad (4)$$

where \otimes denotes the Kronecker product.

3. Multiple Stationary Rayleigh Fading Channels

The Kronecker model for a MIMO channel is related with the correlation matrix and complex Gaussian matrix. We can directly obtain the lower triangular matrix \mathbf{L} by performing Cholesky decomposition on $\mathbf{R}_{\mathbf{H}}$, $\mathbf{L} = \mathbf{R}_{\mathbf{H}}^{1/2}$, and $\mathbf{R}_{\mathbf{H}} = \mathbf{L}\mathbf{L}^H$. If $\mathbf{R}_{\mathbf{H}}$ is nonpositive definite, the eigenvalue decomposition method [30] needs to be applied. In this section, a brief review of the SOC-based simulation method applicable to generating multiple i.i.d. stationary Rayleigh fading channels is provided, and its performance is evaluated.

3.1. The Reference Model. Multiple Rayleigh fading processes are actually equivalent to a set of complex Gaussian random processes. Under this assumption, the k th Rayleigh fading process can be written as

$$\mu_k(t) = \mu_{k,i}(t) + j\mu_{k,q}(t), \quad k = 1, 2, \dots, K, \quad (5)$$

where $j \triangleq \sqrt{-1}$, $\mu_{k,i}(t)$, and $\mu_{k,q}(t)$ are uncorrelated and zero mean real-valued Gaussian processes. Thus, the fading envelope $\zeta_k(t) \triangleq |\mu_k(t)|$ and phase $\phi_k(t) \triangleq \arg\{\mu_k(t)\}$ yield the following PDFs, respectively:

$$p_{\zeta_k}(z) = \frac{2z}{\sigma_{\mu_k}^2} \cdot \exp\left\{-\frac{z^2}{\sigma_{\mu_k}^2}\right\}, \quad z \geq 0, \quad (6)$$

$$p_{\phi_k}(\theta) = \frac{1}{2\pi}, \quad \theta \in [-\pi, \pi),$$

where $\sigma_{\mu_k}^2$ denotes the variance of Rayleigh distribution. The autocorrelated Rayleigh fading process $\mu_k(t)$ can be further characterized by its ACF $r_{\mu_k\mu_k}(\tau) \triangleq E\{\mu_k^*(t)\mu_k(t+\tau)\}$, while the cross-correlated Rayleigh fading processes are characterized by their CCF $r_{\mu_k\mu_l}(\tau) \triangleq E\{\mu_k^*(t)\mu_l(t+\tau)\}$, $\forall k \neq l$. Here, $(\cdot)^*$ is complex conjugation and $E\{\cdot\}$ refers to the expectation of given argument. The DPSD $S_{\mu_k\mu_k}(f)$ describes the power distribution over Doppler frequency and can be calculated by performing the Fourier transform on the ACF; that is, $S_{\mu_k\mu_k}(f) = \int_{-\infty}^{\infty} r_{\mu_k\mu_k}(\tau) \exp\{-j2\pi f\tau\} d\tau$. Our aim is to generate K i.i.d. Rayleigh fading processes, which satisfy the following conditions:

$$r_{\mu_k\mu_k}(\tau) = \sigma_{\mu_k}^2 \int_{-\infty}^{\infty} p_{k,f}(f) \exp\{j2\pi f\tau\} df, \quad (7)$$

$$S_{\mu_k\mu_k}(f) = \sigma_{\mu_k}^2 p_{k,f}(f),$$

$$r_{\mu_k\mu_l}(\tau) = 0, \quad \forall k \neq l,$$

where $p_{k,f}(f)$ is the Doppler frequency PDF of the k th Rayleigh fading process. All elements of the antenna arrays

share a common scattering environment where the small-scale characterization assumption applies. Thus, the K random processes have the same Doppler frequency PDF denoted as $p_f(f)$.

The Gaussian-shaped DPSD plays an important role for nonisotropic scattering environment as in the cases of aeronautical channels. Specifications of frequency-shifted Gaussian DPSD can also be found in the channel models for pan-European, terrestrial, and cellular GSM system [28]. The theoretical expressions of Gaussian DPSD and ACF are given as follows:

$$S_{\mu\mu}^G(f) = \frac{\sigma_{\mu}^2}{f_c} \sqrt{\frac{\ln 2}{\pi}} e^{-\ln 2(f/f_c)^2}, \quad f \in [f_l, f_u], \quad (8)$$

$$r_{\mu\mu}^G(\tau) = \int_{f_l}^{f_u} S_{\mu\mu}^G(f) \exp\{j2\pi f\tau\} df, \quad (9)$$

where f_c denotes the 3-dB-cut-off frequency and f_l, f_u refer to the minimum and maximum frequency, respectively. For a symmetric Gaussian-shaped DPSD, the expression of (9) can be simplified as

$$r_{\mu\mu}^G(\tau) = \sigma_{\mu}^2 e^{-\pi(f_c/\sqrt{\ln 2})\tau^2}, \quad (10)$$

where $f_l = -f_{\max}$ and $f_u = f_{\max}$ with $f_{\max} = f_0 \cdot v/c$ denoting the maximum Doppler frequency due to the movements of transceivers. Here $c = 3 \times 10^8$ refers to the velocity of light, and f_0 is the carrier frequency.

3.2. The SOC Simulation Model. Based on the central limit theorem, a complex Gaussian random process can be modeled as the superposition of infinite properly weighted cisoids. It is impossible to realize the simulation with infinite numbers of cisoids. Fortunately, most of statistical properties can be approximated accurately when the number reaches a certain threshold. The SOC simulator for the k th Rayleigh fading process is defined as [27]

$$\hat{\mu}_k(t) = \sum_{n=1}^N \hat{c}_{k,n} \exp\{j(2\pi \hat{f}_{k,n}t + \hat{\theta}_{k,n})\}, \quad (11)$$

where N is the number of cisoids. The real-valued parameters, including gains $\hat{c}_{k,n}$, phases $\hat{\theta}_{k,n}$, and discrete Doppler frequencies, $\hat{f}_{k,n}$, remain constant during one simulation trial, which results in a deterministic channel in each snapshot. The gains $\hat{c}_{k,n}$ are given such that $E\{\hat{c}_{k,n}^2\} = \sigma_{\mu_k}^2/N$ for $n = 1, 2, \dots, N$, where $\sigma_{\mu_k}^2$ is the average power of channel fading. The phases $\hat{\theta}_{k,n}$ are independent random variables uniformly distributed over $[-\pi, \pi)$. The discrete Doppler frequencies $\hat{f}_{k,n}$ can be characterized by either $S_{\mu_k\mu_k}(f)$ or $r_{\mu_k\mu_k}(\tau)$. How to generate these two functions properly is the key issue.

3.3. Statistical Characteristics. From (11), we can derive the joint distribution $p_{\hat{\mu}_{k,i,n}, \hat{\mu}_{k,q,n}}(z_1, z_2)$ of two random variables $\hat{\mu}_{k,i,n}(t)$ and $\hat{\mu}_{k,q,n}(t)$ as [31]

$$p_{\hat{\mu}_{k,i,n}, \hat{\mu}_{k,q,n}}(z_1, z_2) = p_{\hat{\mu}_{k,i,n}}(z_1) \cdot \delta(z_2 - g(z_1)), \quad (12)$$

where

$$p_{\mu_{ki/q,n}}(z_{1/2}) = \frac{1}{\left(\pi \sqrt{c_{k,n}^2 - z_{1/2}^2}\right)}, \quad (13)$$

$$g(z_1) = \sqrt{c_{k,n}^2 - z_1^2},$$

when $|z_{1/2}| < c_{k,n}$. The joint characteristic function can be defined by the Fourier transform of joint probability density function as

$$\psi_{x,y}(v_1, v_2) = \iint p_{x,y}(z_1, z_2) e^{j2\pi(v_1 z_1 + v_2 z_2)} dz_1 dz_2. \quad (14)$$

Combining with following equation

$$\psi_{x,y}(v_1, v_2) = \prod \psi_{x_n, y_n}(v_1, v_2), \quad (15)$$

where $x(t) = \sum_{n=1}^N x_n(t)$, $y(t) = \sum_{n=1}^N y_n(t)$, and $x_n(t)$ and $y_n(t)$ are i.i.d. random variables, we can get

$$p_{\tilde{\mu}_{ki}\tilde{\mu}_{k,q}}(z_1, z_2) = 2\pi \int_0^\infty \left[\prod_{n=1}^N J_0(2\pi |c_{k,n}| v) \right] \cdot J_0\left(2\pi v \sqrt{z_1^2 + z_2^2}\right) v dv. \quad (16)$$

Finally, transforming the Cartesian coordination into the polar coordination with $z_1 = z \cos \theta$ and $z_2 = z \sin \theta$, the PDFs of envelope and phase can be expressed, respectively, as

$$p_{\tilde{z}_k}(z) = z (2\pi)^2 \int_0^\infty \left[\prod_{n=1}^N J_0(2\pi |\tilde{c}_{k,n}| v) \right] J_0(2\pi z v) v dv, \quad (17)$$

$$z \geq 0,$$

$$p_{\tilde{\phi}_k}(\theta) = \frac{1}{2\pi}, \quad \theta \in [-\pi, \pi] \quad (18)$$

when $\tilde{c}_{k,n} = \sigma_{\tilde{\mu}_k} / \sqrt{N}$ and $N \rightarrow \infty$ are considered; (17) is the same as the Rayleigh PDF.

As a deterministic simulation model, the statistical properties of output fading processes should be calculated by using time average instead of statistical average. According to the definitions of ACF, CCF, and DPSD, we can calculate the time-averaged functions as follows:

$$r_{\tilde{\mu}_k\tilde{\mu}_k}(\tau) = \sum_{n=1}^N \tilde{c}_{k,n}^2 \exp\{j2\pi \hat{f}_{k,n} \tau\},$$

$$S_{\tilde{\mu}_k\tilde{\mu}_k}(f) = \sum_{n=1}^N \tilde{c}_{k,n}^2 \delta(f - \hat{f}_{k,n}), \quad (19)$$

$$r_{\tilde{\mu}_k\tilde{\mu}_l}(\tau) = \sum_{n=1}^N \sum_{m=1}^N \left\{ \begin{array}{l} \delta(\hat{f}_{k,n} - \hat{f}_{l,m}) \\ \exp(-j2\pi \hat{f}_{l,m} \tau) \\ \exp[-j(\hat{\theta}_{k,n} - \hat{\theta}_{l,m})] \end{array} \right\}.$$

To satisfy with the requirements of (7), the following conditions for discrete Doppler frequency parameter should be fulfilled [29]:

$$\begin{aligned} f_{k,n} &\neq 0, \\ f_{k,n} &\neq f_{k,m}, \\ f_{k,n} &\neq f_{l,m}, \\ &\forall k, n, l, m, \quad k \neq l, \quad m \neq n. \end{aligned} \quad (20)$$

4. Nonstationary Channel Simulator

4.1. A New Simulation Model. The issue at hand is that the existing SOC simulator only applies to the stationary channel. To overcome this disadvantage, we propose a new simulator based on the sum of chirp signals as follows:

$$\tilde{\mu}_k(t) = \sum_{n=1}^N \tilde{c}_{k,n} \exp\left\{j\left(2\pi \int_0^t \tilde{f}_{k,n}(t) dt + \tilde{\theta}_{k,n}\right)\right\}, \quad (21)$$

where the discrete frequency parameters are changed over time and characterized by the time-variant DPSD. It can be observed that our model will reduce to the original SOC model if $\tilde{f}_{k,n}(t)$ is time-invariant. The flow chart of the proposed simulation model is illustrated in Figure 2, which also shows the signal of each branch is a frequency modulated signal.

The envelope and phase PDFs are independent of Doppler frequencies according to (12)–(18). Thus, the simulated envelope and phase PDFs based on the proposed model are the same as those for the conventional SOC model. Because the conventional definition of DPSD is invalid for nonstationary processes, we redefine the DPSD as the short-time DPSD which can be calculated by the squared amplitude of signal's short-time Fourier transform (STFT)

$$T_{\tilde{\mu}_k\tilde{\mu}_k}(t, f) \triangleq \int_{-\infty}^{\infty} \tilde{\mu}_k(\tau) e^{-j2\pi f \tau} w^*(t - \tau) d\tau, \quad (22)$$

where $w(t - \tau)$ is an analysis time window, which is sufficiently short such that the process can be considered to be stationary. Now we can redefine the time-variant ACF as the inverse Fourier transform of $T_{\tilde{\mu}_k\tilde{\mu}_k}(t, f)$

$$r_{\tilde{\mu}_k\tilde{\mu}_k}(t, \tau) = \int_{-\infty}^{\infty} T_{\tilde{\mu}_k\tilde{\mu}_k}(t, f) \exp\{j2\pi f \tau\} df. \quad (23)$$

Similarly, the CCF of a nonstationary process can be defined as

$$r_{\tilde{\mu}_k\tilde{\mu}_l}(t, \tau) \triangleq E \left\langle \tilde{\mu}_k^* \left(t + \frac{\tau}{2}\right) \tilde{\mu}_l \left(t - \frac{\tau}{2}\right) \right\rangle \quad (24)$$

and only consider the cases with $\tau = 0$.

4.2. Parameters Computation. The time-variant discrete frequency parameters will increase the complexity and uncertainty of our model, so it is very important to find an efficient

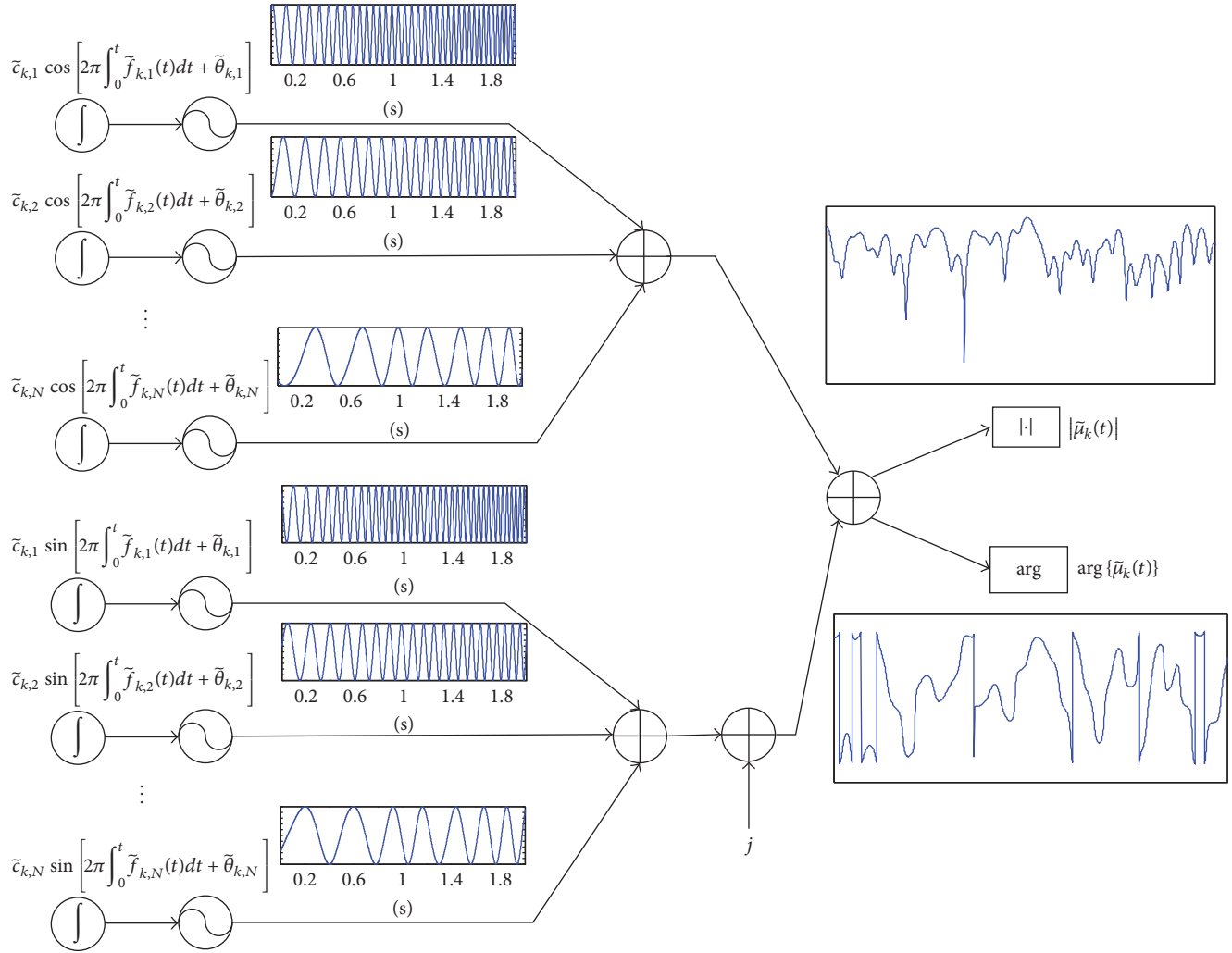


FIGURE 2: Simulation model for nonstationary Rayleigh fading by a finite sum of frequency modulated signals. $|\bar{\mu}_k(t)|$ and $\arg \{\bar{\mu}_k(t)\}$ are the amplitude and phase of the simulated fading process, respectively.

parameter computation method to update the value of frequency for each branch over time.

Assuming that the K Rayleigh fading channels have the same time-variant DPSD, we sample the continuous DPSD

with a short-time interval T_u (namely, channel updating interval). The updating interval is short enough, so the DPSD is approximately constant provided $S_{\mu\mu}^u(f)$ is within the u th interval. In addition, we propose the discrete frequency parameters following the linear change, which is

$$\tilde{f}_{k,n}^u(t) = b_{k,n}^u + s_n^u t, \quad t \in [(u-1)T_u, uT_u), \quad n = 1, 2, \dots, N, \quad k = 1, 2, \dots, K, \quad u = 1, 2, \dots, \quad (25)$$

where $b_{k,n}^u$ means the initial value of the k th Rayleigh fading channel and the n th branch of signal and s_n^u indicates the slope of the n th branch for K fading channels.

The slope s_n^u is calculated as

$$s_n^u = N_{sf} \frac{(F_n^u - F_{n-1}^u) + (F_n^{u+1} - F_{n-1}^{u+1})}{2T_u}, \quad (26)$$

where F_n^u is the computation result of MEA [28], which makes the area under the DPSD curve within the range $[F_{n-1}^u, F_n^u]$ equal to σ_{μ}^2/N

$$\int_{F_{n-1}^u}^{F_n^u} S_{\mu\mu}^u(f) df = \frac{\sigma_{\mu}^2}{N}, \quad n = 1, 2, \dots, N. \quad (27)$$

For the special case of a symmetric DPSD, we have $F_0^u = -f_{\max}^u$ and $F_N^u = f_{\max}^u$ with f_{\max}^u being the maximum Doppler

frequency. N_{sf} refers to the approximate number of periods for the Doppler frequency parameters linearly varying between the upper and lower boundaries. In this paper, we propose $N_{sf} \approx 10$ to ensure the mutual independence among K fading channels. When the value of $\tilde{f}_{k,n}^u(t)$ exceeds the upper boundary or reduces below the lower boundary, the updating direction will be reversed. This step keeps the value of Doppler frequency confined within the upper and lower boundaries. We set the upper boundary $B_n^u(t)$ as a straight line connecting F_n^u and F_n^{u+1} ; that is,

$$B_n^u(t) = \frac{F_n^{u+1} - F_n^u}{T_u} (t - t_u) + F_n^u, \quad n = 1, 2, \dots, N, \quad (28)$$

where t_u is the start time of u th interval. Similarly, the lower boundary expression can be obtained by setting $n = n - 1$.

Finally, we set the initial value $b_{k,n}^u$ of the u th interval equal to the end frequency in the last time interval

$$b_{k,n}^u = \begin{cases} U[F_{n-1}^u, F_n^u] & u = 1 \\ \tilde{f}_{k,n}^{u-1} & u = 2, 3, \dots, \infty. \end{cases} \quad (29)$$

For the case of $u = 1$, $b_{k,n}^1$ is specified as a random variable uniformly distributed over the range of $[F_{n-1}^1, F_n^1]$.

By applying the aforementioned computation method of (25)–(29), we can observe that the discrete frequency parameters generated are continuous and meet the requirements of (20). Additionally, our computation method will make the signal of each branch in (21) as a chirp signal, which are widely adopted in radar systems [32].

5. Simulation and Validation

In this section, we investigate the performance of the proposed simulation model by generating a 2×2 MIMO channel with center frequency $f_0 = 5$ GHz. Assuming that there are many scatters around the receiver but few scatters around the transmitter, the typical averaged correlation matrixes are [33]

$$\mathbf{R}_{\mathbf{R}\mathbf{x}}(t) = \begin{bmatrix} 1 & 0.3 \\ 0.3 & 1 \end{bmatrix}, \quad (30)$$

$$\mathbf{R}_{\mathbf{T}\mathbf{x}}(t) = \begin{bmatrix} 1 & 0.91 \\ 0.91 & 1 \end{bmatrix}.$$

The time-variant DPSD showed in Figure 3 is assumed to be symmetric Gaussian DPSD with $f_c = f_{\max} \ln 2$.

According to the proposed simulation method, we should generate $K = 4$ i.i.d. Rayleigh fading processes firstly. Then,

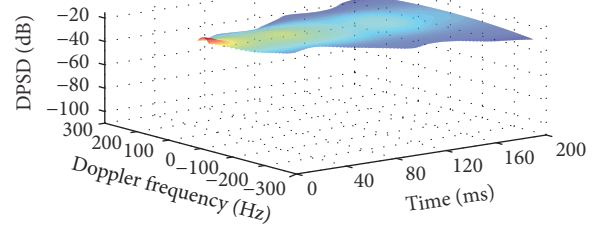


FIGURE 3: Time-variant Gaussian-shaped DPSD used to verify the performance of proposed simulator. This DPSD corresponds to the scenario of mobile receiver starting acceleration.

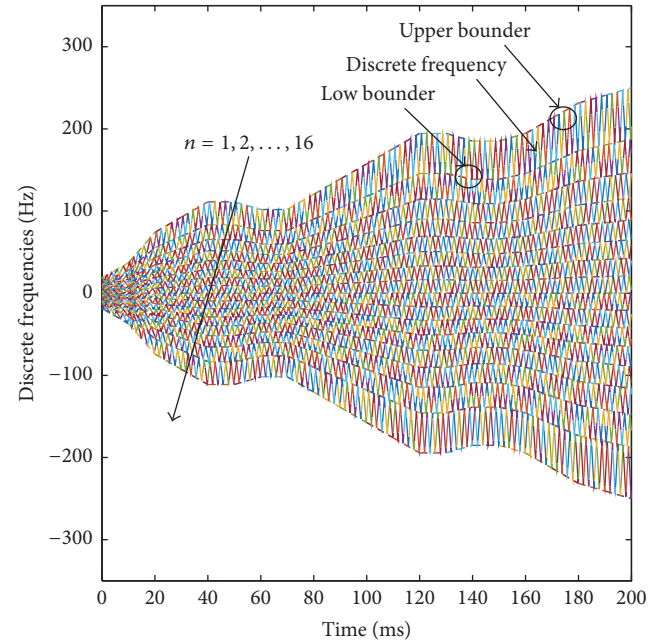


FIGURE 4: Calculated discrete frequency parameters for each branch ($N = 16$). These results are calculated from (25)–(29) and (31) with the DPSD given in Figure 3 and they will be used in (21) to generate the nonstationary Rayleigh fading.

with the given Gaussian DPSD, we get the area under the u th DPSD curve over $[-\infty, F_n^u]$ as

$$G(F_n^u) = \int_{-\infty}^{F_n^u} S_{\tilde{f}_{\mu}^u}^u(f) df$$

$$= \frac{\sigma_{\tilde{f}_{\mu}^u}^2}{2} \left[1 + \operatorname{erf} \left(\frac{F_n^u}{f_c} \sqrt{\ln 2} \right) \right], \quad (31)$$

$$n = 1, 2, \dots, N.$$

So the values of F_n^u can be obtained by applying a proper numerical root-finding technique on (31). Using $N = 16$, $N_{sf} = 10$, and $T_u = 10$ ms as an example, we can get the time-variant discrete frequency parameters from (25) to (29). Figure 4 illustrates the computation results of frequency parameters for 16 branches in solid lines, and the upper and lower boundaries of each branch are showed in dash lines.

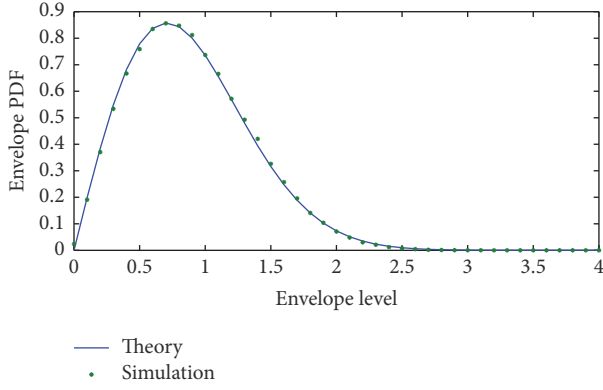


FIGURE 5: Time-averaged envelope PDF of generated fading channel. The simulation time and channel updating interval are 200 ms and 10 ms, respectively. The Rayleigh fading channels during all intervals are assumed to have normalized power. The dotted line denotes the averaged envelope PDF for all time intervals.

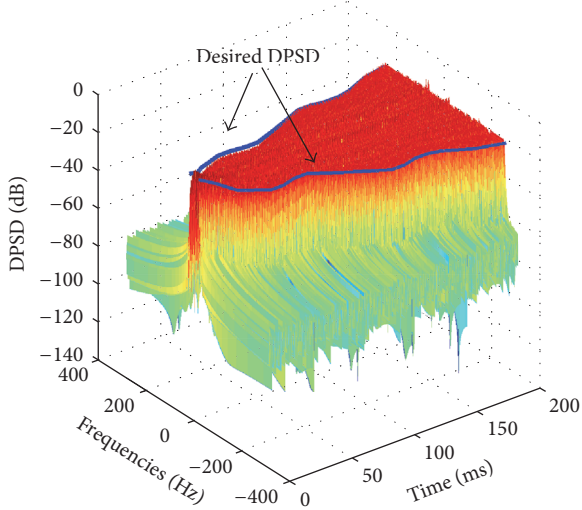


FIGURE 6: Time-variant DPSD of generated fading channel. The dotted line denotes the outline of desired Gaussian-shaped DPSD in Figure 3.

The four independent Rayleigh fading processes generated by using the proposed simulation model exhibit similar statistical properties for the envelopes PDF, ACF, and DPSD. Figure 5 illustrates the simulated envelope PDF of the first Rayleigh fading process. Here, we assume the Rayleigh fading channel with normalized power, and as a result, $\tilde{c}_{k,n} = 1/16$ is used, and the time-averaged PDF for all time intervals is given by dotted line depicted in Figure 5. The figure demonstrates that the simulation result provides a good approximation to the theoretical Rayleigh PDF. We also use (22) and (23) to calculate the time-variant short-time DPSD and ACF, which are showed, respectively, in Figures 6 and 7. For comparison purposes, we also highlight the edge lines of desired DPSD from Figure 3 and plot the calculated theoretical ACF with dotted line. It is apparent that the simulated channel's DPSD and ACF change over time and fit well with the desired graphs. Figures 5–7 also showed that the statistical results

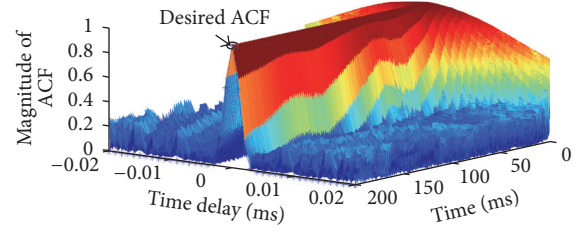


FIGURE 7: Magnitude of time-variant ACF of generated fading channel. The dotted line denotes the theoretical ACF corresponding to the Gaussian-shaped DPSD in Figure 3.

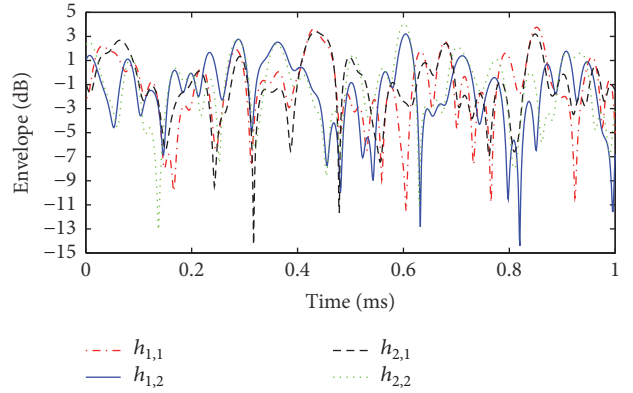


FIGURE 8: Envelopes of four subchannels generated by using the proposed simulation model.

obtained in each interval are very close to the theoretical value, which implies that our simulation model is applicable to reproducing the dynamic channels in the real world with tractable computational complexity.

Then, the four resultant i.i.d. Rayleigh fading processes are combined into the matrix \mathbf{G} . The channel correlation matrix and the lower triangular matrix can be calculated by applying the Kronecker product and Cholesky decomposition as, respectively,

$$\mathbf{R}_H = \begin{bmatrix} 1 & 0.3 & 0.91 & 0.273 \\ 0.3 & 1 & 0.273 & 0.91 \\ 0.91 & 0.273 & 1 & 0.3 \\ 0.273 & 0.91 & 0.3 & 1 \end{bmatrix}, \quad (32)$$

$$\mathbf{L} = \begin{bmatrix} 1 & 0 & 0 & 0 \\ 0.3 & 0.954 & 0 & 0 \\ 0.91 & 0 & 0.415 & 0 \\ 0.273 & 0.868 & 0.124 & 0.396 \end{bmatrix}. \quad (33)$$

Inserting the matrix \mathbf{G} and (33) into (3), we can finally get the nonstationary mutual correlated MIMO channel. Figure 8 gives the varying fading envelopes of all subchannels within 200 ms. The simulation accuracy for the MIMO channel is determined by the statistical properties of its subchannels. According to the theory of random process, the linear combination of four i.i.d. complex Gaussian processes will not change the characteristics of the envelopes PDF, ACF, and

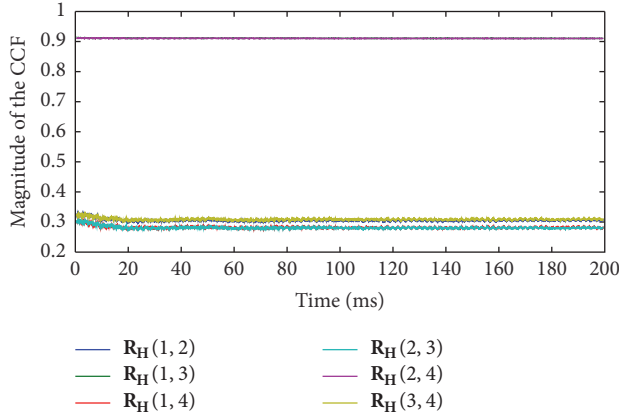


FIGURE 9: Magnitude of time-variant CCF between individual pairs out of four subchannels.

DPSD. So we only need to evaluate the performance of cross-correlation between individual pairs of subchannels. Figure 9 depicts the absolute value of the CCF over time.

Furthermore, the average of varying CCF can be calculated to get the correlation matrix of the simulated MIMO channel as

$$\tilde{\mathbf{R}}_{\mathbf{H}} = \begin{bmatrix} 1.0000 & 0.3003 & 0.9102 & 0.2753 \\ 0.3003 & 1.0000 & 0.2748 & 0.9099 \\ 0.9102 & 0.2748 & 1.0000 & 0.3034 \\ 0.2753 & 0.9099 & 0.3034 & 1.0000 \end{bmatrix} \quad (34)$$

which also exhibits good approximation to the desired one as (32), and the mean of simulation errors is merely 0.46%. The maximum of error is about 1.13%, while the minimum of error is less than 0.01%.

6. Conclusion

In this paper, a new simulation model originating from SOC method has been proposed to generate multiple non-stationary Rayleigh fading processes, which are very useful for the simulation of MIMO channel in time-variant rich-scattering environments as in V-V communication scenarios. Meanwhile, we assume that the frequency parameters of our model change linearly over time, which makes the signal of each branch (or subchannel) in the form of chirp signals. Under this assumption, an efficient updating method for the frequency parameters is proposed, which ensures that the statistical properties of simulated channel fading coincide with the desired ones. Simulation results demonstrate that our proposed simulator is able to generate nonstationary MIMO channels with time-variant statistical characteristics, such as the envelopes PDF, ACF, DPSD, and CCF approximating with their theoretical counterparts accurately.

Competing Interests

The authors declared that they do not have any commercial or associative interest that represents a conflict of interests in connection with this work.

Acknowledgments

This work is supported by Fundamental Research Funds for the Central Universities (NS2015046, NS2016044), Foundation of Jiangsu Key Laboratory of Internet of Things and Control Technologies (NJ20160027), Professional Master Innovation Projects for Jiangsu Ordinary University (SJZZ15_0040), and Postgraduate Innovation Base (lab) Open Fund for NUAA (kfjj20150409).

References

- [1] T. J. Willink, "Wide-sense stationarity of mobile MIMO radio channels," *IEEE Transactions on Vehicular Technology*, vol. 57, no. 2, pp. 704–714, 2008.
- [2] W. Weichselberger, M. Herdin, H. Özcelik, and E. Bonek, "A stochastic MIMO channel model with joint correlation of both link ends," *IEEE Transactions on Wireless Communications*, vol. 5, no. 1, pp. 90–99, 2006.
- [3] C.-X. Wang, X. Cheng, and D. I. Laurenson, "Vehicle-to-vehicle channel modeling and measurements: recent advances and future challenges," *IEEE Communications Magazine*, vol. 47, no. 11, pp. 96–103, 2009.
- [4] A. Ghazal, C.-X. Wang, B. Ai, D. Yuan, and H. Haas, "A non-stationary wideband MIMO channel model for high-mobility intelligent transportation systems," *IEEE Transactions on Intelligent Transportation Systems*, vol. 16, no. 2, pp. 885–897, 2015.
- [5] G. Matz, "On non-WSSUS wireless fading channels," *IEEE Transactions on Wireless Communications*, vol. 4, no. 5, pp. 2465–2478, 2005.
- [6] G. Matz and F. Hlawatsch, "Nonstationary spectral analysis based on time-frequency operator symbols and underspread approximations," *IEEE Transactions on Information Theory*, vol. 52, no. 3, pp. 1067–1086, 2006.
- [7] C.-X. Wang, X. Hong, X. Ge, X. Cheng, G. Zhang, and J. Thompson, "Cooperative MIMO channel models: a survey," *IEEE Communications Magazine*, vol. 48, no. 2, pp. 80–87, 2010.
- [8] H. Xiao, A. G. Burr, and L. Song, "A time-variant wideband spatial channel model based on the 3GPP model," in *Proceedings of the IEEE 64th Vehicular Technology Conference (VTC '06)*, pp. 1–5, IEEE, Montreal, Canada, September 2006.
- [9] S. Wu, C.-X. Wang, H. Haas, E.-H. M. Aggoune, M. M. Alwakeel, and B. Ai, "A non-stationary wideband channel model for massive MIMO communication systems," *IEEE Transactions on Wireless Communications*, vol. 14, no. 3, pp. 1434–1446, 2015.
- [10] A. Borhani and M. Pätzold, "A new non-stationary channel model based on drifted brownian random paths," in *Transactions on Engineering Technologies*, H. K. Kim, S.-I. Ao, and M. A. Amouzegar, Eds., chapter 33, pp. 429–443, Springer, Amsterdam, The Netherlands, 2014.
- [11] R. Couillet, M. Debbah, and J. W. Silverstein, "A deterministic equivalent for the analysis of correlated MIMO multiple access channels," *IEEE Transactions on Information Theory*, vol. 57, no. 6, pp. 3493–3514, 2011.
- [12] V. Erceg, L. Schumacher, P. Kyritsi et al., "TGN channel models," Tech. Rep. IEEE 802.11-03/940r4, IEEE, Garden Grove, Calif, USA, 2004.
- [13] 3GPP, TS36.101, V10.2.1, '3rd Generation Partnership Project; Technical Specification Group Radio Access Network; Evolved Universal Terrestrial Radio Access (E-UTRA); User Equipment (UE) radio transmission and reception (Release 10)', April 2011.

- [14] M. Herdin, N. Czink, H. Özcelik, and E. Bonek, "Correlation matrix distance, a meaningful measure for evaluation of non-stationary MIMO channels," in *Proceedings of the IEEE 61st Vehicular Technology Conference (VTC-Spring '05)*, pp. 136–140, Stockholm, Sweden, May 2005.
- [15] O. Renaudin, V.-M. Kolmonen, P. Vainikainen, and C. Oestges, "Non-stationary narrowband MIMO inter-vehicle channel characterization in the 5-GHz band," *IEEE Transactions on Vehicular Technology*, vol. 59, no. 4, pp. 2007–2015, 2010.
- [16] R. H. Clarke, "A statistical theory of mobile-radio reception," *Bell System Technical Journal*, vol. 47, no. 6, pp. 957–1000, 1968.
- [17] W. C. Jakes, *Microwave Mobile Communications*, Wiley-IEEE Press, Piscataway, NJ, USA, 2nd edition, 1994.
- [18] M. F. Pop and N. C. Beaulieu, "Limitations of sum-of-sinusoids fading channel simulators," *IEEE Transactions on Communications*, vol. 49, no. 4, pp. 699–708, 2001.
- [19] Y. R. Zheng and C. Xiao, "Simulation models with correct statistical properties for Rayleigh fading channels," *IEEE Transactions on Communications*, vol. 51, no. 6, pp. 920–928, 2003.
- [20] Y. R. Zheng and C. Xiao, "Improved models for the generation of multiple uncorrelated Rayleigh fading waveforms," *IEEE Communications Letters*, vol. 6, no. 6, pp. 256–258, 2002.
- [21] A. G. Zajić and G. L. Stüber, "Efficient simulation of rayleigh fading with enhanced de-correlation properties," *IEEE Transactions on Wireless Communications*, vol. 5, no. 7, pp. 1866–1875, 2006.
- [22] C.-X. Wang, M. Pätzold, and D. Yuan, "Accurate and efficient simulation of multiple uncorrelated Rayleigh fading waveforms," *IEEE Transactions on Wireless Communications*, vol. 6, no. 3, pp. 833–839, 2007.
- [23] M. Pätzold, B. O. Hogstad, and D. Kim, "A new design concept for high-performance fading channel simulators using set partitioning," *Wireless Personal Communications*, vol. 40, no. 3, pp. 267–279, 2007.
- [24] C.-X. Wang, D. Yuan, H.-H. Chen, and W. Xu, "An improved deterministic SoS channel simulator for multiple uncorrelated rayleigh fading channels," *IEEE Transactions on Wireless Communications*, vol. 7, no. 9, pp. 3307–3311, 2008.
- [25] M. Pätzold, C.-X. Wang, and B. O. Hogstad, "Two new sum-of-sinusoids-based methods for the efficient generation of multiple uncorrelated rayleigh fading waveforms," *IEEE Transactions on Wireless Communications*, vol. 8, no. 6, pp. 3122–3131, 2009.
- [26] M. Pätzold, U. Killat, Y. Li, and F. Laue, "Modeling, analysis, and simulation of nonfrequency-selective mobile radio channels with asymmetrical Doppler power spectral density shapes," *IEEE Transactions on Vehicular Technology*, vol. 46, no. 2, pp. 494–507, 1997.
- [27] M. Pätzold, B. O. Hogstad, and N. Youssef, "Modeling, analysis, and simulation of MIMO mobile-to-mobile fading channels," *IEEE Transactions on Wireless Communications*, vol. 7, no. 2, pp. 510–520, 2008.
- [28] M. Pätzold, *Mobile Radio Channels*, John Wiley & Sons, New York, NY, USA, 2nd edition, 2011.
- [29] C. A. Gutiérrez, M. Pätzold, A. Sandoval, and C. Delgado-Mata, "An ergodic sum-of-cisoids simulator for multiple uncorrelated rayleigh fading channels under generalized scattering conditions," *IEEE Transactions on Vehicular Technology*, vol. 61, no. 5, pp. 2375–2382, 2012.
- [30] G. H. Golub and C. F. Van Loan, *Matrix Computations*, Johns Hopkins University Press, Baltimore, Md, USA, 3rd edition, 1996.
- [31] S. Primak, V. Kontorovich, and V. Lyandres, *Stochastic Methods and Their Applications to Communications-Stochastic Differential Equations Approach*, John Wiley & Sons, Chichester, UK, 2004.
- [32] V. Khanh Nguyen and M. D. E. Turley, "Bandwidth extrapolation of LFM signals for narrowband radar systems," *IEEE Transactions on Aerospace and Electronic Systems*, vol. 51, no. 1, pp. 702–712, 2015.
- [33] J. P. Kermoal, L. Schumacher, K. I. Pedersen, P. E. Mogensen, and F. Frederiksen, "A stochastic MIMO radio channel model with experimental validation," *IEEE Journal on Selected Areas in Communications*, vol. 20, no. 6, pp. 1211–1226, 2002.